GEORG-AUGUST-UNIVERSITÄT GÖTTINGEN

Novel type of neutron polarization analysis using the multianalyser at PUMA – implementation, characterization and first experiments

---

Dissertation for the award of the degree "Doctor rerum naturalium" (Dr.rer.nat.) of the Georg-August-Universität Göttingen within the doctoral program Chemistry of the Georg-August University School of Science (GAUSS)

Submitted by:

Steffen Schwesig

Göttingen 2019

Thesis Committee

Prof. Dr. Götz Eckold, Institut für Physikalische Chemie

Prof. Dr. Prof. Dr. Simone Techert, Institut für Rötgenphysik/DESY

Members of the Examination Board

Reviewer: Prof. Dr. Götz Eckold, Institut für Physikalische Chemie

Second Reviewer: Prof. Dr. Simone Techert, Institut für Rötgenphysik/DESY

Further members of the Examination Board:

Prof. Dr. Jörg Behler, Institut für Physikalische Chemie

PD. Dr. Helmut Klein, Geowissenschaftliches Zentrum

Prof. Dr. Martin Suhm, Institut für Physikalische Chemie

Prof. Dr. Dietmar Stalke, Institut für Anorganische Chemie

Date of the oral examination: 16.08.2019

1 Table of contents

1 TABLE OF CONTENTS 1

1 INTRODUCTION 4

2 FRMII AND THE THREE AXIS NEUTRON SPECTROMETER PUMA 6

2.1.1 PUMA Multianalyzer/-detector 10

2.2 Why polarization analysis? 13

2.2.1 Polarizing crystals 13

2.2.2 Polarizing mirrors 14

2.2.3 Polarizing filters 14

2.2.4 2D and 3D polarization analysis 14

2.2.5 PUMA polarization analysis 16

3 SETUP 18

3.1 ^{3}He-filter 20

3.1.1 Relaxation time in the PUMA polarization analysis setup 24

3.2 Deflectors 26

3.2.1 Why we use two deflectors 29

3.2.2 Positioning of the deflectors 32

3.3 Collimator 33

3.4 Guide Field 36

3.4.1 Interlude: The PANDA guide field 38

3.4.2 Calculations for the quasi-Helmholtz guide field 39

3.4.3 Construction of quasi-Helmholtz coils 44

3.4.4 Result 46

3.5 Graphite Filter 48

3.6 Mezei Flipper 49

Table of contents

3.7 Calculating the polarization analysis Multianalyzer/-detector positions 52

4 THEORY 58

4.1 Theory of neutron scattering from nuclei nuclear scattering function 58

4.2 Theory of neutron scattering from magnetic moments; magnetic scattering function 61

4.3 Theory of polarized neutron scattering 64

4.3.1 Analytical calculations for PUMA polarization analysis 71

5 EXPERIMENTS 84

5.1 Testing the analytical model 84

5.2 Data reduction 87

5.2.1 Normalizing detectors 87

5.2.2 Background determination 88

5.2.3 Calculating SF/NSF intensities 92

5.2.4 Data processing example 93

5.3 Vanadium 94

5.4 Hematite 96

5.5 Copper (II) oxide 98

5.5.1 Sample preparation 101

5.5.2 Elastic measurements on CuO 104

5.5.3 Inelastic measurements on CuO 106

5.5.4 Low temperature scans 118

6 CONCLUSION AND FUTURE INVESTIGATION 121

6.1 Kinetic investigations with polarized neutrons 122

6.1.1 Oscillating magnetic field; construction and first tests 122

6.1.2 $CoCr_2O_4$ 126

6.2 Possible future improvements and advanced approaches for the PUMA polarization analysis 128

6.2.1 Intensity optimization 128

6.2.2 Full 3d polarization analysis 128

Table of contents

7 HANDBOOK FOR THE PUMA POLARIZATION SETUP 130

7.1 Setup check-list 130

7.2 Detailed setup guide 132

8 APPENDIX 137

8.1 Intermediate steps for guide field calculations 137

8.2 All magnetic scattering combinations 140

8.3 Technical details useful to remember 148

9 BIBLIOGRAPHY 152

1 Introduction

For condensed matter investigations the neutron is an established and ideal probe.
Their mass close to that of the proton means that they can be slowed down by collisions with atoms of similar mass, such as Hydrogen or Deuterium. This allows an experimenter to tailor their energy to the experimental requirements. In addition neutrons are without net charge, they function as a probe interacting directly with the nucleus of a sample, because of this there is only weak interaction with matter making neutrons a very good probe for bulk phenomena, with the additional unique feature that they can easily be transmitted through sufficient thin sample enclosure. This gives the experimenter very good control over his sample environment. They can be used to probe for a wide range of nuclear lattice and super-lattice phenomena by elastic and inelastic scattering techniques. But, as the neutron has a well-defined spin state it can also function as a probe for magnetic systems. Especially inelastic polarized neutron scattering is a powerful tool for investigations into magnetic structures and interactions in materials. For several reasons polarized inelastic neutron scattering is among the most time consuming measurement methods using neutrons. The time consuming nature of this type of experiment lead to the idea to measure both possible spin states in parallel to save costly beam time, with the option for some additional benefits resulting from this unique option.
This work describes the planning, development, installation and first tests of the polarization analysis setup for the thermal three axis neutron spectrometer PUMA @ FRM II. The full name of the instrument is DAS PUMA (“Drei-Achsen-Spektrometer mit Polarisationsanalyse und Multidetektor”), meaning three-axis-spectrometer with polarization analysis and multi-detector.
The PUMA polarization analysis introduces a new method for polarization analysis with neutrons, for the first time allowing the simultaneous measurement of both spin states by detecting spin-up and spin-down neutrons in different detector channels. Detecting both spin states at the same time can lead to a reduction in beam time necessary for a given experiment with polarized neutrons.
In addition to this unique feature, the simultaneous detection of both spin states is very useful for kinetic experiments as one can directly observe the change of both spin components depending on the current state of the sample. It is also a mayor boon if one is interested in an experiment where, for the required information it is difficult to guarantee the same conditions for the two measurements in a conventional polarization setup. The new PUMA setup eliminates these experimental problems and is the first time a three axis spectrometer has the capability to measure both spin states at the same time.
This work will describe the development process, implementation and testing of this new technique.
The first part will give an overview of neutron scattering

Introduction

The next part focusses on development and testing of the components used for the polarization setup.

Following is a section about experiments done during this work, starting with early proof of principle measurements and continuing with first inelastic neutron measurements in the multiferroic phase of CuO. Multiferroic means that a material shows more than one ferroic attribute, such as ferroelectricity or ferromagnetism, in one phase.

A chapter summarizing our achievements and sketching some ideas how to continue with this method can be found after the experimental section.

The last part is a handbook for the installation of our setup at PUMA to give some guidelines for future investigators as well as an appendix with some further, not essential, information.

2 FRMII and the three axis neutron spectrometer PUMA

Fig. 1: Photo of PUMA in its „simple“ conventional configuration

PUMA is one of the world's highest neutron flux three axis spectrometers (TAS)[1].
PUMA is located at beamline 7 (SR7) of the Heinz-Meier-Leibnitz (MLZ) neutron source in Garching near Munich. The neutron source is a nuclear reactor using highly enriched uranium as fuel, and it is moderated by heavy water. Thermal power output of the reactor reaches up to 20MW. This gives the source a peak neutron flux of $8 \cdot 10^{14}$ $cm^{-2}s^{-1}$.

As every TAS PUMA consist of three main components. These are, shown in Fig. 1, (respectively in the Fig. 2 general layout sketch) on the reactor side the castle, constructed from high density concrete to shield the environment from radiation originating from the monochromator housing. Following the beam path we arrive at the sample table. After this is the analyzer/detector located inside the blue shielding box.

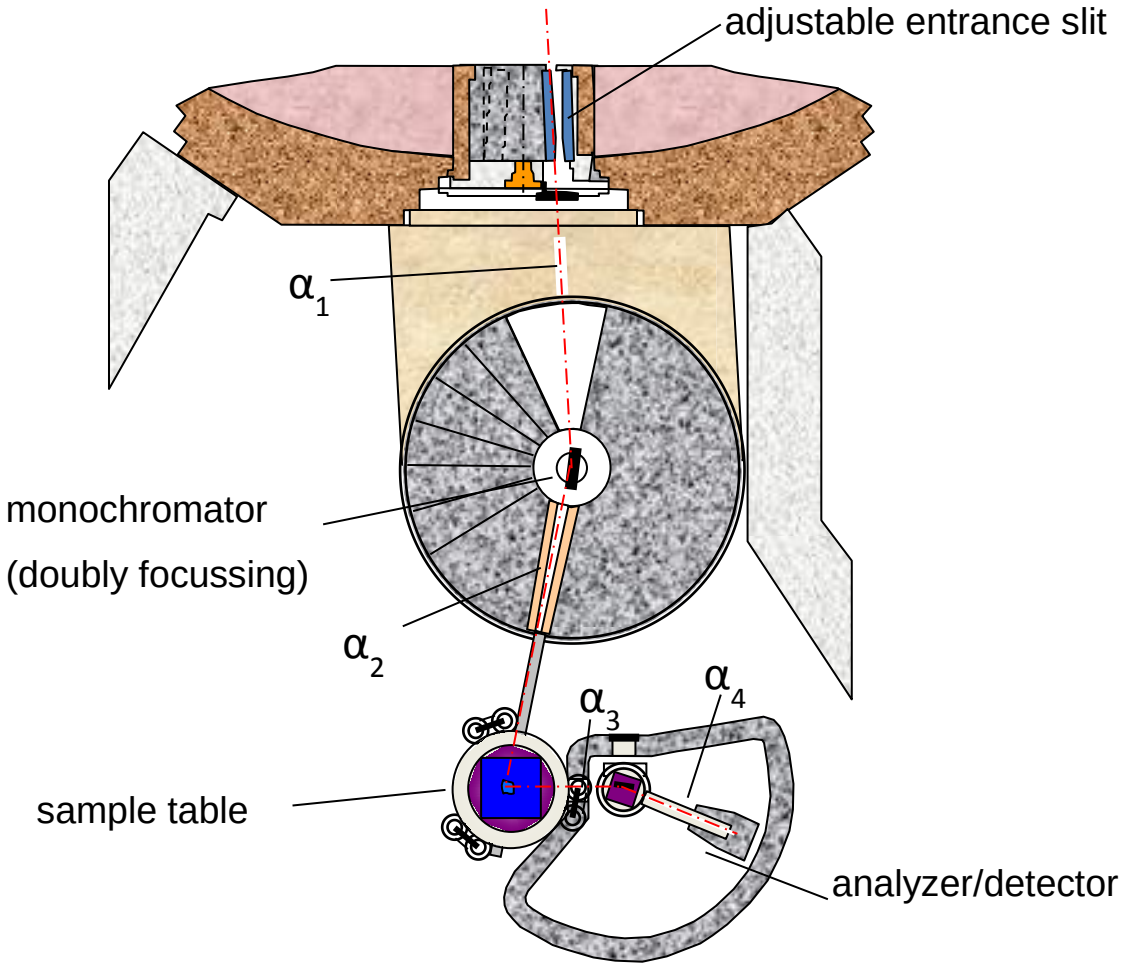

Fig. 2: Sketch of the general PUMA layout showing the monochromator, sample table, and detector/analyzer box as well as the four collimators, $\alpha_{1\text{-}4}$

This setup means that a TAS can be looked at as a very good direct visualization of the scattering triangle. The scattering triangle is a representation of the initial and final wave-vector of a scattering experiment forming a closed triangle with the ***Q***-vector for a conserved momentum case. For a TAS the initial wave-vector $\boldsymbol{k}_i$ is given by the monochromator angle and the final wave-vector $\boldsymbol{k}_f$ by the angle of the analyzer, thus forming the triangle shown in Fig. 3.

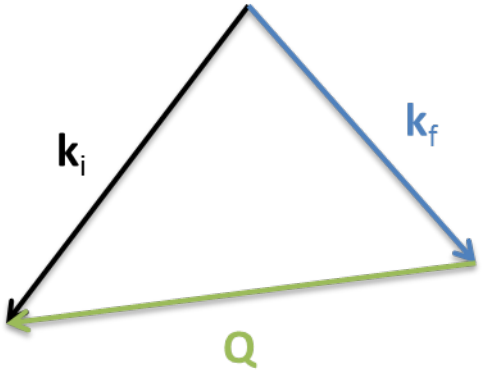

Fig. 3: Scattering triangle build by initial/final wave-vector $\mathbf{k}_{i/f}$ and scattering-vector **Q**

The white neutron beam from the reactor reaches the monochromator drum. There are four different doubly focusing monochromator systems available for PUMA: PG(002), Cu(111), Cu(220) and Ge(311). Each monochromator selects a different energy range from the white neutron beam and reflects it towards the sample position. Between the source and the sample there are two collimators, α_1 (20', 40', 60' and open) before the monochromator and α_2 (14', 20', 24', 30', 45', 60' and open) between monochromator and sample. For practical purposes, such as resolution calculations open means 120' of collimation.

The sample table allows full rotation of the sample as well as tilting (up to ±13°) and translations in all three dimensions (x,y ±10mm and z±19mm).

Located behind the sample table is the analyzer/detector box. This box contains the conventional analyzer/detector setup or, if installed, the PUMA multianalyzer/-detector. The blue box is built to shield the detectors from background gamma or neutron radiation. It can move around the sample position in a large angular segment, allowing a wide range of possible scattering vectors. In addition to the angular movement the distance between sample table and analyzer/detector box can also be varied. This feature is fundamental for our polarization analysis setup as discussed in section 3 Setup.

PUMA is a thermal TAS meaning that the neutrons arriving at the instrument are moderated to a temperature of 300K. In the MLZ this is done by the 300K water of the reactor. Thermal neutrons are used at SR 3, 5, 7 and 8.

The MLZ also offers the option of hot and cold neutrons for other instruments. Hot neutrons are moderated by a 2300K carbon block heated by the gamma radiation of the fuel elements. These neutrons go to instruments located at SR9.

To generate cold neutrons there is a moderator of 18K liquid deuterium located near the reactor core. SR 1, 2 and 4 are connected to the cold source. Roughly speaking neutrons of different temperatures have also different movement speeds, wavelengths, and different energies. There is

nearly unanimous consensus that neutrons of 25 meV or 300K are thermal, but there is no standard for neutron temperature ranges. For one interpretation see Table 1.

	Temperature [K]	Energy [meV]	Wavelength [Å]	Speed [m/s]
Cold	1-116	0.1-10	28.6-9	138-1380
Thermal	116-1160	10-100	9-0.9	1380-4370
hot	1160-5802	100-500	0.9-0.4	4370-9770

Table 1: Neutron temperatures/wavelengths

A TAS is a very flexible instrument that can cover a very large area of (***Q***, ω) space. A conventional TAS can only follow point by point measuring programs, resulting in relatively slow probing of the sample. This is a problem, as beam time on a neutron experiment is a sparse resource and every experiment is a huge investment in time and money. There are some ways to speed up sampling of an area of interest in (***Q***, ω) space. The most basic idea is to increase neutron flux to reduce measurement time, but there are also some more subtle methods such as the multi-analyzer/detector of PUMA discussed in the next section.
So a TAS is a flexible and powerful, albeit slow, instrument, especially for inelastic measurements using polarized neutrons, as these techniques are very time consuming.

2.1.1 PUMA Multianalyzer/-detector

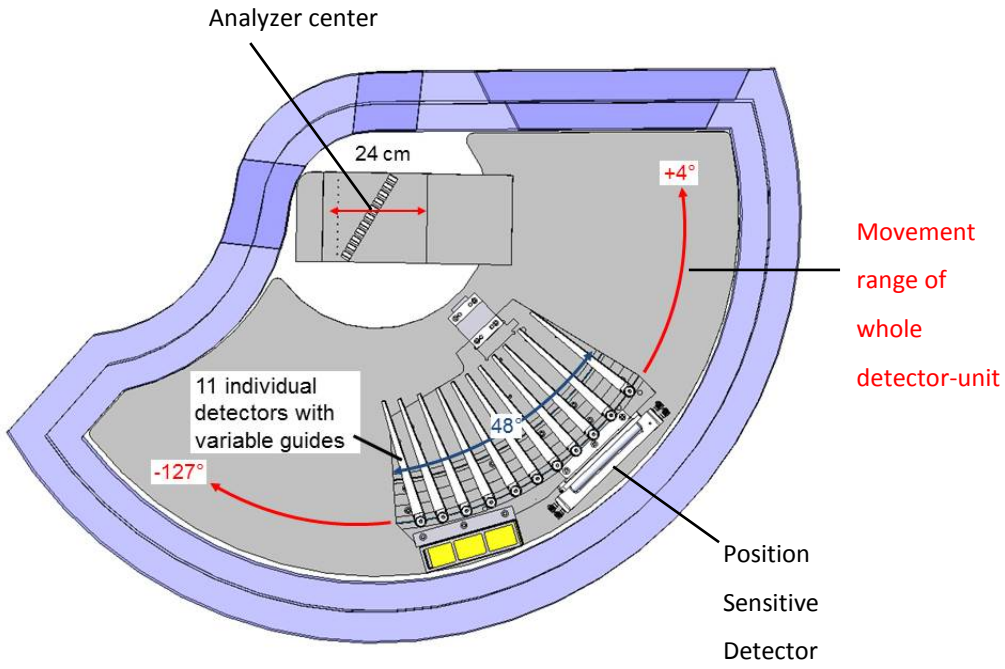

Fig. 4: The PUMA MAD showing the eleven analyzer/single detectors, as well as the PSD, then translate movement range of the analyzers and the angular range of movement for the whole detector-unit and the individual single detectors

The PUMA multi-channel analyzer and detector (MAD) system is a central part of this thesis. Its characteristics and use are discussed in more depth in this section. The MAD consists of eleven independent analyzers and eleven corresponding detectors. Fig. 4 shows a drawing of the whole MAD with its main components in top down view. This practically results in a set of eleven secondary spectrometers that can be used simultaneously. In the conventional mode of operations this allows PUMA to scan eleven different k_f-vectors at the same time. This reduces scanning time during an experiment by roughly an order of magnitude, depending on the used configuration.
Now, combining the MAD with polarized neutrons we are able to measure both neutron spin states of our scattered beam simultaneously, a novel, and to our knowledge unique, feature for a TAS system. The development, implementation, and first experiments are the central motivation of this work. For the PUMA multianalyzer system exists an in depth description in “The multianalyser system of the three axes neutron spectrometer PUMA: Pilot experiments with the innovative multiplex technique” [2].

There are also other TAS multiplex systems and methods in use. For example the first TAS with multiplex system was the RITA spectrometer at Risø. RITA-1 had a seven-bladed PG analyzer working with a single detector or a PSA and different modes of operation. It could be operated as a normal TAS, as well as in focusing and dispersing analyzer modes, see [3]. In this way it is a precursor to the PUMA MAD system. Its direct successor instrument, RITA-2, has a nine-bladed analyzer with the option of using PG (0 0 2) or Ge (1 1 1) and a PSD as the main detector. RITA-2 is a cold neutron instrument located at SINQ in Switzerland.

Another option for a multiplex system is the flat cone approach where the analyzer reflects the scattered beam out of the horizontal plane and into a detector array covering a large area. This allows for the detection of a wide range of scattering angles for a given energy simultaiously. An early example for such an instrument was the modified R1 spectrometer at the BER II reactor in Berlin [4]. An example for a contemporary instrument is IN20, a thermal TAS at ILL in France. Today there are several systems of both types in use.

Fig. 5: Backside of multi-analyzer blades, viewing direction towards sample table

This sub-chapter aims to give a short overview over the system. The multianalyzer/-detector (MAD) consists of a multianalyzer (MA) with eleven independently movable analyzer blades and the multidetector (MD) with eleven detectors. Each analyzer corresponds to one detector. In addition to the array of single detectors there is also an integrated position sensitive detector (PSD). While the single detectors can be moved according to the analyzer angle the PSD is a fixed position facing the sample table.

Each analyzer blade can be independently rotated by up to 90° and translated within a range of 25 cm. Furthermore the whole analyzer can be rotated as a single unit. Each analyzer blade holds five

vertically focusing 25x30 mm^2 crystal plates of pyrolytic graphite ((002)-PG) crystals, giving us a total height of 15cm, for energy analysis of the scattered beam. This means that the MA can work like a collection of eleven analyzers, each with their own k_f.

The MD detectors are conventional 1'' ^{3}He tube detectors which can move around the analyzer center on a circle segment. The angular width of this segment is a little over 130°, see Fig. 4. While the whole MD unit can move over 130° the individual detectors mounted on it have a motion range of 21° on the MD (48° overall, each detector needs 2.46° of space to avoid collisions resulting in 21° of free range). Single detectors are positioned by combined movement of the whole MD unit and movement of the detector in question. Each detector tube has a set of two Cd-coated guides to avoid crosstalk between the detectors and to shield them from neutrons not on a trajectory associated with the corresponding analyzer. Each guide can be rotated towards its analyzer to find the correct cutoff point where the detector receives the maximal amount pf intensity from its analyzer with minimal stray neutrons. The cadmium in the guides has a very large absorption cross section (the peak cross section for ^{113}Cd is around 20000 barn for thermal neutrons), thus preventing almost all neutrons from traversing a guide.

Fig. 6: A photo of the multi-detector with the eleven single detectors in parking position on the right side. The detector tubes are concealed by their guides.

The multidetector array of eleven ^{3}He-detectors can be freely moved and is positioned according to the reflection of the neutrons at the corresponding analyzers. Each detector is a tube filled with ^{3}He under a pressure of 10 bar. Detecting neutrons gives us the problem of converting a charge less particle into an electronic signal. One way to archive this utilizing ^{3}He is sketched in the next paragraph: The detectors have a wire inside the gas filled tube that functions as an electrode. When a neutron hits the detector the following reaction takes place:

$$^{3}\mathrm{He} + \mathrm{n} \xrightarrow{5333\mathrm{b}} \mathrm{p} + {}^{3}\mathrm{H} + 0.765\mathrm{MeV}$$

This means that we now have a charged particle in form of a single proton that can be detected. The PSD is constructed from seven detector tubes arranged in two rows, with three tubes in the first, and four tubes in the second row. So it is an array of ^{3}He-detector tubes with an effective length of 230 mm, covering an angular range of 6-7°. Over its range the PSD shows a sensitivity trend that needs to be taken into account. A scan where the whole detector was exposed to a uniform beam using a vanadium sample can be used for this, see Fig. 71 in the appendix. The PSD tubes work principally in the same way as the single detector tubes. What makes them position sensitive is that the read out electronics detect a signal on both ends of the electrode wire for each proton hitting it and use this time difference between the signals to calculate where on the wire the detection happened. For the polarization analysis developed in this work the PSD is mainly used for adjustments and checking the beam profile during the installation of the experiment. The use of the PSD is discussed in some detail in chapters 4.3.1, 5.1 and 7.

2.2 Why polarization analysis?

Due to the low intensities of polarized neutron beams PA started only in the 1980s to gain more mainstream use, nearly three decades after the first experiments. These low intensities are a result of every method used to polarize a white neutron beam.
For the price of this reduced intensity one gains the key advantages of polarized neutrons, their ability to discriminate between magnetic and nuclear scattering processes. This allows getting information about spin dynamics and magnetic structure of a given sample.

2.2.1 Polarizing crystals

There are three common methods to polarize a neutron beam. The first is by Bragg-scattering from a magnetic Heusler-compound crystal. A Heusler-compound is a material containing an intermetallic Heusler-phase showing behaviors not expected from their component elements. For example the first discovered Heusler-compound Cu_2AlMn shows ferromagnetic properties at room temperature despite the fact that all of its component elements are non-ferromagnetic. Another example of a Heusler compound would be Fe_3Si.
Such a Heusler crystal produces a polarized beam while under the influence of a magnetic field and when its Bragg fulfills certain conditions for magnetic interactions, see chapter 2.8.5 by B. Roessli and

P. Böni in [5]. Typically given examples are the (1 1 1) reflection of Cu_2AlMn or the (2 0 0) reflection of $Co_{0.92}Fe_{0.08}$. These materials can be used to build polarizing neutron monochromators as well as energy and polarization analyzers.

2.2.2 Polarizing mirrors

Another method uses a polarizing bender where the total reflection of the incident neutron beam from a magnetic layer used as a neutron mirror produces a polarized beam. Fe/Si multilayers are an example for such a neutron supermirror. At such a mirror neutrons have different refractivity, depending on their spin state. Due to the refractivity difference the two spin states are reflected under differing angles, creating two beams. In this way such a device also acts as a spin selector. The result of this is the production of a beam of only one spin component while losing the intensity of the second component. More than half of the incident neutrons are lost, due to the removal of all neutrons with the "wrong" spin state, as well as some of the preferred neutrons (as no mirror has perfect reflectivity). In this work we are utilizing a set of polarizing neutron mirrors, but not to polarize our incident beam, but to separate the spin components of our scattered beam. See 3.2 "Deflectors".

2.2.3 Polarizing filters

The third option it the method used in this work, a polarizing ^{3}He-cell. The ^{3}He in such a cell is polarized causing a much higher absorption cross-section for one of the neutron spin states. The cell absorbs neutrons of the undesired polarization state and transmits most of the other state as described in 3.1 "^{3}He-filter". Such a polarizing filter will start with a given polarization achieved by optical pumping of the He gas, but due to magnetic inhomogeneity and collisions of the polarized nuclei with the cell walls polarization will degrade over time.
Again we are losing somewhat more than half of our incident neutrons.

2.2.4 2D and 3D polarization analysis

After the beam is polarized, a magnetic field along the beam path is necessary to preserve beam polarization. Even small disturbances in the homogeneity of the field will depolarize the beam. However, for some experimental conditions it can be useful to change the spin orientation. This can

be done by rotating the spin through changes in guide field orientation where neutron speed and field orientation need to be carefully coordinated.

In addition to a method for polarizing there also needs to be a method for analyzing the scattered beam. This works along the same line as polarizing the incident beam.

Polarization analysis can be done in basically two ways, uniaxial, where a guide field at the sample position orients the spins along its axis or as a full spherical polarization analysis where the interaction between sample and incident beam happens in a field free environment. The present work uses a uniaxial approach. The main disadvantages of a uniaxial system is that one is more restricted in planning and executing an experiment as the incident spin orientation and sample have to be matched. Furthermore one only measures a projection along single axis. This means that more than one measurement is necessary when the scattered polarization is not exactly parallel or antiparallel to the incident polarization.

For a full 3D polarization approach the two options are CryoPAD or MuPAD. Both of them create a field free sample environment in which the spin-orientation of the incident neutrons and sample can be chosen at will. They differ in their method of creating the field free space;

CryoPAD has two superconducting Meissner screens to isolate the sample from magnetic stray fields. The shields work with the Meissner effect where a magnetic field gets expulsed from a superconductor when it transits into the superconducting phase. For a more detailed description look at Tasset, 1989 [6].

MuPAD on the other hand works by isolating a field free region with a Mu-metal shield. A nice description of MuPAD can be found in Janoschek, 2007 [7].

In both cases the incident spin orientation is rotated in the requested orientation by a combination of a nutator and Lamor precession while entering the field free space. In the same way the scattered beam is oriented back parallel to the guide field upon leaving the shielded volume.

Finally for uniaxial, as well as spherical polarized neutron scattering, the scattered beam has to be polarization analyzed.

Now, taking into account the additional information provided by the polarization state of the incoming and scattered neutron-beam one can gain new conclusions regarding the magnetic behavior of the scattering sample

2.2.5 PUMA polarization analysis

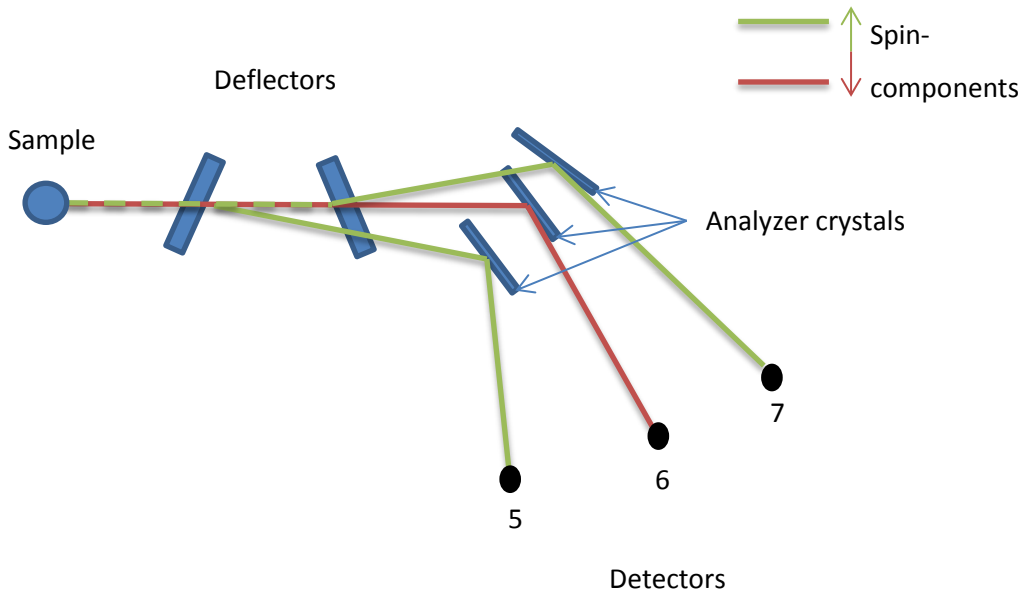

Fig. 7: Sketch of the PUMA polarization analysis idea

All previous methods for polarized neutron analysis can only detect one spin component at a time, losing intensity and possibly information about the sample if the experiment doesn't call for a repeated measurement with the second spin direction. This can also lead to some experimental problems for kinetic experiments.

To avoid this we are using some polarizing neutron mirrors to split the scattered beam into its spin components and then utilize the PUMA MAD to detect both spin states simultaneously, see Fig. 7 for a sketch of the principle.

For the PUMA polarization analysis we restricted the multianalyzer to a constant k_f-configuration with k_f= 2.662 $Å^{-1}$ because of our use of a PG filter to avoid higher order contamination. Usually only the three central analyzer crystals 5, 6, and 7 are used.

For the central channel, usually analyzer and detector number 6, this means the graphite angle of -20.6° for the analyzer and the matching position for its detector. For the other two analyzers it is -20.6 plus (analyzer 5) or minus (analyzer 7) angle of corresponding deflector. The single detectors themselves are mounted on a curved rail covering only 48°, but this setup can rotate around the analyzer center using a coupled axis device (CAD). This means that for most configurations the position of the detector is given by a combination of CAD position and position of the detector on its rail. CAD is a virtual axis where the whole sled housing the MD is rotating around the analyzer center

while the MA is stationary. This can be illustrated using Fig. 4. Everything would be stationary except for the detector-unit moving along the whole range indicated by the red arc.

For the cost of some intensity, making polarized neutron experiments some of the most time consuming neutron measurements possible, one gains unique insights into magnetic structures and dynamics.

3 Setup

In the following chapter the PUMA polarization analysis setup and its components will be examined in some detail. A sketch of the setup is shown in Fig. 8 to illustrate which components are used, if they have some influence on the beam polarization and how they are located relative to each other. This also shows the fundamental principle of the setup, separating spin-up and spin-down neutrons. Starting with an unpolarized beam from the monochromator we use a standard FRM II ^{3}He-filter to get a polarized beam. After being scattered by the sample, the beam again includes both spin directions (postulating that some spin-flip interaction took place). After the sample are some components used to get a well-defined beam (slits, PG-filter), as well as an additional collimator to restrict beam divergence. Further along the beam path are the core components of our setup, two neutron deflecting devices. These are used to spatially separate the spin-up and spin-down parts of the scattered beam. We use two deflectors to take the rather broad divergence of the neutron beam into account, as well as to improve on spin purity of the central beam which still contains spin down neutrons due to the not perfect reflectivity of the deflectors. Each beam component, one direct beam for spin-up and two deflected spin-down beams, hits one of three different analyzer blades. There the analyzer selects a specific energy range for each beam which is finally reflected towards the corresponding detectors of the multi-detector.

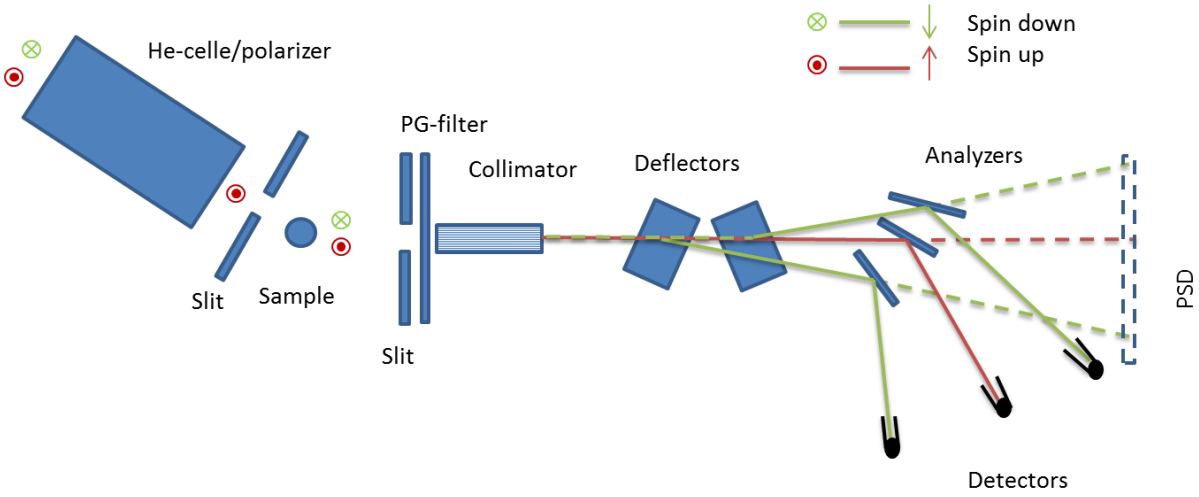

Fig. 8: Sketch for the polarization analysis setup at PUMA, excluding the monochromator. Shown here are the beam paths for both spin components along their way through the setup. On the right side both detector options are shown, three single detectors from the MD or, in dashed lines, the PSD.

These deflectors consist of multilayer stack of silicon wafers coated with the reflective FeSi layer. The silicon wafer by itself is mostly transparent for neutrons while the coating of the wafers transmits spin-up neutrons, except for very low angles, and reflects spin-down neutrons over a larger angular range. These components slit, PG-filter, collimator and deflectors, on the analyzer side of the

experiment are installed on an 80 cm long optical rail connected to the analyzer/detector box. In addition to the eleven single tubes of the MD there is also a position sensitive detector (PSD) available in the MAD setup. This detector can be used to monitor the beam profile during some steps of the installation process.

In addition to the components shown in Fig. 8 there are permanent magnet- and quasi-Helmholtz guide fields to preserve the spin stare of the neutron beam along its path from the polarizer to the spin-analyzer (deflector).

The geometry and performance of the setup depend primarily on the distances between the movable components. These are, on the optical bench, mainly the deflectors. The other relevant variable distance is between the center of the analyzer table and the sample table L_{SA}. In our experiments we typically choose L_{SA}=141 cm, L_{SD1}=61 cm and L_{SD2}=66 cm. $L_{SD1/2}$ are the distances between the sample and deflector ½.

We will now look at each component in detail, starting with the 3He-polarizer, followed by deflectors, collimator, guide field, and additional components.

Fig. 9 shows a photo of the complete PUMA polarization analysis setup with labeled components.

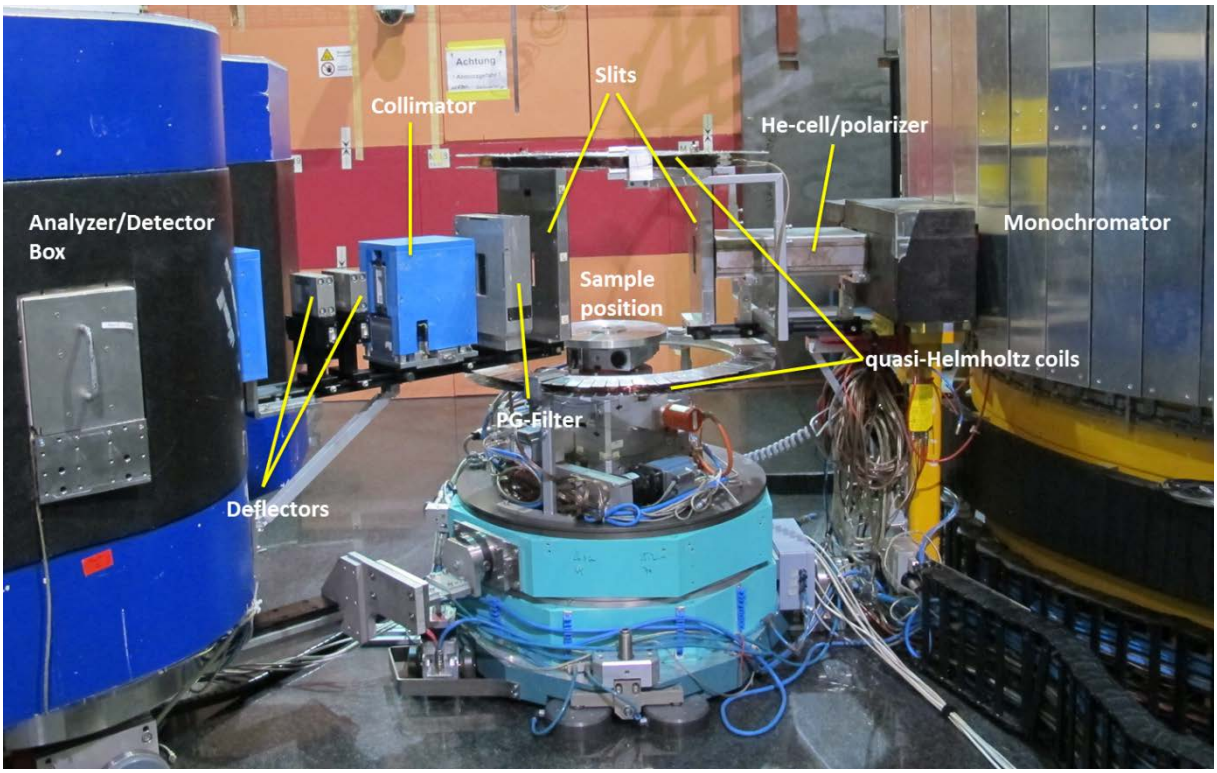

Fig. 9: Complete setup for polarization analysis at PUMA with all components installed.

3.1 ^{3}He-filter

For holding our ^{3}He filter cell we use a magnetostatic cavity that was formerly in use and provided by POLI[1]. The magnetostatic cavity/holding box is described in some detail in [8] as "Magic Box 2", or MB2. It consists of a Mu-metal framework with a series of permanent magnets on the sides and a PE holding structure for the ^{3}He-cell in its center. This cell produces a permanent magnetic guide field of about 18G to conserve the polarization of the ^{3}He-cell. Fig. 10 shows our guide field box holding a cell in. The cell is 130 mm long over all, of which 124 mm are gas volume, and with a diameter of 60 mm [9].

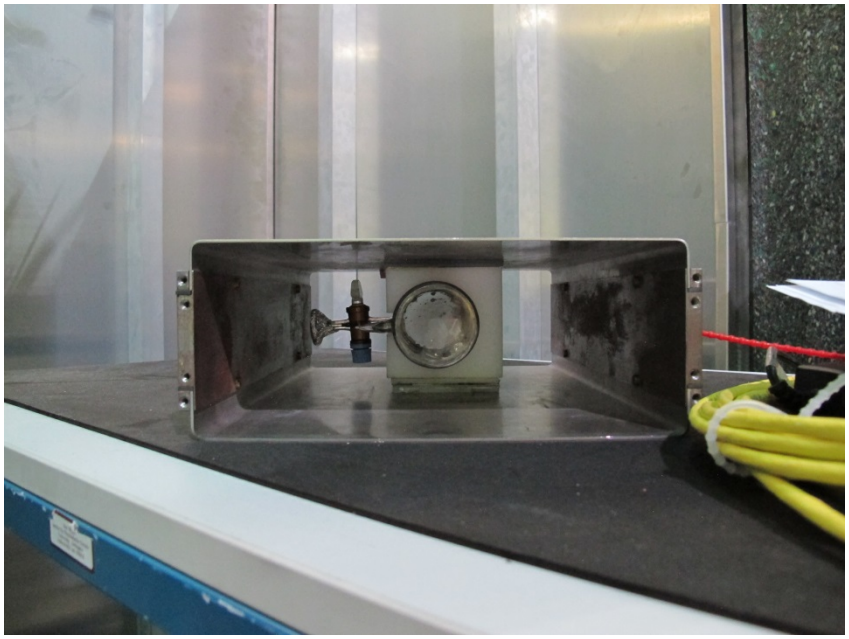

Fig. 10: ^{3}He-cell inside guide-field box. The box holds the cell in position and provides a homogeneous permanent magnetic field to preserve the spin polarization of the helium.

Our ^{3}He cells are polarized at the HELIOS facility, working by the MEOP (metastability exchange optical pumping) principle. This means that a low pressure ^{3}He gas gets exited from ground state into the metastable 2^3S_1 state and then optically pumped by circular polarized light. Thereby the photons angular momentum is transferred to the helium electron shell resulting in a nuclear polarization. All of this is done under the influence of an external magnetic field hold polarization in place. Afterwards the polarized gas is compressed up to the required cell pressure. See [10].

Furthermore the cell is characterized by its gas parameters, the important ones being pressure and polarization of the helium. With this information the resulting beam polarization can be calculated as shown further down in this section.

The filter selects neutrons with spins oriented vertically (z-direction) due to the orientation of the ^{3}He-cell box guide-field. SF-scattering changes the spin orientation of neutrons in anti-parallel to the guide field. This orientation towards -z-direction is conserved along the remaining beam-path by magnetic guide fields until after the beam is split up into its spin components by the deflectors.

For polarized ^{3}He we have an absorption cross-section of $\sigma_{abs}(\uparrow\uparrow)\approx 0$ b for parallel and $\sigma_{abs}(\uparrow\downarrow)=10666$ b for antiparallel incident neutrons with a velocity of v=2200m/s (or $\lambda_0 = \frac{h}{m_n v_0} =$

[1] POLI is the polarized hot neutron diffractometer directly located adjacent to PUMA at FRM2

1.798 Å). Here m_n is the neutrons mass, h the Planck constant and v_0 the neutron velocity. In addition we have $n_{He}^{tot} = \frac{p}{k_B T}$ He particle density in our cell. With this we can calculate the opacity of our cell which we need to find the spin dependent transmission of our ^{3}He-filter. For this we further use that $\sigma_0 \frac{p_0}{k_B T} \frac{1}{\lambda_0} = 0.144\ cm^{-1}\text{Å}^{-1}$ where $\sigma_0 = \sigma_\lambda \cdot \frac{\lambda_0}{\lambda}$ is the unpolarized absorption cross section. From this we get that

$$\sigma_\lambda n_{He}^{tot} = \sigma_0 \cdot \frac{p}{k_B T} \frac{\lambda}{\lambda_0} = 0.0732 \cdot p \cdot \lambda\ cm^{-1}\text{Å}^{-1} bar^{-1} \quad (1)$$

with *p* being the cell pressure inside in bar, and. The factor of 0.0732 results from spin dependent absorption cross-section (σ_{abs}) and particle density of the helium. Note that σ_{abs} is proportional to neutron wavelength.

This gives us the opacity of a ^{3}He-cell

$$\eta = 0.0732 \cdot p \cdot l \cdot \lambda \quad (2)$$

with *l* the length of the cell in cm and λ the neutron wavelength in Å.

From the opacity we can calculate terms for the spin dependent transmission for our filter cell:

$$T_\uparrow = \frac{1}{2} \cdot e^{-\eta \cdot (1 + P_{He})} \quad (3)$$

$$T_\downarrow = \frac{1}{2} \cdot e^{-\eta \cdot (1 - P_{He})}$$

The most important parameter for a polarization setup with a helium polarizer is the polarization of the incident beam. Incident beam polarization depends on the time-dependent polarization of the helium inside the cell which can be described by

$$P_{He}(t) = P_{He}(0) \cdot e^{-t/T_R} \quad (4)$$

$P_{He}(0)$ is the starting polarization of the cell, *t* elapsed time since the cell was polarized, and T_R the relaxation-time of the cell.

The helium in the cell is losing its polarization primarily by collisions with the cell walls and by magnetic in-homogeneities. Hence a very homogenous guide field, as provided by the magnetostatic cavity, is necessary to archive a long relaxation time. In addition, every change of the magnetic environment, such as during the insertion of a new cell into the holding box, or a change in the guide

field provided by the quasi-Helmholtz coils, has to be done very carefully. The magnetic environment of our setup gives T_R in the order of 100 h, see the following subsection.

Polarization of a given neutron beam can be described by

$$P_0 = \frac{N_+ - N_-}{N_+ + N_-} \tag{5}$$

Here N_+ is the number of neutrons with a spin oriented parallel to the field, called up neutrons, while N_- is the number of neutrons antiparallel to the field, the down neutrons.

Now the time dependent polarization of the incoming beam is given by

$$P_n(t) = \tanh\left(\eta \cdot P_{He}(0) \cdot e^{-\frac{t}{T_R}}\right) \tag{6}$$

Even if the incident beam polarization is measured directly (see 4.3.1 for one option using a spin flipper) it is easier to use calculated polarization values for data evaluation. Especially for long scans where checking beam polarization during the scan may not be an option a calculated value is a good alternative to a measured polarization. Nevertheless checking calculated polarization by a measurement is always a good idea if the experiment allows time for this.

To select the right cell parameters it is necessary to understand how many neutrons are absorbed by the polarizer. For this we need to know the transmission of a ^{3}He-cell which is given by [11]

$$T_n = T_0 \cdot e^{-\eta} \cdot \cosh(\eta \cdot P_{He}) \tag{7}$$

Using these expressions it is possible to calculate polarization and transmission of a given polarizer-cell. Fig. 11 shows an example for a 13cm long cell, with an initial helium polarization of 75%, and a neutron wavelength of 2.36 Å.

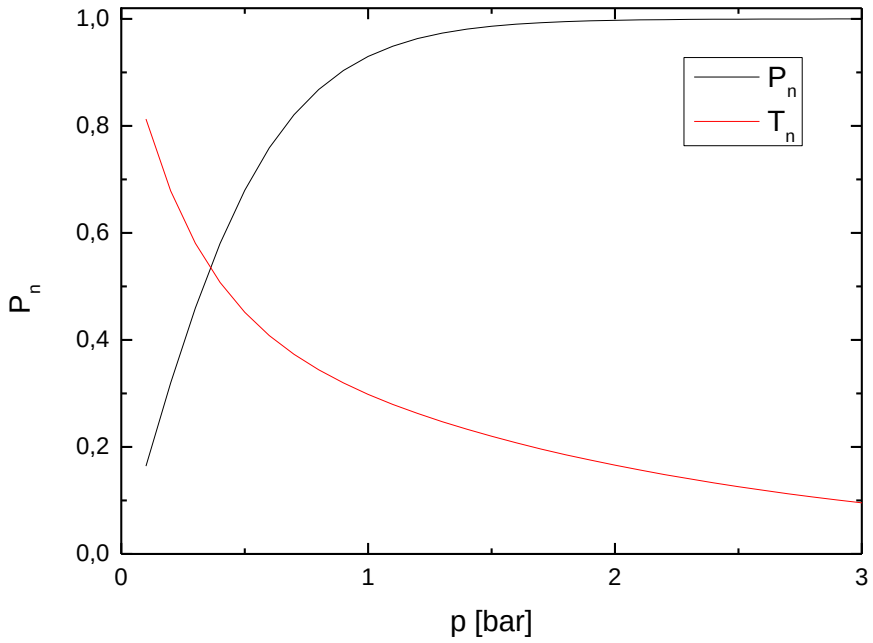

Fig. 11: Polarization of incoming beam and neutron Transmission in relation to cell pressure for a starting cell polarization 0.75

For a cell with these characteristics going from a pressure of 1 bar up to 1.5 bar results in a loss of over 35% of transmitted neutrons with a gain of only 5.5% in beam polarization.

When we take a look at the ^{3}He-cell transmission separated by spin state, using equation (3) we get the plot shown in Fig. 12.

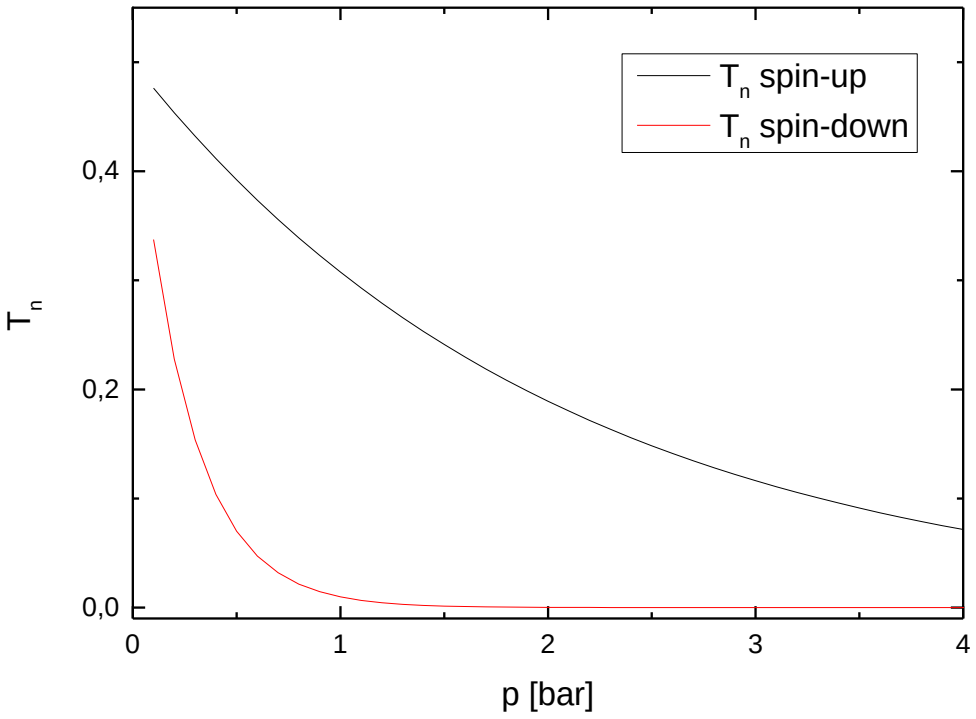

Fig. 12: Transmission of spin up and spin down neutrons for a standard He-cell with 78% He-polarization dependent on cell pressure

Note that below 1 bar the transmission for spin down neutrons starts to rise, for a cell with P_{He}=75%. For maximal neutron intensity without loss of neutron polarization a cell with p of 1 bar is advisable. If the goal is highest possible polarization a cell pressure of slightly above 1.6 bar should be sufficient as there is no gain in spin-down absorption for higher pressures.

3.1.1 Relaxation time in the PUMA polarization analysis setup

For data reduction, the relaxation time T_R (see equation (4)) of the ^{3}He-cell used in the experiment is needed. For the PUMA polarization setup the standard ^{3}He cells of the FRM II, also used by POLI and described by Hutanu et al. [9] is utilized. As the paper already characterized the cell one could use the relaxation time given in this publication. But as the PUMA setup has its own unique magnetic environment it is better to check the relaxation time for its specific magnetic environment.
The relaxation time of the ^{3}He-cell can be determined experimentally by measuring the polarization of the incident beam over time. There are several possible ways how to execute such a

measurement. It can either be done by using the direct beam without a sample or by measuring a reflection of a sample without a spin-flip (SF) component, such as a lattice reflection. Furthermore it is possible to use the full polarization analysis setup, comparing the signal of the three single detectors. Or, as another valid option using the PSD by integrating the intensity over the channels associated with the three component beams.

To get the relaxation time estimated incident beam polarization is fitted with a decay law of the following form:

$$P_{He}(t) = P_{He}(0) \cdot e^{-\frac{t}{T_R}} \tag{8}$$

To give an example, in August 2016 we used the direct beam, PSD, and no sample. The resulting measurement and fit are shown in Fig. 13.

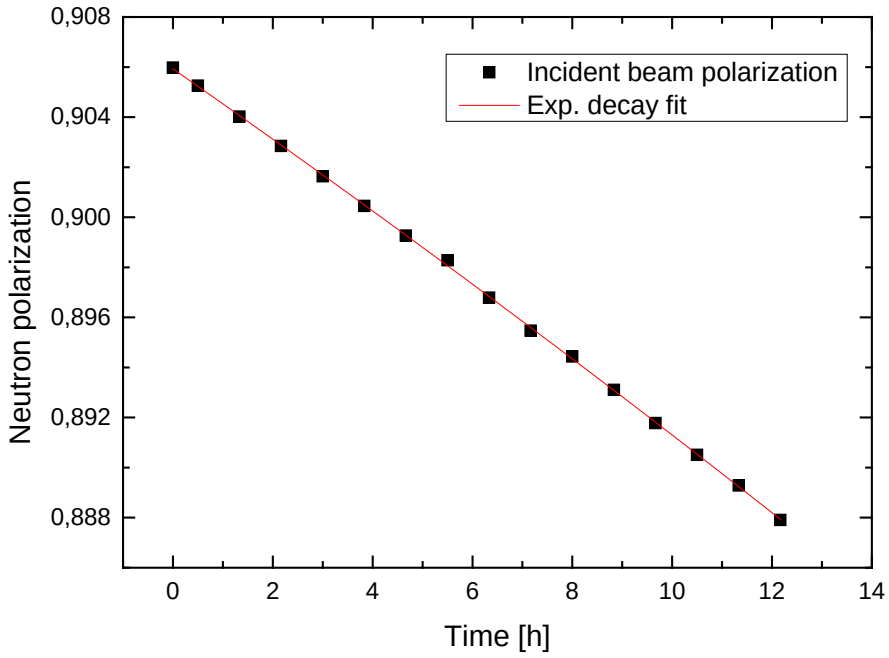

Fig. 13: Exponential decay fit to incident beam polarization during the August 2016 experiment. The observed relaxation time was T_R=100(22) h, with the large error resulting from the comparatively short time interval considered here

But doing regular control scans over a lattice reflection between other scans offers several additional benefits. It helps to confirm the calibration of the spectrometer, allows checking if something unexpected happened to the sample, and, as discussed, also gives us a set of data to calculate the

relaxation time for the specific experiment with using the described method. One only needs to fit the change in polarization that can be seen over time.

3.2 Deflectors

As already mentioned in the introduction to this chapter we are using two deflectors, obtained from Swiss Neutronics, to create multiple neutron beams. This is done to spatially separate spin-up and spin-down neutrons.

They are formed by a stack of 36 coated silicon wafers. Each wafer has a thickness of d=0.55 mm, a length and height of 40 mm resulting in a 20x40 mm^2 beam cross section. The coating of the wafers consist of a FeSi layer with *m*=4.5. Neutron supermirrors are characterized by their *m*-value, defining their wavelength dependent critical angle

$$\Theta_C = 0.099 m \lambda \tag{9}$$

θ_C is in degrees and λ in Å. For cold neutrons with λ≈5Å the critical angle for natural Ni is defined as *m*=1. To reach higher angles one could choose a pure isotope, such as ^{58}Ni, which has a higher neutron scattering length density compared to natural Ni resulting in m=1.18. But this approach cannot reach the high m-values provided by neutron supermirrors. Today supermirrors with *m*-values up to *m*=8 have been realized, see [12, 13].

Each deflector unit also has its own vertical magnetic guide field provided by permanent magnets with B=60 mT.

The deflectors work as a stack of polarizing neutron supermirrors, with different reflectivity curves for spin up and down neutrons. This is a result of spin dependent reflectivity. Spin dependent refractivity for neutrons has a nuclear (n_N) and magnetic (n_M) component and depends on the neutron being parallel (+) or anti-parallel (-) to the applied magnetic field:

$$n_{\pm} = n_N \pm n_M = 1 - \frac{N\lambda^2}{2\pi}(b \pm C\mu) \tag{10}$$

N is the atomic number density, b coherent scattering length, μ average magnetic moment per atom and C a constant of $0.2645 \cdot 10^{-12}$ cm μ_B^{-1}. See [14].

A combined reflectivity curve for our two deflectors is shown in Fig. 14.

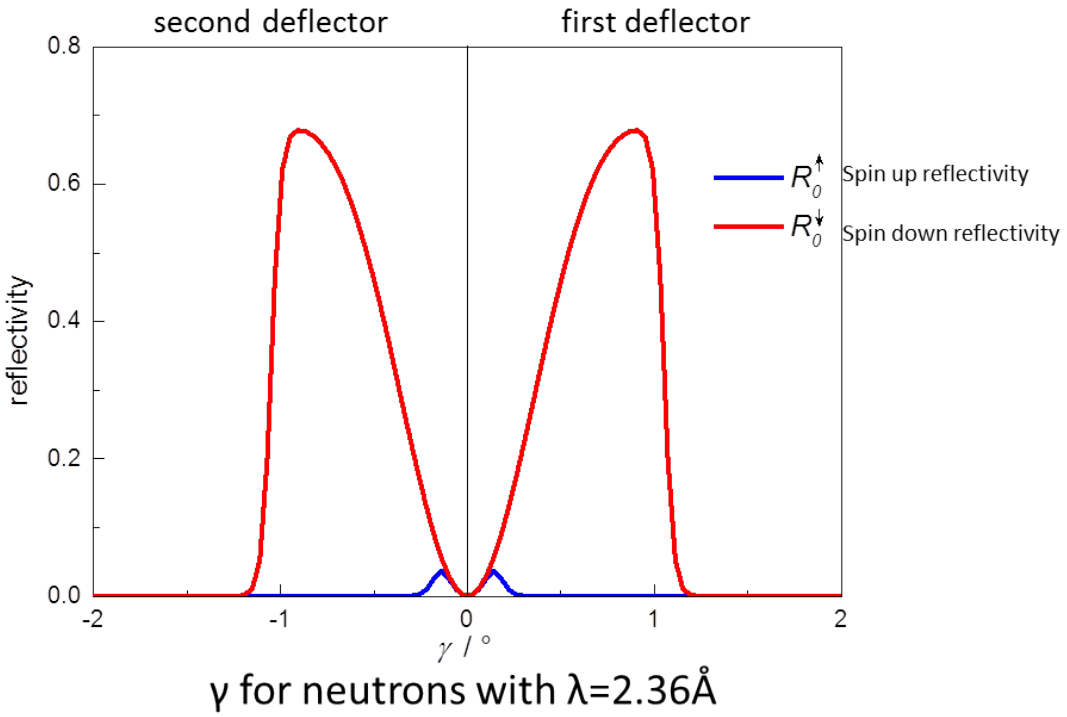

Fig. 14: Reflectivity curves of our two deflectors showing the spin dependence of their reflectivity. Details for the somewhat complicated form of the curves are given in the text.

Shown are the reflectivity curves for spin-up and –down neutrons. In the reflectivity curves plot γ is the tilt angle between deflector and beam, given for a wavelength of 2.36 Å. This wavelength is often used for inelastic neutron experiments in a constant-k_f configuration because of the benefits of PG-filters, see section 3.5. The plot also illustrates that spin-up neutrons are only reflected for small angles (<<0.25°) and even then only in a small amount (below 5%). The figure shows a reflectivity curve for two identical deflectors placed in front of each other and with opposed tilt angles. This is done to optimize the separation of spin states and explained in some more detail in section 3.2.1. The reduction in reflectivity for angles lower than 1° is the result of our deflector being a stack of mirrors that work like a collimator for small enough incident angles. This leads to a loss of neutrons as some never hit one of the mirror planes, for an only slightly tilted deflector, but passing between them. Because of their construction from a stack of coated Si wafers the deflectors also work as a collimator, as we have the basic layout of a neutron collimator. The Si wafers themselves are mostly transparent for neutrons, and the coating works as a collimating sheet. This means that for small incident angles incoming neutrons have a chance to travel though the deflector without hitting a mirror coating. This results in the dip in the center of the Fig. 14 reflectivity curve. As our deflectors are 40mm deep and the wafers have a thickness of 0.55 mm a simple geometric calculation gives us a

collimation of 47’ or 0.79°. In addition this effect can be observed by rotating a deflector in the beam, for example during its calibration, see chapter 7 “Handbook for the PUMA polarization setup”. When the deflector wafers/coatings are perfectly parallel to the incident beam there is a sharp intensity spike where almost all neutrons travel through the Si wafer material. An example of this is shown in Fig. 75, found in the appendix.

Overall there are four deflectors available, with each deflector having its own stepper motor drive to vary its tilt angle. The motors and deflectors were assembled in the chemistry workshops of the University of Göttingen and there are slight differences in the characteristics of each unit. The number of the deflector is written on the motor/slider holding the deflector. There are also small differences between the deflectors for transmission as shown in Table 2. Probably these differences are the result of some small deviations during the manufacturing process, and most likely due to not perfectly parallel wafers. This leads to the conjecture that deflector 2 and 3 have the most parallel oriented wafers. Because of this the use of deflector two and three is preferred.

The order of deflectors also has some influence on the resulting beam profile. As shown in Fig. 72 in the appendix some combinations of deflectors result in small additional side peaks. The effects resulting in this phenomenon are currently not fully understood, but it is assumed that a chance combination of small manufacturing imperfections is to be blamed. Nevertheless this should be noted as a known occurrence for future reference.

Deflector	Transmission	Angular range [°]
1	0.824	-4,17..4.78
2	0.849	-4.29..4.56
3	0.837	-4.34..4.47
4	0.793	-4.39..5.07

Table 2: Neutron transmission and angular movement range for the four available deflectors at PUMA

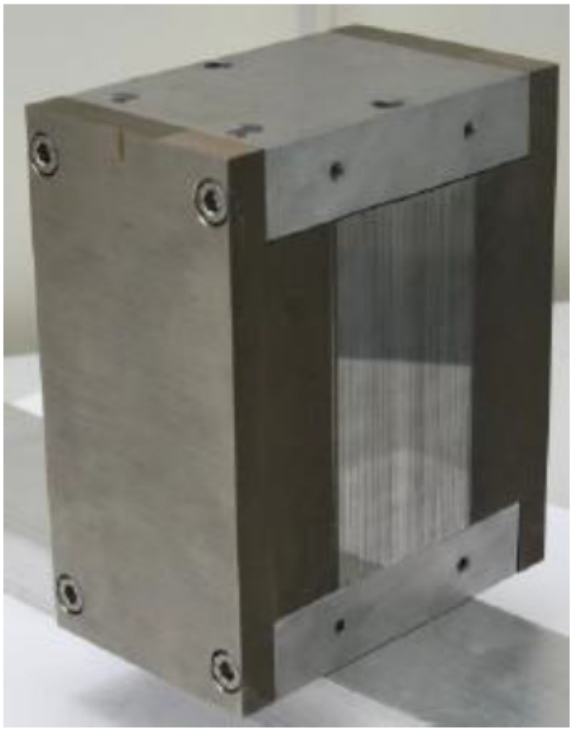

Fig. 15: Photo of one deflector without its stepper motor. The silvery sheets in the center are the coated wafers

In Fig. 15 a photo of one of the deflectors, without slider and stepper-motor is shown.

3.2.1 Why we use two deflectors

In this setup we use a pair of deflectors to separate the spin components of the scattered beam. As the use of a second deflector produces a third beam and thus increases the complexity of the experiment some explanations for this choice are in order.
Using only one deflector would lead to some loss of intensity. There are two main reasons for this. The first is the divergence of the scattered beam, which is somewhat wider than a single deflector at a typical deflector position. The second reason is the non-perfect reflectivity of our deflectors. As there are some spin down neutrons that are simply transmitted through the first deflector a second deflector gives us a second chance to still separate these from the direct beam.

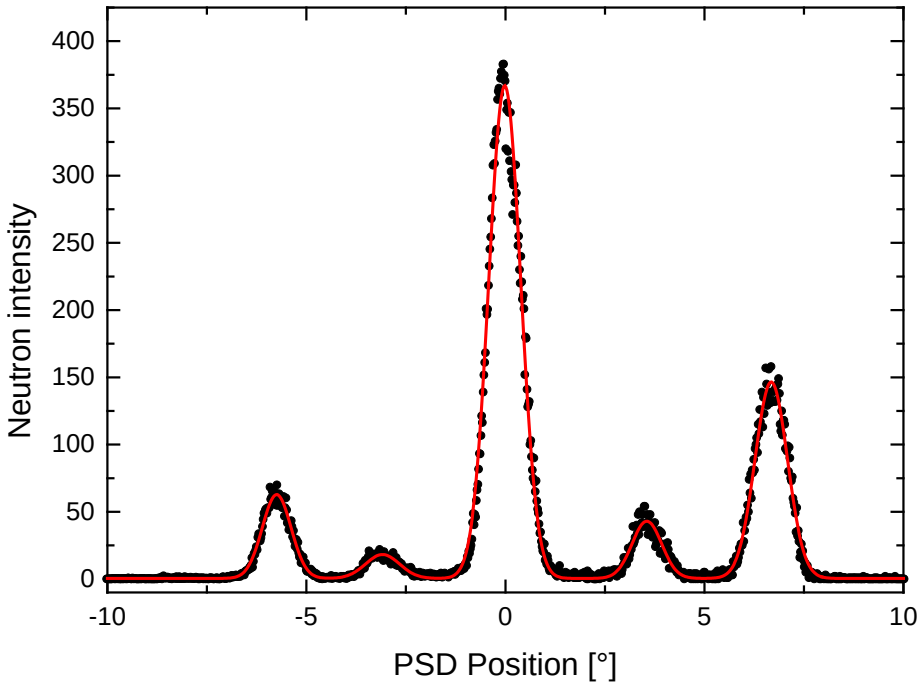

Fig. 16: PSD beam profile using four deflectors. This image is a composite of two exposures, as the PSD has only an angular range of 6-7°. The position is relative to the central beam, not centered on the PSD.

The use of more deflectors, meaning up to four, was also tested. Besides making an already complex system more complicated the main problem with this approach is that it yields not more, but less intensity than the two deflector approach.

A PSD image of the beam profile when four deflectors are used is shown in Fig. 16.

An image using three deflectors can be found in the appendix, page 143 Fig. 73 and the preferred two deflector setup is shown in Fig. 17.

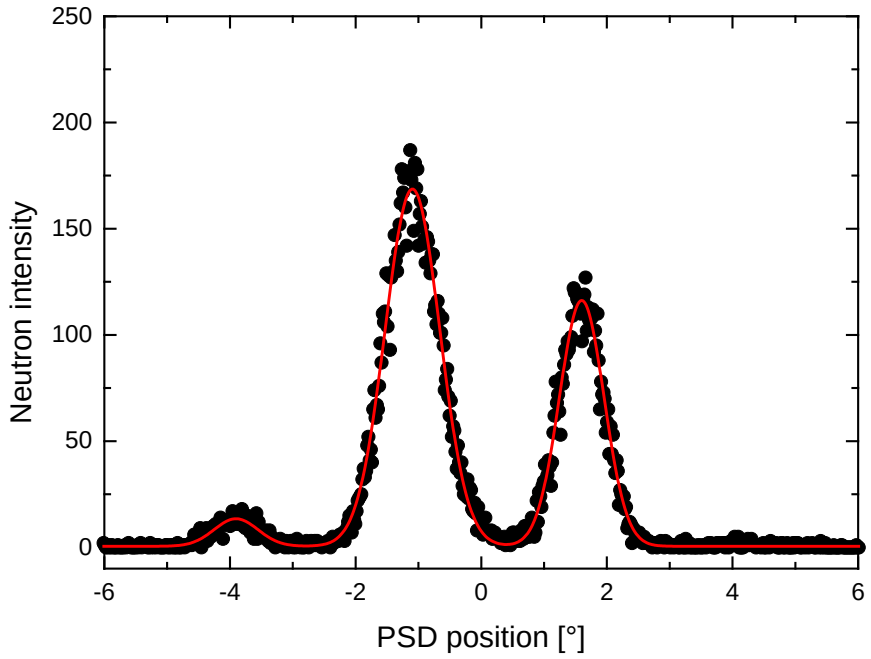

Fig. 17: PSD profile for two deflectors. The 0° position is the PSD center and is not identical with the optical axis

The integrated intensities for the four deflector image are from left to right: 56, 19, 367, 40 and 150 in arbitrary units. For the two deflector setup we get intensities of 66, 408 and 264 for the three component beams. This gives us a deflected/direct-beam ratio of 0.72 which is somewhat worse than the ratio of 0.81 for two deflectors.

The idea behind using more deflectors was to gain in deflected intensity by getting a larger part of the scattered beam to hit a deflector, and by giving neutrons that passed a deflector without being redirected, due to the reflectivity of our deflectors being <1, a “second chance” or even third and fourth one. What we see in testing this approach is a loss of overall neutron intensity (as each deflector also absorbs a small number of neutrons, see Table 2) of over 14%, a loss in relative deflected neutrons and a much more complicated setup.

Using more deflectors also means using more detectors and their full counting chains with all the possible associated electronic problems and finally a higher impact of electronic background.

The same problems we found for four deflectors are, for a lesser extent, also true for three. There is only a minimal gain in overall intensity which is outweighed by the associated problems. Using two deflectors seems to be an optimal compromise. But even using only two deflectors it can be beneficial to ignore the lower intensity deflected beam. This can be true for measurements with

overall low intensity. In this case the lower intensity side channel still adds to intensity, but the channel adds background so that the signal to noise ratio for the combined SF channel gets worse. This is further discussed in 5.5 “Copper (II) oxide”.

3.2.2 Positioning of the deflectors

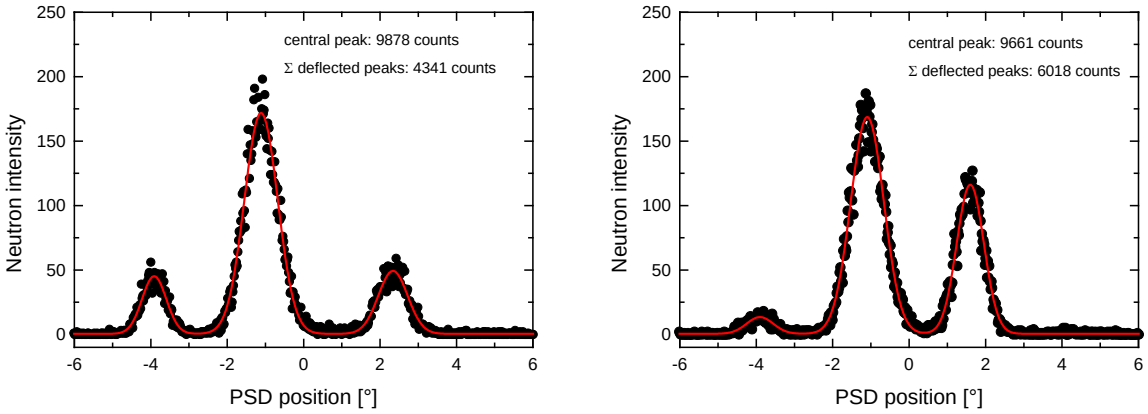

Fig. 18: Optimization of the deflector orientation. On the left is an example of our first trial using symmetrical deflected signals. On the right an example for asymmetric side peaks showing an intensity gain of around 10%

When positioning the deflectors we have to consider their distance to the analyzer center, as well as their tilt angle towards the neutron beam.

In our first setup we tried to produce deflected beams of nearly identical intensity. The naïve reason for this was the assumption that a symmetrical setup would be optimal, with the symmetry of the beam profile as point of orientation. This lead to a small loss of overall intensity and also resulted in a large drop in deflected beam intensity. A scan with symmetrical side peaks compared to the optimized asymmetrical setup is shown in Fig. 18.

Considering the reflectivity curve of our deflectors it is easy to understand why a setup with symmetrical intensity in the deflected beams is less than optimal as it leads to a tilting angle of the deflectors bigger than the optimal critical angle. This results in a lower reflection probability and with this a loss of reflected neutrons and overall intensity.

Placement of the deflectors on the optical rail should be 80 cm from the analyzer center for the first, and 75 cm for the second deflector. This gives us a spatial separation of the beams at the analyzer location so that we can move an analyzer into each beam just by translation.

When the deflectors need to be placed again it is recommended to orient on the analyzer center, as the sample analyzer distance will vary somewhat with each new installation. As the deflectors are mounted on an optical rail connected to the analyzer/detector-box the analyzer center is a fixed point of reference for them. In contrast to this the distance between sample and deflector is not fixed, as the coupling between sample table and analyzer/detector lacks a mechanical fix-point. The optimal angle for the deflectors is between 0.75 and 0.8° as found by analytical calculations, as well as by experimental experience. For this see chapter 4.3.1 “Analytical calculations for PUMA polarization analysis”.

3.3 Collimator

As the divergence of the scattered beam must be adapted to the reflectivity profile of the deflectors an additional collimator is set up on the optical rail between sample position and the deflectors. If the beam-collimation reaching the deflectors is too relaxed a good separation of the spin components can no longer be achieved. Without the collimator the central beam gets too broad and starts to “flow over” into the zones occupied by the analyzers intended for the reflected intensity. If this happens the detectors for the side peaks are no longer spin state pure which renders our method useless. To avoid this two different collimators are available, with 15’ and 30’ divergence. As expected the 30’ collimator gives us a higher neutron flux without broadening the deflected beams too much. This is shown in Fig. 19. The 30’ collimator gives a gain of roughly 60% intensity in this test measurement.

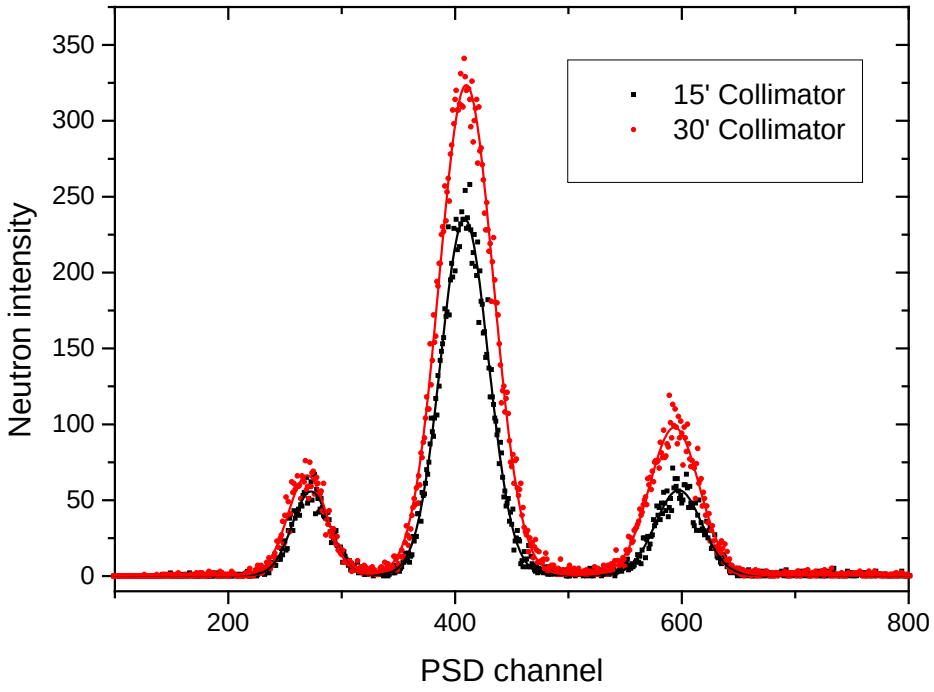

Fig. 19: Comparison of 15‘ and 30‘ collimator beam profiles showing intensity gain by using the rougher 30’ collimator while still preserving good beam separation. Note that this measurement used an early, suboptimal, configuration. This can be seen in the low count-rate of the right side peak, as well as the wide separation between central and right beam. From this one can conclude that deflector 1 had a larger than optimal incident beam angle.

Still, if one wants to use finer collimation the 15’ collimator is available. The selected collimator is installed right after the PG-filter and in front of the deflectors. Both devices include their own vertical guide field provided by a series of permanent neodymium magnets of roughly 60 mT is inlaid in the frames holding the collimator. In addition to this they have stepper motor drives to rotate them in the x-y-plane so that they can be aligned to the beam.

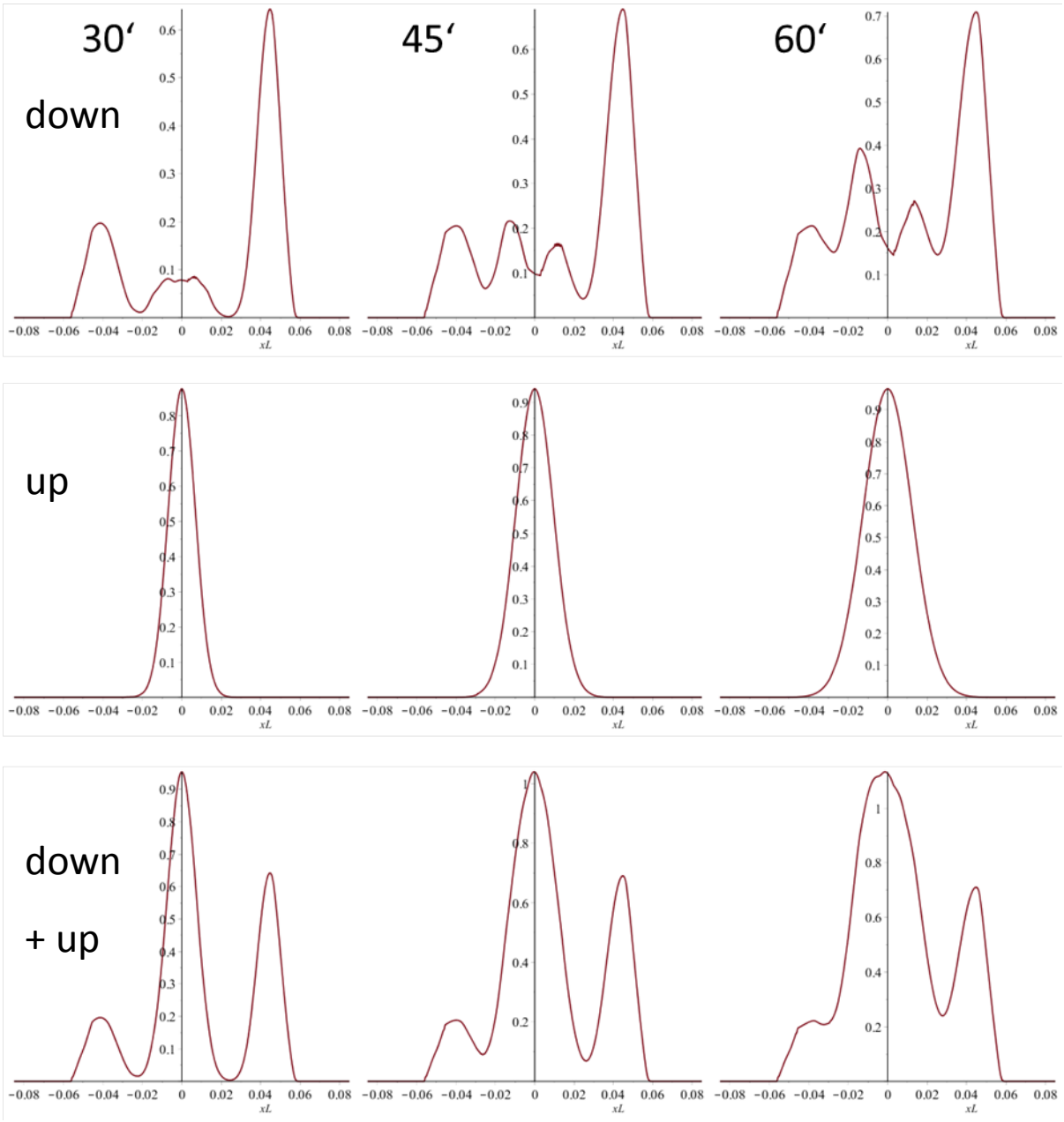

Fig. 20: Calculations for intensity distribution at PSD position. X-axis is PSD position in m, y-axis intensity in arbitrary units. From top to bottom the profiles for spin-down neutrons, spin-up neutrons and both spin directions are shown. From left to right, for a 30’, 45’, and 60’ collimator

Fig. 20 shows calculations for the intensity distribution at the PSD using the formalism shown in chapter 4.3.1. For these calculations deflector angels of +/- 0.8° where used, as well as sample deflector distances of 55 cm for the first, respectively 60 cm for the second deflector. We also used to simulate a 2 cm diameter sample to take into account that after scattering the neutron can have some angular divergence respective to the optical axis as well as geometric effects resulting from the sample acting as a source.

For 30' collimation we see a clear separation between the three peaks, as well as a small spin-down component in the central beam.

With the 45' collimation the three beams start to flow into each other, which results in a small contamination of the side peaks with spin-down neutrons. This could still be avoided by lateral displacing the analyzers, but then they will also wander out of the highest intensity region. For estimation, the projected width of a given analyzer is roughly 2 cm as given by the distance of neighboring rails of the MA. This means that we need 2 cm of uncontaminated spin-down intensity in the side peaks for our measurement. The side peaks gain around 5-7% in peak intensity, but at the same time the analyzers need to be placed somewhat off-center to stay spin-state pure. In addition the central beam gains proportionally more spin-down contamination; so much that there is more spin-down intensity there than in the second deflected beam.

If we now look at the 60' collimation this effect is even more pronounced. Now we have still more spin-up intensity in the central channel, and it becomes completely impossible to guarantee spin state pure deflected beams without a big loss in flux, as well as a needlessly complicated analyzer setup compared to the option of a tighter collimation.

Obviously the use of collimators is associated with a reduction of intensity. But due to the geometric restrictions of the MAD analyzer blades this effect is a minor concern.

3.4 Guide Field

As mentioned in the corresponding subsection some components of the polarization setup already have their own vertical guide field provided by a series of permanent magnets. These are the He-cell/polarizer, the additional collimator and the deflectors. After the deflectors a further guide field is no longer necessary as spin states were spatially separated while their spin orientation was still conserved by the guide field. If anything happens to the spin state of a neutron after the second deflector this has no influence on the experiment as the analyzer/detector system doesn't discriminate between spin states.

Besides the need for a guide field to preserve the spin state of the neutron beam there is also the need to shield the experiment from external stray fields. These include fields from magnetic systems used in other, neighboring, experiments, from electrically powered systems in the experimental hall, such as the crane, as well as surprisingly strong remnant magnetic fields originating from the floor of the experimental area. We found fields of up to 0.6 mT under PUMA on ground level and still around 0.1 mT at beam height. This is shown in Fig. 74 in the appendix.

From August 2016 onwards a guide field of up to 2.2 mT for a current of 7 A is provided by our new pair quasi-Helmholtz[2] coils. This set of coils allows free access to the sample table and a very easy way to install and manipulate even bulky sample environments. In addition this construction allows us to extend the optical benches as close as possible to the sample and gives a continuous guide field with smooth field gradients along the beam path.

In day to day operation the guide field is limited to a maximum current of 5 A for power source reasons. This gives us a guide field of 1.8 mT which is still much stronger than the normal magnetic background.

[2] It is quasi-Helmholtz, as for a Helmholtz coil the distance between coils is identical to their radius. Our setup has a larger distance then radius, the reasons for which are shown later

3.4.1 Interlude: The PANDA guide field

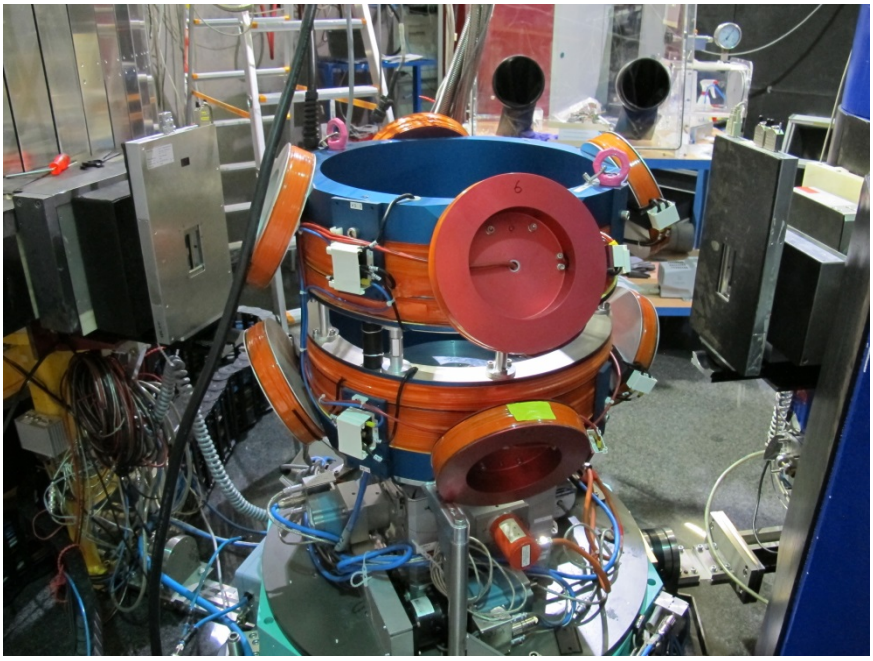

Fig. 21: PANDA guide field coils during testing. They turned out to be insufficient for our needs.

Before we started to work on our own guide field we asked of one of the other instruments could provide some help. As it turned out PANDA[3] had a set of guide field coils available which were not in regular use.

As some test showed this setup produces a rather inhomogeneous field of up to some 13 mT (see Table 8 as well as Table 9 in the appendix). We only tested the two main coils, up to I=10 A, as we were only interested in a vertical guide field for the next measurement cycle. After we saw how uneven the field distribution is it was decided to continue exploring the possibility of building a guide field along our own specifications.

An additional incentive was that the construction of these coils was very voluminous, making the handling of the coils and access to the sample table difficult. Furthermore the coils have some structural elements holding the upper coil in place which would block the beam while rotating the sample table. This was no problem for the intended use at PANDA, as the coil was to be stationary. For our setup, mounting the coils on our sample table, the whole system became freely rotatable. It would have been very difficult to take into account when one of the support stubs crossed the beam path during an experiment.

[3] PANDA is a cold neutron three axis spectrometer, also located at the experimental hall of FRMII in Garching

3.4.2 Calculations for the quasi-Helmholtz guide field

In addition to field strength the most important attributes of a guide field are good homogeneity in the shielded area, as well as soft transitions between different regions. During the development process we modeled our field in two ways: once by using a freely available finite element method program, FEMM 4.2[4], and then by doing analytical calculations for the field. The results where compared and our coils build according to the optimized parameters.
In the following we will take a more detailed look at the analytical approach and compare the results with FEMM models for some cases.

For reasons of simplicity we are using a cylindrical coordinate system as shown in Fig. 22, where r is the distance from the z-axis to some point, z is the height and φ the azimuth angle.

$$\boldsymbol{e}_{\varphi} = \begin{pmatrix} -\sin\varphi \\ \cos\varphi \\ 0 \end{pmatrix} \tag{11}$$

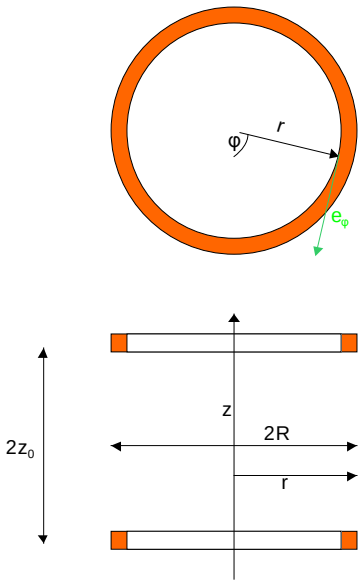

Fig. 22: Sketch for the coordinate system used in our Helmholtz coil calculations

[4] Available at http://www.femm.info/wiki/HomePage

A detailed derivation how we arrived at $\boldsymbol{B}_r$ and $\boldsymbol{B}_\varphi$ can be found in the appendix 8.1 on page 137. *N* is the number of windings for a given coil, *I* the current, $\boldsymbol{B}$ is a magnetic field, $\boldsymbol{A}$ a vector potential (see equation (129)), *z*, *z0, R* and *r* are explained in Fig. 22.

Here we will continue with

$$\begin{aligned}\boldsymbol{B}_r &= \frac{1}{r}\frac{\partial \boldsymbol{A}_z}{\partial \varphi} - \frac{\partial \boldsymbol{A}_\varphi}{\partial \boldsymbol{z}} \\ &= -\frac{\mu_0}{2\pi} NIR \int_{-1}^{1} dy \left(\frac{z - z_0}{\sqrt{z^2 - 2zz_0 + z_0^2 + R^2 + r^2 - 2rRy}^3} \right. \\ &\left. + \frac{z + z_0}{\sqrt{z^2 + 2zz_0 + z_0^2 + R^2 + r^2 - 2rRy}^3} \right) \frac{y}{\sqrt{1 - y^2}}\end{aligned} \tag{12}$$

and

$$\boldsymbol{B}_\varphi = \frac{\partial \boldsymbol{A}_r}{\partial \boldsymbol{z}} - \frac{\partial \boldsymbol{A}_z}{\partial \boldsymbol{r}} = 0 \tag{13}$$

From this we can take a closer look at some interesting point in our field. For the origin of our coordinate system, meaning the center of the guide field at z=0 and r=0, we get

$$\boldsymbol{B}_z(0) = -\mu_0 \frac{NIR^2}{\sqrt{z_0^2 + R^2}^3} \tag{14}$$

$$\boldsymbol{B}_r(0) = \boldsymbol{B}_\varphi(0) = 0 \tag{15}$$

To get a cross-section of our field we calculate the profile of *B* along our cylinder-axis by setting r=0. From this get:

$$\boldsymbol{B}_z(r=0) = -\frac{\mu_0}{2} NIR^2 \left(\frac{1}{\sqrt{z^2 - 2zz_0 + z_0^2 + R^2}^3} + \frac{1}{\sqrt{z^2 + 2zz_0 + z_0^2 + R^2}^3} \right) \tag{16}$$

As already mentioned, it is important to consider how big the homogeneous field area is, as well as how steep the change in field strength at the edges of the homogeneous zone. For this we calculate the first and second derivative of equation (16). The first derivative gives us

$$\frac{\partial B_z}{\partial z}(r=0) = \frac{3\mu_0}{2} NIR^2 \left(\frac{z - z_0}{\sqrt{z^2 - 2zz_0 + z_0^2 + R^2}^5} + \frac{z - z_0}{\sqrt{z^2 + 2zz_0 + z_0^2 + R^2}^5} \right) \tag{17}$$

which goes to 0 for z=0 and the second derivative

$$\frac{\partial^2 B_z}{\partial z^2}(r=0) = \frac{3\mu_0}{2} NIR^2 \left(\frac{1}{\sqrt{z^2 - 2zz_0 + z_0^2 + R^2}^5} + \frac{1}{\sqrt{z^2 + 2zz_0 + z_0^2 + R^2}^5} - \frac{(z-z_0)^2}{\sqrt{z^2 - 2zz_0 + z_0^2 + R^2}^7} - \frac{(z-z_0)^2}{\sqrt{z^2 + 2zz_0 + z_0^2 + R^2}^7} \right) \quad (18)$$

becomes 0 for $\boldsymbol{z_0 = \frac{R}{2}}$, as $\boldsymbol{\frac{\partial^2 B_z}{\partial z^2}(r=0) \underset{z=0}{\longrightarrow} \frac{3\mu_0}{2} NIR^2 \left(2 - 10 \frac{z_0^2}{z_0^2+R^2}\right)}$. This shows us that we have an enlarged area with a homogeneous magnetic field in direction for $\boldsymbol{z_0 = R}$ in comparison to a conventional Helmholtz setup with $\boldsymbol{2z_0 = R}$. This is shown in Fig. **23** for both analytical and FEMM calculations.

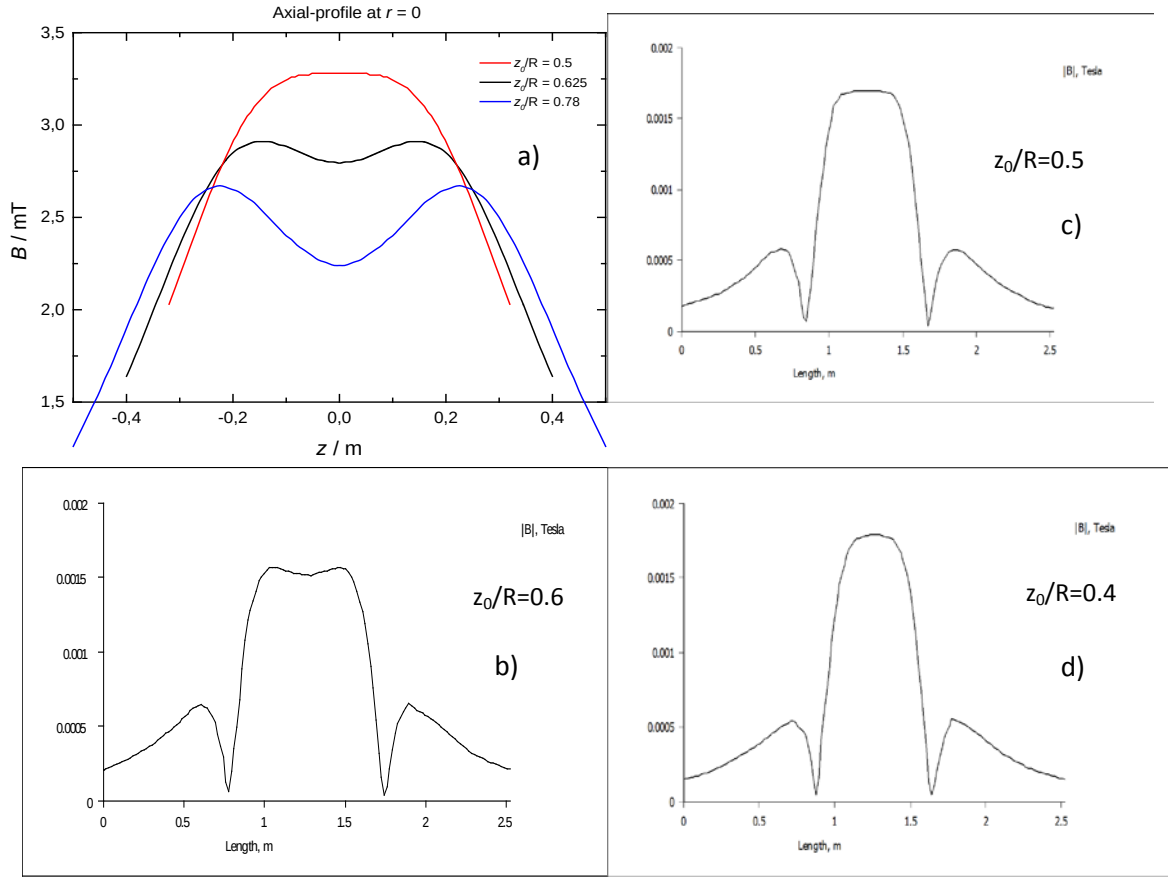

Fig. 23: Magnetic field profiles along r=0. On the top left are analytical calculations with a) showing the axial profile centered on the coil center; *B* is given as absolute value in mT. The other plots b)-d) are comparable FEMM profile calculations, but with *B* in T

Now we take a look at the radial profile of our magnetic field by looking at z=0. This gives us the field profile along our beam path.

Again using cylindrical coordinates (for a derivation in Cartesian coordinates see 8.1 “Intermediate steps for guide field calculations” in the appendix) we simplify our expression for $\boldsymbol{B}$ by considering it in two dimensions. This can be done by interpreting the field lines as contour lines of A_ϕ. Again the problem becomes two dimensional with B_ϕ=0, giving us

$$\boldsymbol{B} = \begin{pmatrix} B_r \\ B_z \end{pmatrix} = \nabla \times \boldsymbol{A} = \begin{pmatrix} \frac{1}{r}\frac{\partial A_z}{\partial \varphi} - \frac{\partial A_\varphi}{\partial z} \\ \frac{A_\varphi}{r} + \frac{\partial A_\varphi}{\partial r} - \frac{1}{r}\frac{\partial A_r}{\partial \varphi} \end{pmatrix} \approx \begin{pmatrix} -\frac{\partial A_\varphi}{\partial z} \\ \frac{\partial A_\varphi}{\partial r} \end{pmatrix} \tag{19}$$

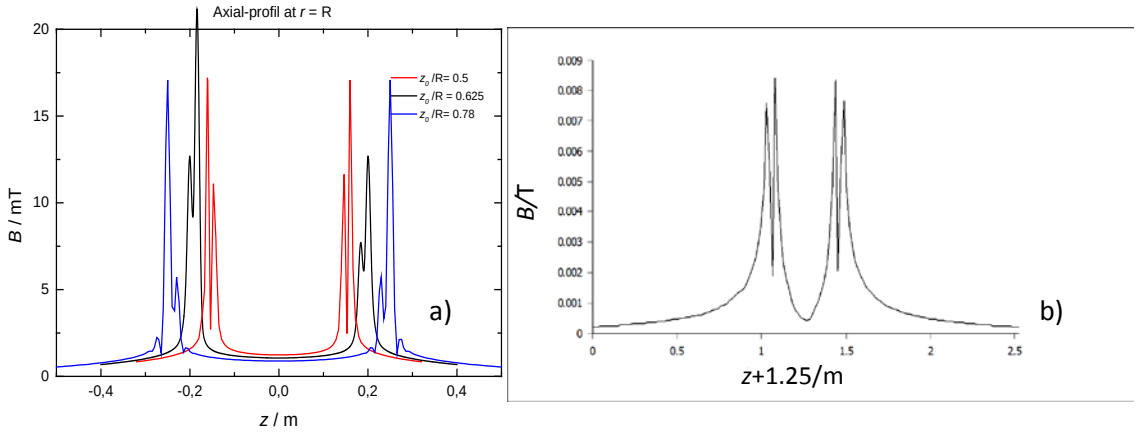

Fig. 24: Axial profiles of B at the coil edge. On the left, a), analytical for three different geometries and on the right once for z_0/R=0.5.

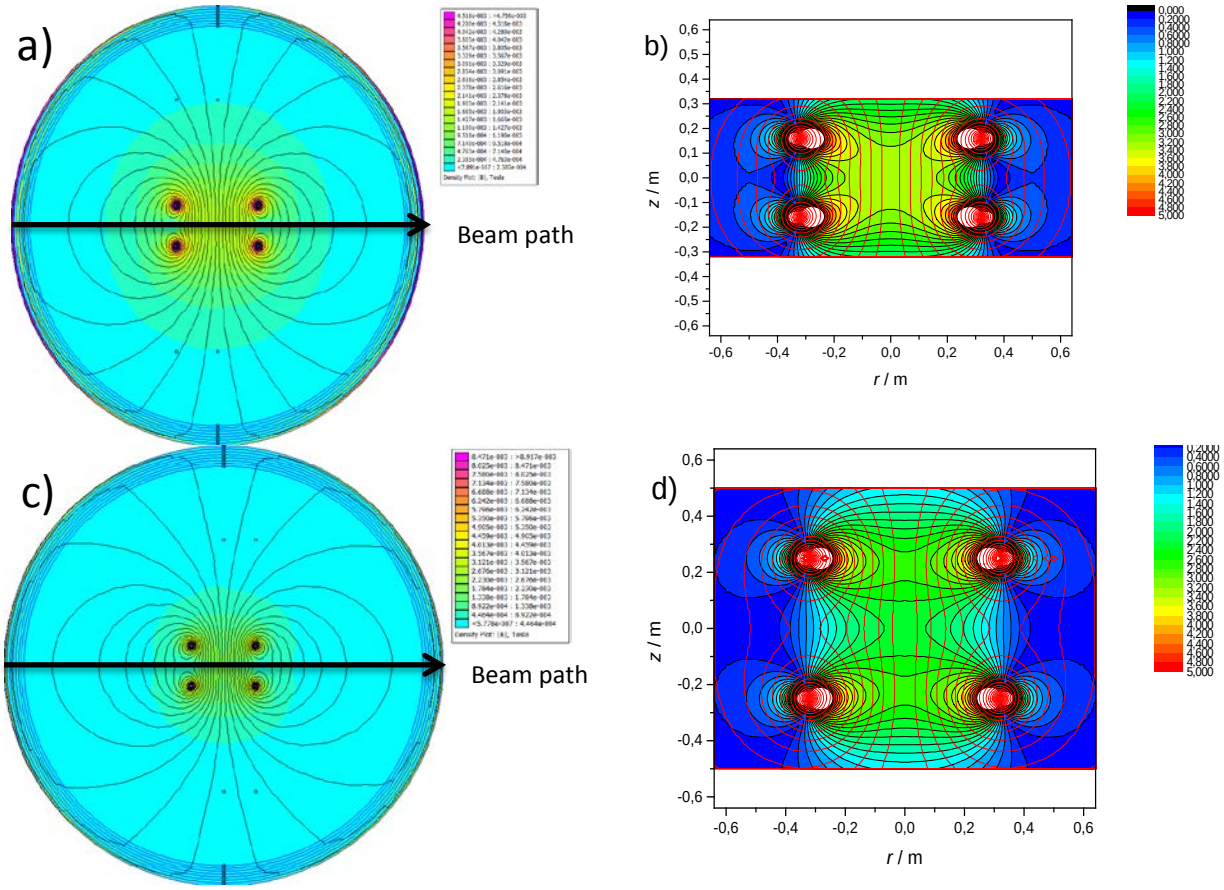

Fig. 25: Magnetic field distribution for several coil geometries in FEMM and analytical calculations. Here a) and b) show a geometry with $2z_0$=R and c) and d) z_0=R

In Fig. **25** the calculated magnetic field structure for different geometries is shown. The realized $\frac{z_0}{R} = 1$ geometry is shown in c) for FEMM simulation and d) for analytical calculations. Both show the same field distribution and strength, as well as an increased area of homogeneity in beam direction compared to the other shown geometries. In a) and b) have $\frac{z_0}{R} = \frac{1}{2}$, in which case the polarized beam would cross a stronger field gradient compared to the geometry shown in c)/d).

FEMM field strengths are in T while the numbers given for the analytical approach are in mT.

3.4.3 Construction of quasi-Helmholtz coils

After modeling our field we arrived at a quasi-Helmholtz configuration with $\frac{z_0}{R} = 1$ that should have around 200 windings and be capable of sustaining a current of 5 A.
Dimensions of the coils where adapted to the size of the sample table. Now the sample table guide field consists of a pair of coils with an inner diameter of 600 mm and an outer diameter of 640 mm. The wire windings are hold in place by a circle with a U-profile. As an interesting side fact, this fundamental structural component of the coils consists of two aluminum bicycle wheel rims. The upper and lower coils have a vertical distance of 500 mm. This makes the coils quasi Helmholtz, as an ideal Helmholtz setup would have a distance of $\frac{R}{2} = 300\ \mathrm{mm}$ between its coils. This enlarged distance gives us a larger homogenous field area, as well as better access to the sample

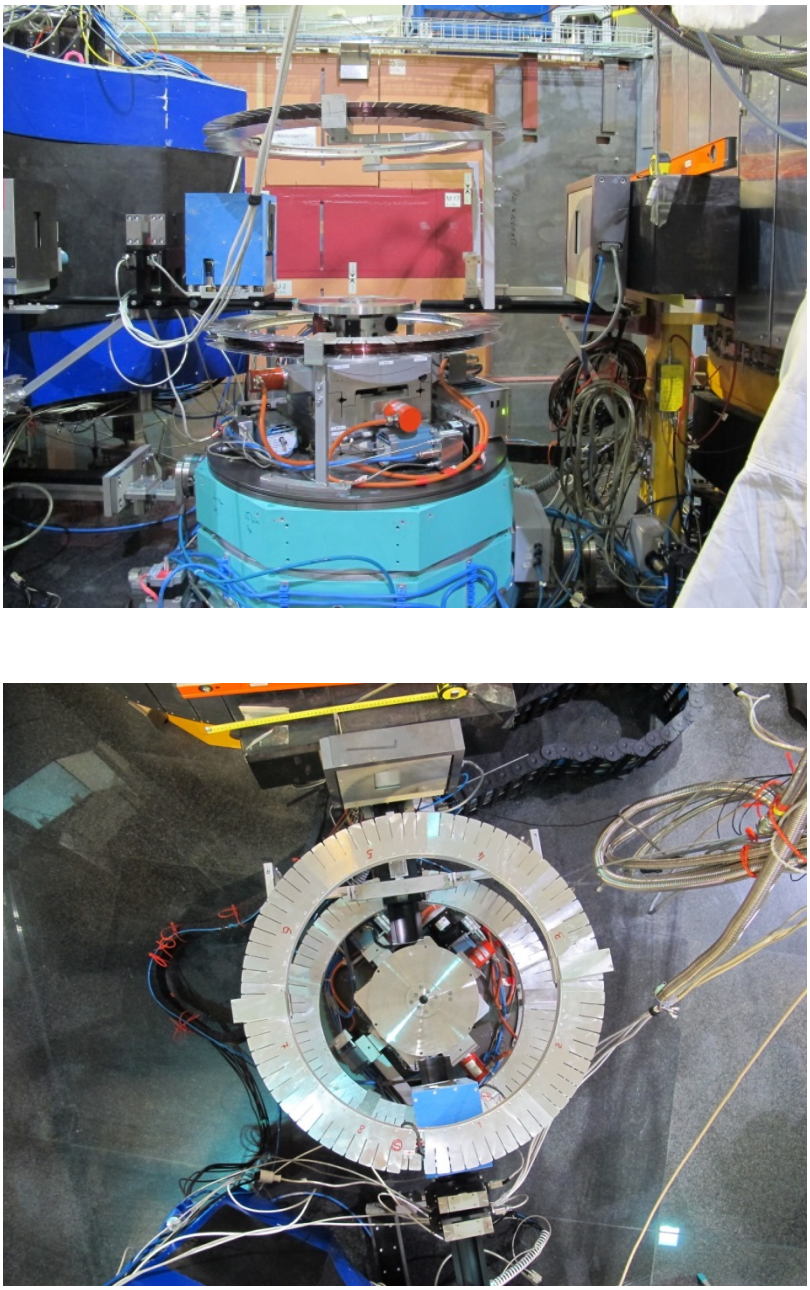

Fig. 26: Photos of the finished quasi-Helmholtz guide field.
Top: Photo of the guide field coils installed on the spectrometer. Note the Mounting for the upper coil fastened to the short optical rail and one of the three mountings for the lower coil fastened to the sample table.
Bottom: Look from above, showing the alignment of the coils and position of the collimator and the front mounting for the ^{3}He-cell inside the coils.

table.

Each coil has 134 windings of copper wire with a 4×1 mm^2 cross-section. Above and below the coils are a series of aluminum plates. These help to hold the windings in place and provide additional surface area for heat dissipation. In addition each plate has a number of notches. Originally it was planned to twist the small elements produced by the notches to create a radiator like structure to help with heat dissipation. For our normal setting with an electric current of 5-7 A the produced

waste heat turned out to be small (40 °C using 5 A) enough that this feature was not needed. The ohmic resistance of the coils is 1.3-1.4 Ω, and with an electric current of 5 A the coils produce a field of 1.8 mT at the sample position.

The upper coil is held in place by a mount on the optical rail on the monochromator side of the instrument, the same rail holding the ^{3}He-cell. The mounting can be seen in the upper left photo of Fig. 26.

The lower coil is held in position by three support struts connected to the sample table.

The support struts of the lower coils are shown in the upper row photos of Fig. 26.

3.4.4 Result

Some initial tests were done by placing some permanent magnets of various strengths at the sample position. The experimental setup consisted of the ^{3}He polarizer cell, the guide field, all components on the analyzer bench and the PSD. Now, by iterating the strength of the guide field and the number and position of the permanent magnets the influence of an interfering magnetic field on the guide field could be observed.

In conclusion, the guide field was shown to work very well and up to expectations both in the magnetic interference tests as well as in all following uses, as no problems with external magnetic fields or unexplained loss of polarization were observed.

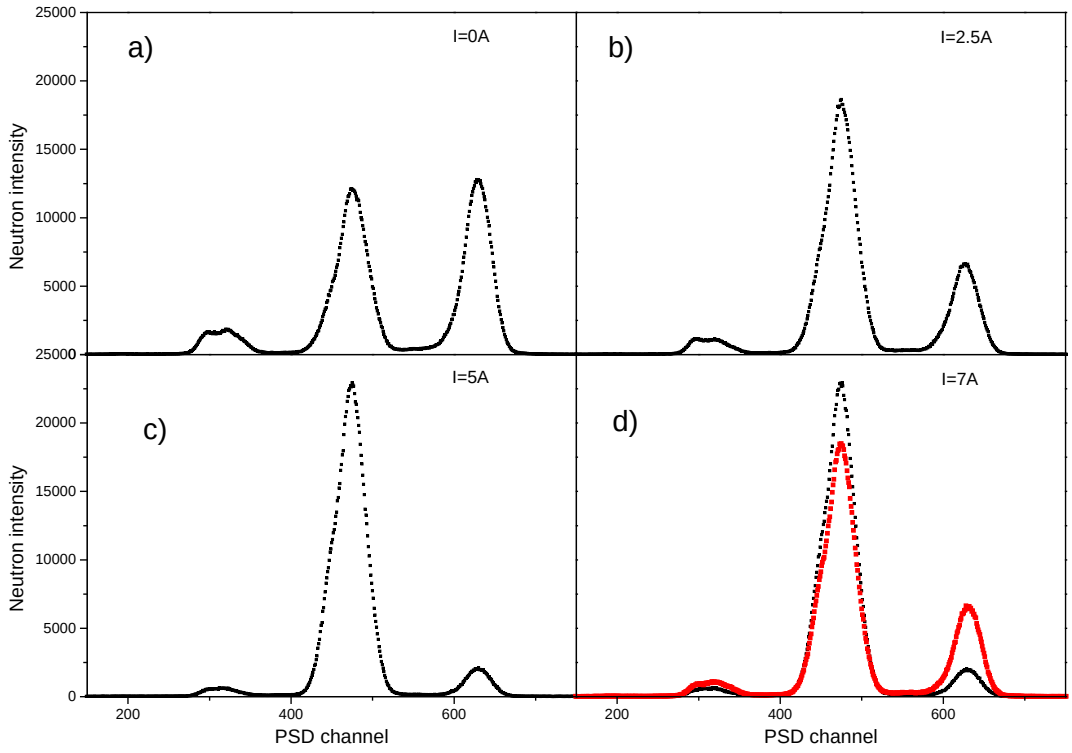

Fig. 27: Graphs show the beam profile of a polarized beam with a stray field of 1.3 mT at the sample position. Without guide field the profile shows a complete depolarization, shown in a). In b), with a guide field current of 2.5 A the beam is still slightly depolarized. In c) no depolarization can be seen for guide field currents of 5 A. The same is true in d) for a 7 A current (black dots). However polarization starts to break down for a stray field of 2.8 mT (red dots).

Some test beam profiles where taken utilizing the PSD and some permanent magnets as the source for a stray field. The magnets where placed at the sample position and provided stray fields of up to 2.8 mT. As shown in Fig. 27 our quasi-Helmholtz setup provides a good quality guide field. In a) we see a completely depolarized beam as the guide field is inactive. In b) the beam profile still shows some depolarization with guide field operating with a current of 2.5 A. Operating with a current of 5 A we no longer see any depolarization in c) and in d) we see that a stray field of 2.8 mT is necessary to partly depolarize our beam. So, even operating our guide field with I=5 A we still have no effect on our beam polarization with a stray field one order of magnitude larger than the remnant stray fields originating from the floor.

Tests with standard equipment and situations, such as movement of the big experimental hall crane, moving the sample table, using a cryostat at the sample positon, etc. also showed no noticeable effect on beam polarization.

Measuring with the *I*=7 A and no stray field setup we noticed a drop of 1.7% beam polarization over a time of 11 h 40 min. The data from this test also gave us a relaxation time for the ^{3}He-cell of T_R=100(22) h for this experimental conditions (see Fig. 13).

3.5 Graphite Filter

From the Bragg equation

$$n\lambda = 2d\sin(\Theta) \tag{20}$$

it follows that not only neutrons with a wavelength of λ are reflected by a monochromator but also wavelengths of $\frac{\lambda}{n}$. From these higher order neutrons we can get additional, spurious peaks in our data. This makes the correct interpretation of a given measurement more difficult up to impossible. To avoid this there are usually filter systems to eliminate these higher order neutrons from the beam before the detectors. In our case we are using a filter that works by Bragg scattering.

Right in front of our collimator we have a filter, made out of pyrolytic graphite (PG-filter). A PG filter is the best option for a thermal neutron instrument to filter higher order neutrons from the beam. The filter consists of a crystal with its highly aligned hexagonal c-axis and a randomly aligned a-axis. Placing the filter with its c-axis parallel to the beam makes it nearly transparent for neutrons of some given energies, while higher order neutrons are eliminated

For example, looking at how the neutron cross section of a PG filter block depends on the incident neutron energy we see a minimum for incident neutrons of 14.6 meV (λ=2.36 Å). Looking at second order neutrons $\left(\frac{\lambda}{2}\right)$ carrying 60 meV of energy we see a maxima in the cross-section, see [15]. This means that such a filter has a good transmission for 15 meV neutrons, while higher order neutrons are attenuated by scattering processes.

3.6 Mezei Flipper

During a polarized neutron experiment it might become interesting to change the spin direction of the beam. A device that changes the spin direction is commonly called a spin-flipper. PUMA has a pair of Mezei flippers available, one of which is shown in Fig. 28. In the following they will be identified as flipper no. 1 or 2.

They were used during the early stages of the implementation of the PUMA polarization analysis and were constructed by the chemical department workshop in Göttingen, as apparently no comparable components where commercially available. The flippers are constructed from anodized aluminum wire of 1.6mm diameter (commercially available for flower bindings…). This wire was chosen as aluminum is mostly transparent for neutrons and anodization is necessary to isolate the windings of the coil from each other. The coils have 98 windings and a depth (in beam direction) of 20 mm each.

The flippers consist of two coils, one to compensate for external magnetic fields, the compensation coil (C) and the main coil (M) to change the spin direction.

Fig. 28 shows a photo of flipper 2. Both coils can be seen, the main coil wirings in magenta completely and partially also the windings of the compensation coil in gold.

Fig. 28: Photo of flipper 2 shows the windings (differently colored wire for both coils) and power connections for both coils

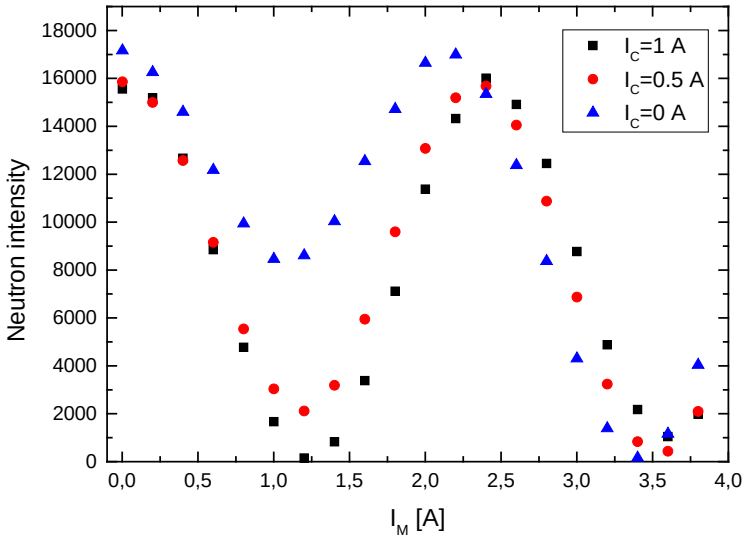

Fig. 29: Measurement of intensity depending on main coil current with for compensation currents of 0, 0.5 and 1A for flipper 2. The data points very close to zero are in the 150 counts range

The magnetic dipole moment of a neutron with spin **S** is given by

$$\boldsymbol{\mu}_S = g_n \mu_N \frac{\boldsymbol{S}}{\hbar} \tag{21}$$

where g_n=-3.826085 is the spin-g-factor of the neutron, and μ_N is the nuclear magneton given by

$$\mu_N = \frac{e\hbar}{2m_p} \tag{22}$$

Here m_p is the mass of a single, undisturbed, proton.

From this we get the gyromagnetic ratio of a particle with spin *S*

$$\gamma_S = \frac{|\boldsymbol{\mu}_S|}{|\boldsymbol{S}|} \tag{23}$$

Now combining and we get an expression for the Lamor frequency

$$f_{Lamor} = \frac{\gamma}{2\pi} B = \frac{|g_n \mu_N \frac{\boldsymbol{S}}{\hbar}|}{|\boldsymbol{S}|} \frac{B}{2\pi} \tag{24}$$

Knowing the length of our neutron flight path though the flipper field (20 mm) and the speed of our neutrons (k_i=k_f=2.662 Å^{-1}, λ=2.36 Å, v=1676 m/s) we can say that, and more importantly how, they will be influenced by B for the 11.9*10^{-6} seconds it takes them to cross the flipper.

To characterize our flippers we put one into the beam-path on the monochromator side of the polarization setup, after our polarizer cell. Then we measured the intensity of the central channel as

a function of the current of the main coil (I_M) and iterated the scan over different currents for the compensation coils (I_C). Each flipped neutron will now be deflected towards one of the side channels. For such a scan a measured intensity of zero means perfect flipping of all detected neutrons as there are no longer ones reaching the central channel. One such scan for flipper 2 is shown in Fig. 29. Here a nearly perfect flipping is shown by the intensity minimum for I_C=1 A and I_M=1.23 A.

From these measurements the best flipping ratio for flipper 1 was achieved with I_M=1.3 A and I_C=1 A. In addition to this a transmission of 92% was observed by measuring the beam intensity with and without the flipper in the beam path. During this transmission test where the flipper was in the beam path it was powered down so that only the effect of its materials was observed.

For Flipper 2 we observed the best result using I_M=1.23 A and I_C=1 A. Flipper 2 has a transmission of 97%. Consequently we used flipper 2 for all following tests.

Flipping ratios of the two flippers where 72.4 for flipper 1 and 104 for flipper 2. The limiting factor in determining the flipping ratio was mostly the high, but not perfect, polarization of the incident beam and the, also not perfect, reflectivity of our deflectors resulting in a slightly too high count-rate for the central channel. Beam polarization is a limiting factor for this flipping ratio test as it was done in the early phases of this project before we started to correct for beam polarization. The flipping ratio itself is independent of beam polarization

The deflectors were useful for determining the incident beam polarization and helped to discriminate between nuclear and magnetic signal during our first test measurement on hematite (see 5.4 “Hematite”).

We also did a longer series of measurements, alternating between on/off states of flipper 2. This scan is shown in Fig. 30.

The flipping ratio in this plot is calculated by $FR = \frac{I_{off}}{I_{on}}$, without any further data correction. This means that our real FR is somewhat higher because of the not deflected neutrons reaching the central detector while the flipper is on.

Because of this it primarily shows the aging of the He-cell, as the shown data is not corrected for polarization. So the plot shows polarization of the incident beam, over the course of the measurement, but also the extremely good flipping ratio of our Mezei-flipper can be seen at the beginning of the measurement where the highly polarized beam (P_n= 0.9996) makes a polarization correction unnecessary.

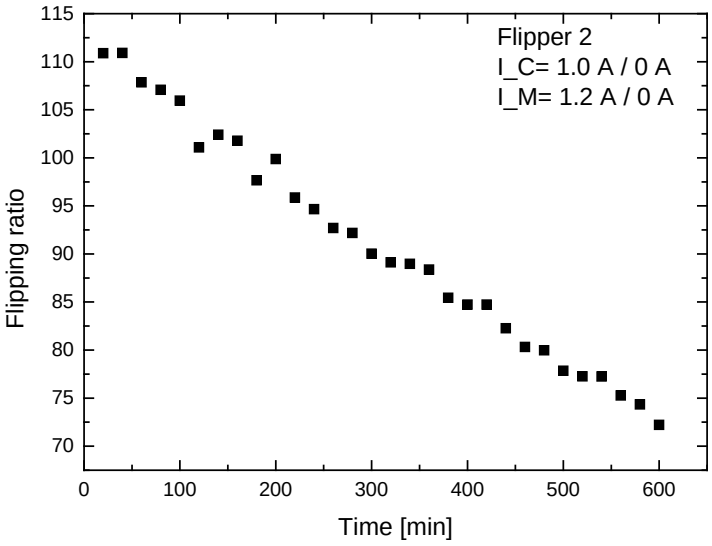

Fig. 30: Data for the measurement of the flipper 2 flipping ratio. As the data was not corrected for beam polarization the first measurement gives the best value for the flipping ratio, but is still a lower limit.

3.7 Calculating the polarization analysis Multianalyzer/-detector positions

The MAD used in the PUMA polarization analysis is a complex system with numerous degrees of freedom. Positioning all needed axis is a complex problem, but as the whole process of finding optimal positions for each analyzer, detector, and guide is a basic problem of geometry. The distances are given by the angles for the analyzers, by the neutron wavelength and the angles of the deflectors, and the position of the detectors and their guides by the angles of the analyzers. All of this can be calculated in advance and given as an output of commands for PUMA. A script to calculate the best positions is now available at PUMA and integrated into the PA setup software.
In this subsection we will go through all necessary steps to get an optimized configuration for the MA in polarization analysis mode. The theory of operation, calculation of the MAD positions, as well as some of our first measurements where already published by us in [16].
We start with the following given quantities;

D	=	Distance between analyzer rails [2cm (fixed)]
θ_A	=	Analyzer Bragg-angle [°]
L_{SA}	=	Distance sample-analyzer [cm]
L_{SD1}	=	Distance sample-deflector 1 [cm]
L_{SD2}	=	Distance sample-deflector 2 [cm]
L_{AD}	=	Distance analyzer-detector [cm]
γ_1	=	Deflector 1 tilt angle [°]
γ_2	=	Deflector 2 tilt angle [°]
α	=	MA tilt angle [°]

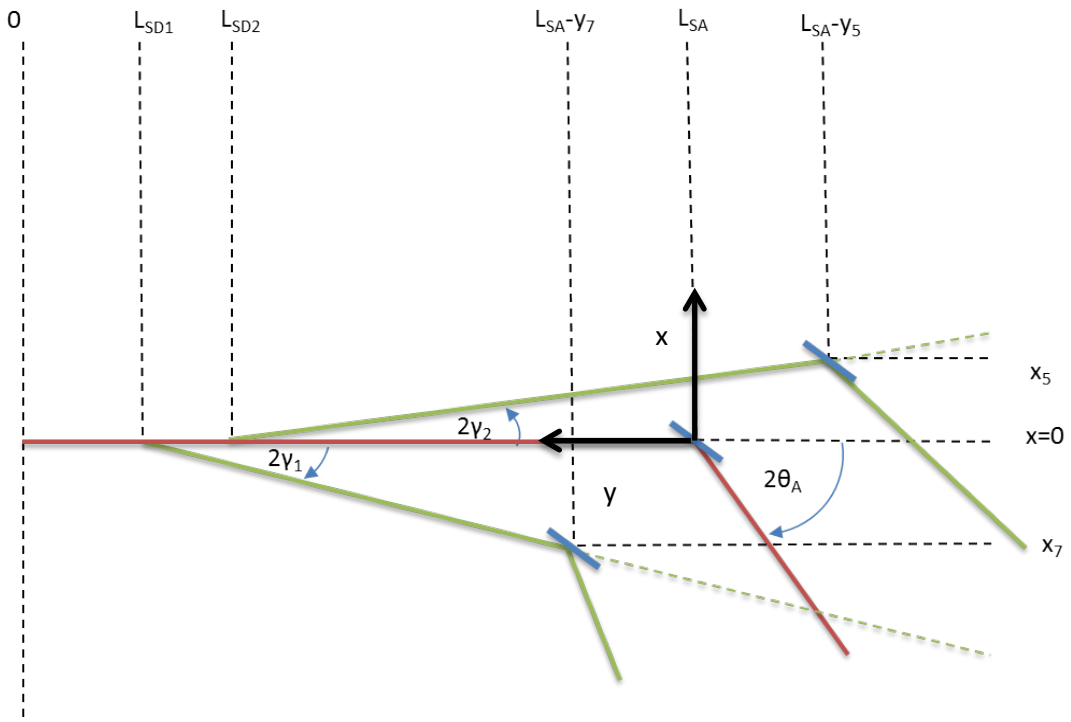

Fig. 31: Distances and angles relevant for the MA configuration calculation. The y-coordinate axis is perpendicular to x

In addition to the relevant distances and angles shown in Fig. 31 there is also the option to rotate the whole analyzer around its center. The angle for this rotation is α. The center of this coordinate system is the analyzer center.

We now have the position of the side analyzers (5 and 7, with 6 the central analyzer) given by

$$x_5 = (L_{SA} - L_{SD2} - y_5)\tan(2\gamma_2) \tag{25}$$

$$x_7 = (L_{SA} - L_{SD1} - y_7)\tan(2\gamma_1)$$

The relation between the x and y coordinates of the analyzer crystals is given by the MA tilt angle α and can be expressed by

$$x_5 = D - y_5 \tan(\alpha) \qquad (26)$$
$$x_7 = -D - y_7 \tan(\alpha)$$

If we combine these equations we can determine the y-coordinates of the analyzers using

$$y_5 = \frac{(L_{SA} - L_{SD2})\tan(2\gamma_2) - D}{\tan(2\gamma_2) - \tan(\alpha)}$$
$$y_7 = \frac{(L_{SA} - L_{SD1})\tan(2\gamma_1) + D}{\tan(2\gamma_1) - \tan(\alpha)} \qquad (27)$$

Now, using equation (27) we have both x- and y-coordinates for the analyzers. This would be enough if the whole MA was never rotated. Then x is parallel to the optical path of our central neutron beam.

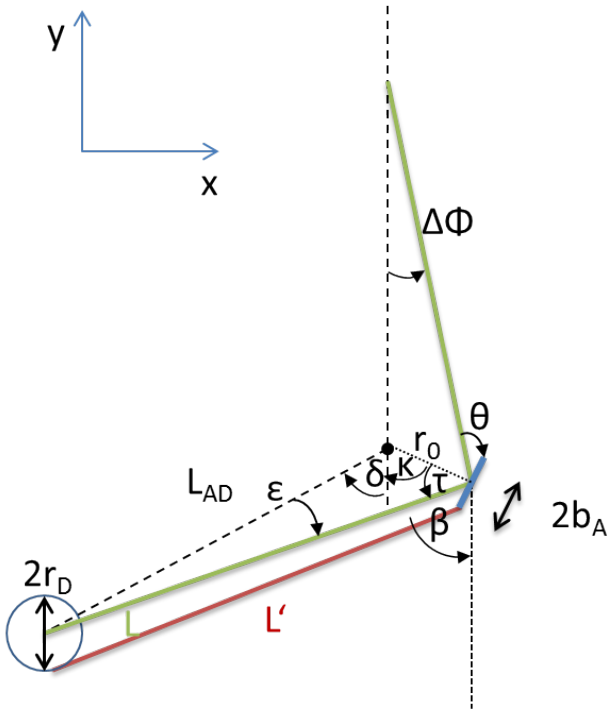

Fig. 32: Angles and distances relevant for the MD configuration calculation

But as the MA can rotate we have to take into account that the path traveled by analyzer 5 or 7 to reach their intended position is not given by y but rather by

$$\tilde{y}_5 = \frac{y_5}{\cos(\alpha)} + D \cdot tan(\alpha)$$
$$\tilde{y}_7 = \frac{y_7}{\cos(\alpha)} + D \cdot tan(\alpha) \qquad (28)$$

As the analyzer crystals cannot move in x-direction calculating $\tilde{x}_5$ and $\tilde{x}_7$ for a tilted MA is not necessary.

The angles for the analyzers are given by the neutron wavelength. For k_f=2.663 Å^{-1} the reflection angle for a graphite crystal is $\Theta_A = 20.6°$. From this we get -20.6° (minus sign to get a consistent sense of rotation) as the fixed angle for the central analyzer (normally number 6), and taking into account the angle of the scattered beams, defined by the deflector angles we get -20.6°+γ_2 for analyzer 5 and -20.6°-γ_1 for analyzer 7.With this we know how to position our three analyzers.

What we now still lack is the position of the detectors and their guides. For this we take a look at the coordinate system in Fig. 32.

L is the distance between the analyzer center and the center of the corresponding detector, while L' is the distance between the outer edges of both components. r_0 is the distance between the analyzer center and the individual analyzer blade, while b_A is half the width of the analyzer blade and r_D is the radius of a detector tube.

We now have the following general relations:

$$\kappa = \arctan\left(\frac{x_i}{y_i}\right) \tag{29}$$

Here x_i/y_i is the center of the relevant analyzer crystal.

$$\begin{gathered}
\tau = \pi + \kappa - \beta \\
\sin(\varepsilon) = -\frac{r_0}{L_{AD}}\sin(\tau) = -\frac{r_0}{L_{AD}}\sin(\beta - \kappa) \\
\delta = -\beta - \varepsilon \\
L = L_{AD}\frac{\sin(-\delta - \kappa)}{\sin(\beta - \kappa)} \\
L' = L - b_A\cos(\Theta)
\end{gathered} \tag{30}$$

As already mentioned, the angles (β>0, see Fig. 32) between the beam towards a detector and direct beam are given by

$$\begin{gathered}
\beta_5 = -2\Theta_A - 2\beta_2 \\
\beta_6 = -2\Theta_A \\
\beta_7 = -2\Theta_A - 2\beta_1
\end{gathered} \tag{31}$$

We also need to know where to position the guides of each used detector. For this we now use

$$\begin{gathered}
\kappa_5 = \arctan\left(\frac{x_5}{y_5}\right) \\
\kappa_7 = \arctan\left(\frac{x_7}{y_7}\right)
\end{gathered} \tag{32}$$

to obtain these expressions for the angles between L_{AD} and L

$$\sin(\varepsilon_5) = \pm\left|\frac{\sqrt{x_5^2 + y_5^2}}{L_{AD}}\sin(\beta_5 - \kappa_5)\right| \; for\; y_5 - x_5\cot(\beta_5) \gtrless 0 \tag{33}$$

$$\varepsilon_6 = 0 \tag{34}$$

$$\sin(\varepsilon_7) = \pm\left|\frac{\sqrt{x_7^2 + y_7^2}}{L_{AD}}\sin(\beta_7 - \kappa_7)\right| \; for\; y_7 - x_7\cot(\beta_7) \gtrless 0 \tag{35}$$

From this the angular positions of the used detectors are given by

$$\begin{aligned} \delta_5 &= -\beta_5 - \varepsilon_5 \\ \delta_6 &= -\beta_6 = -2\Theta_A \\ \delta_7 &= -\beta_7 - \varepsilon_7 \end{aligned} \tag{36}$$

As any given analyzer is not hit head on by the neutron beam we have to look at the projection of the tilted analyzer inside the beam divergence. To get the projection of the effective analyzer width a correction for the rotation angle is needed. The correction angles can be calculated using

$$\begin{aligned} \Delta\varepsilon_5 &= \left|\arctan\left(-\frac{b_A\, sin(\Theta - R_D)}{L_5{}'}\right)\right| \; with\; L_5' = L_{AD}\frac{\sin(-\delta_5 - \kappa_5)}{\sin(\beta_5 - \kappa_5)} - b_A\cos(\Theta) \\ \Delta\varepsilon_6 &= \left|\arctan\left(-\frac{b_A\, sin(\Theta - R_D)}{L_6{}'}\right)\right| \; with\; L_6' = L_{AD} - b_A\cos(\Theta) \\ \Delta\varepsilon_7 &= \left|\arctan\left(-\frac{b_A\, sin(\Theta - R_D)}{L_7{}'}\right)\right| \; with\; L_7' = L_{AD}\frac{\sin(-\delta_7 - \kappa_7)}{\sin(\beta_7 - \kappa_7)} - b_A\cos(\Theta) \end{aligned} \tag{37}$$

With this we have calculated the angle for the guide sheets of each detector, $\varepsilon_i+\Delta\varepsilon_i$. We now have the angle Θ_i for the analyzer blades, the position of the analyzers in x and y given by equations (26) and (27) as well as the angular position of the detectors and their guides given by equations (36) and (37) respectively.

For the case that the MA is not tilted, $\gamma = 0$ the equations for x and y look like

$$\begin{aligned} x_5 &= D \\ \tilde{y}_5 = y_5 &= L_{SA} - L_{SD2} - \frac{D}{\tan(2\gamma_2)} \\ x_7 &= -D \end{aligned} \tag{38}$$

$$\tilde{y}_7 = y_7 = L_{SA} - L_{SD1} - \frac{D}{\tan(2\gamma_1)}$$

This was the case for all measurements in this work. We now can calculate full set of coordinates and angles to position the MAD for any given PA setup.

There are some ideas where tilting the whole MA is an option, some of which are discussed in section 6.2.1.

4 Theory

After introducing our setup we will discuss what can be done with it and how to interpret the data. For this we will, in the following chapter, first look at some formalism for neutron scattering, first unpolarized nuclear and magnetic scattering followed by a section about polarized neutron scattering. Then an analytical model for simulating experiments with our setup is introduced and compared to a Monte Carlo simulation.

4.1 Theory of neutron scattering from nuclei

nuclear scattering function[5]

For discussing scattering processes it is advantageous to use the concept of reciprocal space. The position of an atom, or, for some systems, a unit of atoms in a lattice can be represented by the lattice vector ***R***, with the components ***a, b*** and ***c***. If this is the case for a lattice position in real space, we can also define a reciprocal lattice vector:

$$\boldsymbol{G}_{hkl} = h\boldsymbol{a}^* + k\boldsymbol{b}^* + l\boldsymbol{c}^* \tag{39}$$

This is a very useful representation for the description of scattering by Bragg reflections. Note that *h, k, l* are the Miller indices used to denote the orientation and plane distance in reciprocal space. Further

$$\boldsymbol{a}^* = \frac{2\pi(\boldsymbol{b} \times \boldsymbol{c})}{\boldsymbol{a} \cdot (\boldsymbol{b} \times \boldsymbol{c})} \tag{40}$$

represents one of the three independent basic vectors, with ***b**** and ***c****having cyclic permutated definitions. Now, for a given lattice, $\boldsymbol{G}_{hkl}$ is perpendicular to the atomic plane. With d the lattice spacing, as defined for a Bragg scattering experiment we can connect d with the reciprocal lattice vector by

[5] 4.1 and 4.2 are mostly following chapter 1 and 2 of the book “Neutron Scattering with a Triple-Axis Spectrometer” by Shirane, Shapiro and Tranquada, see [17]

$$|\boldsymbol{G}_{hkl}| = \frac{2\pi n}{d} \tag{41}$$

Here n is an integer multiple for the lattice spacing *d*.

While performing a scattering experiment there are two principal observable cases of scattering behavior; elastic and inelastic scattering. For elastic scattering we have $|\boldsymbol{k}_i|=|\boldsymbol{k}_f|=k$. $\boldsymbol{k}_i$ and $\boldsymbol{k}_f$ are the initial and final wave vectors as shown in Fig. 3. Further the scattering vector **Q** for elastic scattering is defined as:

$$\boldsymbol{Q} = \boldsymbol{G} = \boldsymbol{k}_i - \boldsymbol{k}_f \tag{42}$$

$\boldsymbol{k}_i$ is the direction of the incident beam, while $\boldsymbol{k}_f$ is the direction of the scattered beam, relative to the sampled crystal.

In the case of inelastic scattering things get somewhat more complicated. As energy is transferred form the incoming neutrons to the sample $|\boldsymbol{k}_i|=|\boldsymbol{k}_f|$ is no longer true, and we have

$$\boldsymbol{Q} = \boldsymbol{G} + \boldsymbol{q}_j \tag{43}$$

Here $\mathbf{q}_j$ is the propagation vector of an excitation mode j. Thus the scattering vector becomes the sum of the reciprocal lattice vector of a Bragg peak (**G**) and some excitation momentum ($\mathbf{q}_j$) transferring energy. This transfer is between the incoming, scattered neutron and the object on which it is scattered.

If we now take a look at the scattering process itself and how to describe it, we can start with the differential cross-section, as expressed by the sum of the incoherent and coherent parts:

$$\frac{d^2\sigma}{d\Omega dE} = \frac{d^2\sigma}{d\Omega dE}_{inc} + \frac{d^2\sigma}{d\Omega dE}_{coh} \tag{44}$$

Here σ is the scattering cross-section and dΩ is the angle under which the neutron beam is scattered. The incoherent part contains information about phenomena of individual particles such as particle movement inside the sample. For this work the coherent part, which provides information about collective effects such as Bragg scattering and inelastic scattering by magnons and phonons is much more interesting.

A scattered neutron induces a transition in the quantum states of a sample while maintaining the basic nature of these states. They can be described by λ_i and λ_f which are quantum numbers for the

initial and final state. Neutron and sample interact with each other via the interaction operator *V*. With this the differential cross section can be written as

$$\frac{d^2\sigma}{d\Omega_f dE_f} = \frac{k_f}{k_i}\left|\langle \boldsymbol{k}_f \lambda_f | V | \boldsymbol{k}_i \lambda_i \rangle\right|^2 \delta\left(\hbar\omega + E_i - E_f\right) \tag{45}$$

Equation (45) assumes specific initial and final states. In the more general case there will be a number of possible initial states weighted by $P(\lambda_i)$. $P(\lambda_i)$ is normalized by $\sum_{\lambda_i} P(\lambda_i) = 1$. Furthermore, there will also be a number of final states as long as there is no selection for a single state is taking place. This gives us the differential cross section in the form of

$$\frac{d^2\sigma}{d\Omega_f dE_f} = \frac{k_f}{k_i}\overline{\sum_{\lambda_\iota \lambda_f} P(\lambda_\iota)\left|\langle \boldsymbol{k}_f \lambda_f | V | \boldsymbol{k}_\iota \lambda_\iota \rangle\right|^2 \delta\left(\hbar\omega + E_\iota - E_f\right)} \tag{46}$$

The horizontal bar indicates all averaged quantities not included in $P(\lambda_i)$, such as isotopes, nuclear spin orientations etc.

Using the Born approximation and treating incident and scattered neutrons as plane waves the interaction matrix element can be written as

$$\left|\langle \boldsymbol{k}_f \lambda_f | V | \boldsymbol{k}_i \lambda_i \rangle\right|^2 = \langle \lambda_f \left| V(\boldsymbol{Q}) \sum_l e^{i\boldsymbol{Q}\boldsymbol{r}_l} \right| \lambda_i \rangle \tag{47}$$

$\mathbf{r}_l$ are the scattering center coordinates and $V(\boldsymbol{Q}) = \int d\boldsymbol{r}\, V(\boldsymbol{r}) e^{i\boldsymbol{Q}\boldsymbol{r}}$. For nuclear scattering the nuclear potential can be treated as a delta function with *b* the nuclear scattering length, so that

$$V(\boldsymbol{r}) = \frac{2\pi\hbar^2}{m_n} b \cdot \delta(\boldsymbol{r}) \tag{48}$$

Equation **(46)**, when averaging over initial states and summing over final states then reads like

$$\frac{d^2\sigma}{d\Omega_f dE_f} = \frac{k_f}{k_i}\overline{\sum_{\lambda_\iota \lambda_f} P(\lambda_\iota)\left|\langle \lambda_f \left| V(\boldsymbol{Q}) \sum_l e^{\iota \boldsymbol{Q}\cdot\boldsymbol{r}_l} \right| \lambda_\iota \rangle\right|^2 \delta(\hbar\omega + E_\iota - E_f)} \tag{49}$$

The differential cross section can also, as shown by Van Hove [18], be expressed as

$$\frac{d^2\sigma}{d\Omega dE} = N\frac{k_f}{k_i}|V(\boldsymbol{Q})|^2 S(\boldsymbol{Q},\omega) \tag{50}$$

however in newer literature it is more common to integrate *V(**Q**)* into *S(**Q**,ω)*, so that we get

$$\frac{d^2\sigma}{d\Omega dE} = N\frac{k_f}{k_i}S(\boldsymbol{Q},\omega) \tag{51}$$

We can now express the scattering function in the following form:

$$S(\boldsymbol{Q},\omega) = \frac{|V(\boldsymbol{Q})|^2}{2\pi\hbar N}\sum_{ll'}\int_{-\infty}^{\infty} dt\langle e^{-i\boldsymbol{Q}\cdot\boldsymbol{r}_{l'}(0)}e^{i\boldsymbol{Q}\cdot\boldsymbol{r}_{l}(t)}\rangle e^{-i\omega t} \tag{52}$$

N is the number of nuclei and *t* time. We use the thermal average, as shown by the angle brackets. Furthermore for inelastic scattering we can take a look at the general scattering function S(**Q**,ω) and eliminate all elastic contributions from it, for example Bragg scattering. What remains is a function of momentum and frequency that describes fluctuations in a given sample. Examples for such fluctuations are phonons for lattice excitations and magnons for magnetic excitations.
In a crystal lattice the orientation of magnetic moments undergoes permanent fluctuations. Because spins are coupled by exchange interactions these fluctuations produce collective excitations in the electrons spin structure. This collective phenomenon is known as a spin wave. A spin wave is also often called a magnon, a magnetic quasiparticle equivalent of vibrational quasiparticle, the phonon. Spin wave energy shows dispersion with respect to ***q*** in a given Brillouin zone. A neutron scattered from a magnetic system can absorb or emit magnons.
As this work is mostly concerned with magnetic excitation we will go into some more detail for magnetic scattering and magnons in the next sections.

4.2 Theory of neutron scattering from magnetic moments; magnetic scattering function

As they have a magnetic moment of their own neutrons can scatter from the magnetic moment of an atom, which makes them a good probe for the exploration of such phenomena.
One important aspect for magnetic scattering is the magnetic form factor f(**Q**).

$$f(\boldsymbol{Q}) = \int \rho_s(\boldsymbol{r})e^{i\boldsymbol{Q}\boldsymbol{r}}d\boldsymbol{r} \tag{53}$$

The magnetic form factor describes the Fourier transformation of the normalized unpaired spin density $\rho_s(r)$ of an atom.
The full differential cross section for magnetic scattering originates from equation (49) but also takes the initial (s_i) and final (s_f) spin-state of the neutron into account ([17] chapter 2.6, equation 2.61)

$$\frac{d^2\sigma}{d\Omega dE} = \frac{k_f}{k_i}\sum_{i,f} P(\lambda_i)\left|\langle\lambda_f\left|\sum_l e^{iQr_l}U_l^{s_i s_f}\right|\lambda_i\rangle\right|^2 \delta(\hbar\omega + E_i - E_f) \tag{54}$$

with

$$U_l^{s_i s_f} = \langle s_f | b_l - p_l \boldsymbol{S}_{\perp l}\boldsymbol{\sigma} + B_l \boldsymbol{I}_l \boldsymbol{\sigma} | s_i\rangle \tag{55}$$

Equation (55) is the atomic scattering amplitude for a site l where a spin state transitions from s_i to s_f. In addition *B* is the spin dependent nuclear amplitude, **I** is the nuclear spin operator and $\boldsymbol{S}_\perp$ is the magnetic interaction vector. $\boldsymbol{S}_\perp$can be described by

$$\boldsymbol{S}_\perp = \widehat{\boldsymbol{Q}} \times \left(\boldsymbol{S} \times \widehat{\boldsymbol{Q}}\right) = \boldsymbol{S} - \widehat{\boldsymbol{Q}}(\widehat{\boldsymbol{Q}} \cdot \boldsymbol{S}) \tag{56}$$

$\widehat{\boldsymbol{Q}}$ is a unit vector along $\boldsymbol{Q}$. Note that only the $\boldsymbol{S}$ component perpendicular to $\boldsymbol{Q}$ gives a contribution to the scattering amplitude. This has major experimental consequences as we can only measure the component of the magnetic interaction perpendicular to our scattering vector.

$$|\boldsymbol{S}_\perp|^2 = \sum_{\alpha,\beta}\left(\delta_{\alpha\beta} - \hat{Q}_\alpha \hat{Q}_\beta\right) S^*_\alpha S_\beta \tag{57}$$

The differential cross section for atomic magnetic scattering of a system with a single sort of magnetic atom for unpolarized neutrons can be written as

$$\frac{d^2\sigma}{d\Omega_f dE_f} = \frac{N}{\hbar}\frac{k_f}{k_i} p^2 e^{-2W} \sum_{\alpha,\beta}\left(\delta_{\alpha\beta} - \hat{Q}_\alpha \hat{Q}_\beta\right) S^{\alpha\beta}(\boldsymbol{Q}, \omega) \tag{58}$$

Where

$$p = \left(\frac{\gamma r_0}{2}\right) g f(Q) \tag{59}$$

$$\frac{\gamma r_0}{2} = \frac{\gamma e^2}{2 m_e c^2} = 0.2695 \cdot 10^{-12} cm \tag{60}$$

here *g* is the Lande splitting factor, *e* and m_e are the electron mass and charge and *c* the speed of light.

And furthermore

$$S^{\alpha\beta}(\boldsymbol{Q},\omega) = \frac{1}{2\pi}\int_{-\infty}^{\infty} dt\, e^{-i\omega t} \sum_{l} e^{iQ\cdot r_l} \langle S_0^{\alpha}(0) S_l^{\beta}(t)\rangle \tag{61}$$

Here we averaged over different possible configurations, as indicated by <…>. Now integrating $S^{\alpha\beta}(\mathbf{Q},\omega)$ over all frequencies and then integrating over a whole Brillouin zone in reciprocal space gives the following sum rule

$$\int_{-\infty}^{\infty} d\omega \int_{BZ} d\boldsymbol{Q} S^{\alpha\beta}(\boldsymbol{Q},\omega) = \frac{(2\pi)^3}{3v_0} S(S+1)\delta_{\alpha\beta} \tag{62}$$

Elastic Bragg scattering of a magnetically ordered system is proportional to $\langle S^z\rangle^2$, with z the axis along which the magnetic moments are ordered. For temperatures below the ordering transition and classical spins (S is large) we have $\langle S^z\rangle = S$.

The weight of scattering from magnons compared to magnetic Bragg scattering is *1/S* which goes to zero for large S. For temperatures above the ordering transition diffuse scattering is observed with a weight proportional to *S(S+1).*

Up until this point magnetization density, from which a neutron is scattered, was only the result of spin angular momentum. But there are also contributions from orbital angular momentum.

The scattering cross section includes the Fourier transform of the magnetization density, expressed by

$$\frac{\boldsymbol{M}(\boldsymbol{Q})}{\mu_B} = g\boldsymbol{S}f(\boldsymbol{Q}) \tag{63}$$

With g=2. Using a radial wave function Φ(r) that corresponds to the unpaired spin we get

$$f(Q) = \int_0^{\infty} dr\, r^2 j_0(Qr)|\Phi(r)|^2 \equiv \langle j_0\rangle \tag{64}$$

With $j_n(Qr)$ a spherical Bessel function of n-th order. Now we can include the orbital moment and write (63) as

$$\frac{\boldsymbol{M}(\boldsymbol{Q})}{\mu_B} = 2\langle j_0\rangle S + (\langle j_0\rangle + \langle j_2\rangle)\boldsymbol{L} \tag{65}$$

L is the angular momentum vector.

4.3 Theory of polarized neutron scattering

Neutrons have a magnetic moment of

$$\boldsymbol{\mu}_n = \gamma \mu_N \boldsymbol{\sigma}_n \tag{66}$$

with the gyromagnetic ratio γ=-1.91 and where

$$\mu_N = \frac{e\hbar}{2m_p} \tag{67}$$

is the nuclear magneton and $\boldsymbol{\sigma}_n$ stands for the neutron spin operator.

This magnetic moment allows neutrons to interact with magnetic phenomena, which in turn allows us to use neutrons as a probe for magnetic systems.

So, by using polarized neutrons it is possible to probe a sample for its magnetic structure and behavior in details not possible by conventional neutron experiments.

As a neutron is a spin $\frac{1}{2}$ particle with a magnetic momentum several observations can be made.

When observed along one axis, such as the z-axis as given by our guide field, the vector component of its total angular momentum can take two different possible values, $\pm\frac{\hbar}{2}$.

Like in most cases we only observe the polarization vector in the direction of the external magnetic field in our experiment. For us this is our guide field, described in section 3.4.

Before we use this restriction given by our setup we will first find expressions describing in general terms how the neutron spin can interact. For this we start with the energy of a neutron interacting with a magnetic field, which is given by

$$V = -\boldsymbol{\mu}_n \boldsymbol{B} \tag{68}$$

The magnetic field of a moving electron is given by

$$\boldsymbol{B}(\boldsymbol{r}) = \frac{\mu_0}{4\pi} \nabla \times \frac{\boldsymbol{\mu}_e \times \boldsymbol{r}}{|\boldsymbol{r}|^3} - \frac{e}{4\pi\varepsilon_0} \boldsymbol{v} \times \frac{\boldsymbol{r}}{|\boldsymbol{r}|^3} \tag{69}$$

with the coordinate-system centered on the electron.

Combining equations (68) and (69) we calculate the field of the magnetic moment between a neutron and a moving electron using a neutron with spin σ, located at $\boldsymbol{r}$. We get an interaction potential described by

$$V(r) = -\boldsymbol{\mu}_N \boldsymbol{B} = -\gamma\mu_N \boldsymbol{\sigma}\boldsymbol{B} = -\gamma\mu_N \boldsymbol{\sigma}\left[\frac{\mu_0}{4\pi}\nabla \times \frac{\boldsymbol{\mu}_e \times \boldsymbol{r}}{|\boldsymbol{r}|^3} - \frac{e}{4\pi\varepsilon_0}\boldsymbol{v} \times \frac{\boldsymbol{r}}{|\boldsymbol{r}|^3}\right] \\ = \gamma\mu_N \left[2\mu_B \boldsymbol{\sigma}\nabla \times \frac{\boldsymbol{s} \times \boldsymbol{r}}{r^3} - \frac{e}{8\pi\varepsilon_0 m_e}\left(\boldsymbol{p}_e \frac{\boldsymbol{\sigma} \times \boldsymbol{r}}{\boldsymbol{r}^3} + \frac{\boldsymbol{\sigma} \times \boldsymbol{r}}{\boldsymbol{r}^3}\boldsymbol{p}_e\right)\right] \tag{70}$$

Here μ_N is the nuclear magneton, γ the gyromagnetic ratio, μ_0 permeability of free space, μ_e the magnetic moment of the electron, **v** its speed**, s** the electron spin and $\mathbf{p}_e$ its momentum.
Now we write down the transition matrix element which takes the following form

$$\left|\langle \boldsymbol{k}_f \boldsymbol{\sigma}_f \lambda_f | V(\boldsymbol{r}) | \boldsymbol{k}_i \boldsymbol{\sigma}_i \lambda_i \rangle\right|^2 \\ = (\gamma\mu_N)^2 \left|\left[\langle \boldsymbol{\sigma}_f \lambda_f \left| \int e^{i(\boldsymbol{k}_i - \boldsymbol{k}_f)\boldsymbol{r}} \boldsymbol{\sigma}\nabla \times \frac{\boldsymbol{s} \times \boldsymbol{r}}{r^3} d\boldsymbol{r} \right| \boldsymbol{\sigma}_i \lambda_i \rangle \right. \\ - \frac{e}{8\pi\varepsilon_0 m_e} \langle \boldsymbol{\sigma}_f \lambda_f \left| \int e^{i(\boldsymbol{k}_i - \boldsymbol{k}_f)\boldsymbol{r}} \left(\boldsymbol{p}_e \frac{\boldsymbol{\sigma} \times \boldsymbol{r}}{r^3} \right.\right. \\ \left.\left. + \frac{\boldsymbol{\sigma} \times \boldsymbol{r}}{r^3}\boldsymbol{p}_e\right) d\boldsymbol{r} \right| \boldsymbol{\sigma}_i \lambda_i \rangle \Big] d\boldsymbol{r} \Big|^2 \delta(\hbar\omega + E_{\lambda_i} - E_{\lambda_f}) \tag{71}$$

$\boldsymbol{k}_{i/f}$ is the wave vector, $\boldsymbol{\sigma}_{i/f}$ the spin state, $\lambda_{i/f}$ the wavelength and *E* the wavelength dependent energy of the initial/i or final/f neutron. Now, using

$$\nabla \times \frac{\boldsymbol{s}_e \times \boldsymbol{r}}{r^3} = \frac{1}{2\pi^2} \int \frac{1}{q^2} \boldsymbol{q} \times (\boldsymbol{s}_e \times \boldsymbol{q}) e^{i\boldsymbol{q}\boldsymbol{r}} d\boldsymbol{q} \tag{72}$$

on the first part of equation (71) we get

$$
\begin{aligned}
&\int e^{i(\boldsymbol{k}_i-\boldsymbol{k}_f)\boldsymbol{r}}\boldsymbol{\sigma}\nabla\times\frac{\boldsymbol{s}\times\boldsymbol{r}}{r^3} \\
&=\frac{1}{2\pi^2}\iint\frac{1}{q^2}e^{i(\boldsymbol{k}_i-\boldsymbol{k}_f)\boldsymbol{r}}\boldsymbol{\sigma}(\boldsymbol{q}\times\boldsymbol{s}\times\boldsymbol{q})e^{i\boldsymbol{q}\boldsymbol{r}}d\boldsymbol{q}d\boldsymbol{r} \\
&=\frac{1}{2\pi^2}\int\frac{1}{q^2}\boldsymbol{\sigma}(\boldsymbol{q}\times\boldsymbol{s}\times\boldsymbol{q})\int e^{i(\boldsymbol{k}_i-\boldsymbol{k}_f)\boldsymbol{r}}d\boldsymbol{q}d\boldsymbol{r} \\
&=\frac{4\pi}{Q^2}\boldsymbol{\sigma}(\boldsymbol{Q}\times\boldsymbol{s}\times\boldsymbol{Q}) \\
&=4\pi\boldsymbol{\sigma}\left(\boldsymbol{s}-\widehat{\boldsymbol{Q}}\left(\widehat{\boldsymbol{Q}}\boldsymbol{s}\right)\right) \\
&=4\pi\boldsymbol{\sigma}\boldsymbol{s}^{\perp}
\end{aligned}
\tag{73}
$$

Where $\int e^{i(\boldsymbol{k}_i-\boldsymbol{k}_f)\boldsymbol{r}}d\boldsymbol{q}=(2\pi)^3\delta(\boldsymbol{Q}+\boldsymbol{q})$, $\boldsymbol{Q}=\boldsymbol{k}_i-\boldsymbol{k}_f$ and $\widehat{\boldsymbol{Q}}=\frac{\boldsymbol{Q}}{Q}$. $\widehat{\boldsymbol{Q}}\left(\widehat{\boldsymbol{Q}}\boldsymbol{s}\right)$ is the component of $\boldsymbol{s}$ in $\boldsymbol{Q}$ direction and $\left(\boldsymbol{s}-\widehat{\boldsymbol{Q}}\left(\widehat{\boldsymbol{Q}}\boldsymbol{s}\right)\right)$ the **s** component perpendicular to $\boldsymbol{Q}$. Only the spin components perpendicular to $\boldsymbol{Q}$ contribute to the scattering amplitude.

For the second part of equation (71) we first get:

$$
\begin{aligned}
&\int e^{i(\boldsymbol{k}_i-\boldsymbol{k}_f)\boldsymbol{r}}\boldsymbol{p}_e\frac{\boldsymbol{\sigma}\times\boldsymbol{r}}{r^3}d\boldsymbol{r} \\
&=\int e^{i\boldsymbol{Q}\boldsymbol{r}}\boldsymbol{p}_e\frac{\boldsymbol{\sigma}\times\boldsymbol{r}}{r^3}d\boldsymbol{r} \\
&=\int e^{i\boldsymbol{Q}\boldsymbol{r}}\boldsymbol{r}\frac{\boldsymbol{\sigma}\times\boldsymbol{p}_e}{r^3}d\boldsymbol{r} \\
&=-\int e^{i\boldsymbol{Q}\boldsymbol{r}}\boldsymbol{\sigma}\left(\nabla\left(\frac{1}{r}\right)\times\boldsymbol{p}_e\right)d\boldsymbol{r} \\
&=-\frac{1}{2\pi^2}\int e^{i\boldsymbol{Q}\boldsymbol{r}}\boldsymbol{\sigma}\left(\nabla\left(\int\frac{1}{q^2}e^{i\boldsymbol{q}\boldsymbol{r}}d\boldsymbol{q}\right)\times\boldsymbol{p}_e\right)d\boldsymbol{r} \\
&=-\frac{1}{2\pi^2}\int e^{i\boldsymbol{Q}\boldsymbol{r}}\boldsymbol{\sigma}\left(\left(\int\frac{i\boldsymbol{q}}{q^2}e^{i\boldsymbol{q}\boldsymbol{r}}d\boldsymbol{q}\right)\times\boldsymbol{p}_e\right)d\boldsymbol{r} \\
&=4\pi i\boldsymbol{\sigma}\frac{\boldsymbol{Q}\times\boldsymbol{p}_e}{Q^2} \\
&=i\frac{4\pi}{Q}\boldsymbol{\sigma}(\widehat{\boldsymbol{Q}}\times\boldsymbol{p}_e)
\end{aligned}
\tag{74}
$$

And then in the same way

$$
\begin{aligned}
&\int e^{i(\boldsymbol{k}_i-\boldsymbol{k}_f)\boldsymbol{r}}\frac{\boldsymbol{\sigma}\times\boldsymbol{r}}{r^3}\boldsymbol{p}_e d\boldsymbol{r} \\
&=i\frac{4\pi}{Q}\boldsymbol{\sigma}(\widehat{\boldsymbol{Q}}\times\boldsymbol{p}_e)
\end{aligned}
\tag{75}
$$

For the neutron scattering matrix element this means that we can write it down like

$$\begin{aligned}\left|\langle \boldsymbol{k}_f \boldsymbol{\sigma}_f \lambda_f | V(\boldsymbol{r}) | \boldsymbol{k}_i \boldsymbol{\sigma}_i \lambda_i \rangle\right|^2 \\ = (\gamma \mu_K)^2 \delta\left(\hbar\omega + E_{\lambda_i} - E_{\lambda_f}\right) \\ \cdot \left|\left(4\pi \langle \boldsymbol{\sigma}_f \lambda_f | \boldsymbol{\sigma} \boldsymbol{s}^{\perp} | \boldsymbol{\sigma}_i \lambda_i \rangle - i \frac{e}{\varepsilon_0 m_e} \langle \boldsymbol{\sigma}_f \lambda_f \left| \frac{1}{Q} \boldsymbol{\sigma} (\widehat{\boldsymbol{Q}} \times \boldsymbol{p}_e) \right| \boldsymbol{\sigma}_i \lambda_i \rangle\right) d\boldsymbol{r}\right|^2\end{aligned} \tag{76}$$

for a single spin state and like

$$\begin{aligned}\left|\langle \boldsymbol{k}_f \boldsymbol{\sigma}_f \lambda_f | V(\boldsymbol{r}) | \boldsymbol{k}_i \boldsymbol{\sigma}_i \lambda_i \rangle\right|^2 \\ = (\gamma \mu_K)^2 \delta\left(\hbar\omega + E_{\lambda_i} - E_{\lambda_f}\right) \\ \cdot \left|\left(4\pi \left\langle \boldsymbol{\sigma}_f \lambda_f \left| \sum e^{i\boldsymbol{Q}\boldsymbol{R}_k} \boldsymbol{\sigma} \boldsymbol{s}_k^{\perp} \right| \boldsymbol{\sigma}_i \lambda_i \right\rangle \right.\right. \\ \left.\left. - i \frac{e}{\varepsilon_0 m_e} \langle \boldsymbol{\sigma}_f \lambda_f \left| \frac{1}{Q} \sum e^{i\boldsymbol{Q}\boldsymbol{R}_k} \boldsymbol{\sigma} (\widehat{\boldsymbol{Q}} \times \boldsymbol{p}_k) \right| \boldsymbol{\sigma}_i \lambda_i \rangle\right) d\boldsymbol{r}\right|^2\end{aligned} \tag{77}$$

for multiple spins. Again $\boldsymbol{Q}$ is the scattering vector, $\boldsymbol{\sigma}$ the Pauli spin operator, $\boldsymbol{k}_{i/f}$, $\boldsymbol{\sigma}_{i/f}$, $\lambda_{i/f}$, and $E_{i/f}$ are the wave vector, spin state, wavelength and energy of the incident respective scattered neutron. Position of the kth electron is given by $\boldsymbol{R}_k$ and $\boldsymbol{s}_k^{\perp}$ is the spin component orthogonal to the scattering vector and $\boldsymbol{\sigma}$ is the Pauli spin operator.

We will now use the Pauli matrices which together form $\boldsymbol{\sigma}$ and have the following form:

$$\sigma_x = \begin{pmatrix} 0 & 1 \\ 1 & 0 \end{pmatrix} \quad \sigma_y = \begin{pmatrix} 0 & -i \\ i & 0 \end{pmatrix} \quad \sigma_z = \begin{pmatrix} 1 & 0 \\ 0 & -1 \end{pmatrix} \tag{78}$$

We can also write part of (77) concerning the orthogonal spin component as

$$\langle \boldsymbol{\sigma}_f \lambda_f \left| \frac{1}{Q} \sum e^{i\boldsymbol{Q}\boldsymbol{R}_k} \boldsymbol{\sigma} \boldsymbol{s}_k^{\perp} \right| \boldsymbol{\sigma}_i \lambda_i \rangle = \langle \boldsymbol{\sigma}_f \lambda_f | \widehat{\boldsymbol{\sigma}}_x m_x + \widehat{\boldsymbol{\sigma}}_y m_y + \widehat{\boldsymbol{\sigma}}_z m_z | \boldsymbol{\sigma}_i \lambda_i \rangle \tag{79}$$

again with $\boldsymbol{\sigma}_{i/f}$ the initial and final neutron spin state, $\lambda_{i/f}$ the neutron wavelength and $\boldsymbol{\sigma}$ the Pauli spin operator (equation (78)). $\boldsymbol{R}_k$ is the position of electron k, $\boldsymbol{s}_k^{\perp}$ is the spin component orthogonal with respect to $\boldsymbol{Q}$ and m_x, m_y and m_z are the components of the Fourier-transformed spins.

Eigenvectors and Eigenvalues of the Pauli matrices are as follows:

$$\begin{gathered}\sigma_x \begin{pmatrix} 1 \\ 1 \end{pmatrix} = \begin{pmatrix} 1 \\ 1 \end{pmatrix} \quad \sigma_x \begin{pmatrix} 1 \\ -1 \end{pmatrix} = \begin{pmatrix} -1 \\ 1 \end{pmatrix} = -1 \begin{pmatrix} 1 \\ -1 \end{pmatrix} \\ \boldsymbol{s}_{\pm}^{x} = \frac{1}{\sqrt{2}} \begin{pmatrix} 1 \\ \pm 1 \end{pmatrix}\end{gathered} \tag{80}$$

$$\begin{gathered}\sigma_y \begin{pmatrix} 1 \\ i \end{pmatrix} = \begin{pmatrix} 1 \\ i \end{pmatrix} \quad \sigma_y \begin{pmatrix} 1 \\ -i \end{pmatrix} = \begin{pmatrix} -1 \\ i \end{pmatrix} = -1 \begin{pmatrix} 1 \\ -i \end{pmatrix} \\ \boldsymbol{s}_{\pm}^{y} = \frac{1}{\sqrt{2}} \begin{pmatrix} 1 \\ \pm i \end{pmatrix}\end{gathered} \tag{81}$$

$$\sigma_z \begin{pmatrix}1\\0\end{pmatrix} = \begin{pmatrix}1\\0\end{pmatrix} \quad \sigma_z \begin{pmatrix}0\\1\end{pmatrix} = \begin{pmatrix}0\\-1\end{pmatrix} = -1\begin{pmatrix}0\\1\end{pmatrix} \qquad (82)$$
$$\boldsymbol{s}_+^z = \begin{pmatrix}1\\0\end{pmatrix} \text{ and } \boldsymbol{s}_-^z = \begin{pmatrix}0\\1\end{pmatrix}$$

A scattered neutron, as well as one before the scattering event, can be in one of these six spin states given by the Eigenvalues. Combining the six possible incident values with the six possible scattered values gives us a total of 36 combinations. For example a neutron with a spin oriented along the z axis that undergoes a spin-flip form z^+ to z^- can be described with the following expression:

$$\begin{aligned}\langle\sigma_z^+|\hat{\sigma}_x m_x + \hat{\sigma}_y m_y + \hat{\sigma}_z m_z|\sigma_z^-\rangle &= \langle\sigma_z^+|\hat{\sigma}_x m_x|\sigma_z^-\rangle + \langle\sigma_z^+|\hat{\sigma}_y m_y|\sigma_z^-\rangle + \langle\sigma_z^+|\hat{\sigma}_z m_z|\sigma_z^-\rangle \\ &= \begin{pmatrix}1\\0\end{pmatrix}\begin{pmatrix}0 & 1\\1 & 0\end{pmatrix}\begin{pmatrix}0\\1\end{pmatrix} m_x + \begin{pmatrix}1\\0\end{pmatrix}\begin{pmatrix}0 & -i\\i & 0\end{pmatrix}\begin{pmatrix}0\\1\end{pmatrix} m_y + \begin{pmatrix}1\\0\end{pmatrix}\begin{pmatrix}1 & 0\\0 & -1\end{pmatrix}\begin{pmatrix}0\\1\end{pmatrix} m_z \\ &= m_x - i m_y\end{aligned} \qquad (83)$$

Doing this for all possible combinations shows that there are only six, different contributions to the scattering function:

0:	(xx),($\overline{\text{xx}}$)
A=$\lvert m_y\rvert^2$:	(yy),($\overline{\text{yy}}$),(z$\bar{\text{z}}$),($\bar{\text{z}}$z)
B=$\lvert m_z\rvert^2$:	(y$\bar{\text{y}}$),($\bar{\text{y}}$y),(zz),($\bar{\text{z}}\bar{\text{z}}$)
C=1/2($\lvert m_y\rvert^2$+$\lvert m_z\rvert^2$+$m_y m_z$*+m_y*m_z):	(yz),($\overline{\text{yz}}$),(zy),($\overline{\text{zy}}$)
D=1/2($\lvert m_y\rvert^2$+$\lvert m_z\rvert^2$-$m_y m_z$*-m_y*m_z):	(y$\bar{\text{z}}$),($\bar{\text{y}}$z),(z$\bar{\text{y}}$),($\bar{\text{z}}$y)
E=1/2($\lvert m_y\rvert^2$+$\lvert m_z\rvert^2$+i($m_y m_z$*-m_y*m_z)):	($\bar{\text{x}}$x),($\overline{\text{xy}}$),($\bar{\text{x}}$y),(x$\bar{\text{z}}$),($\bar{\text{x}}$z),($\bar{\text{y}}$x),(yx),(zx),($\bar{\text{z}}$x)
F=1/2($\lvert m_y\rvert^2$+$\lvert m_z\rvert^2$-i($m_y m_z$*-m_y*m_z)):	(x$\bar{\text{x}}$),(xy),(x$\bar{\text{y}}$),(xz),(x$\bar{\text{z}}$),(y$\bar{\text{x}}$),($\overline{\text{yx}}$),(z$\bar{\text{x}}$),($\bar{\text{z}}$x)

Here (xx) means that the initial spin is oriented in positive x-direction and keeps its orientation during the scattering process. On the other hand (y$\bar{\text{z}}$) means an incident spin oriented in positive y-direction gets flipped in minus z-direction during scattering. All 36 possible combinations can be found in the appendix 8.2 “All magnetic scattering combinations”.

The chosen coordinate system has *x* parallel to ***Q***, and *y* perpendicular to ***Q***, so that the *x*-*y* plane is the scattering plane. Perpendicular to the scattering plane is *z*. From this orientation $\hat{\boldsymbol{\sigma}} m_x = 0$ follows, as only components perpendicular to ***Q*** make a contribution to the scattered intensity. Intensity of

the scattered beam is proportional to the structure factor squared. This means for our SF-example (equation (83)) the resulting intensity I_{SF} is proportional to $\left|m_y\right|^2$.
Utilizing these contributions to construct a general tensor for the intensities for a 3d polarization experiment we find the following contributions listed in Table 3.

	x	$\bar{x}$	y	$\bar{y}$	z	$\bar{z}$
x	0	2F	F	F	F	F
$\bar{x}$	2E	0	E	E	E	E
y	E	F	A	B	C	D
$\bar{y}$	E	F	B	A	D	C
z	E	F	C	D	B	A
$\bar{z}$	E	F	D	C	A	B

Table 3: Contributions to scattered intensity depending on the polarization of incident (columns) and scattered (rows) neutrons

As an example of how the general tensor behaves under certain conditions we will use a helical magnetic structure. For a chiral magnetic system this tensor can be further simplified. There are two cases, in the first one where m_z=im_y the six contributions are further simplified and we get the following elements:

$$A = B = \left|m_y\right|^2 = |m_x|^2$$

$$C = \frac{1}{2}(A + A - iA + iA) = A$$

$$D = \frac{1}{2}(A + A + iA - iA) = A$$

$$E = \frac{1}{2}(A + A + i(-iA - iA)) = 2A$$

$$F = \frac{1}{2}(A + A - i(-iA - iA)) = 0$$

This results in the intensity tensor shown in Table 4.

	x	$\bar{x}$	y	$\bar{y}$	z	$\bar{z}$
x	0	0	0	0	0	0
$\bar{x}$	4A	0	2A	2A	2A	2A
y	2A	0	A	A	A	A
$\bar{y}$	2A	0	A	A	A	A
z	2A	0	A	A	A	A
$\bar{z}$	2A	0	A	A	A	A

Table 4: Contributions for a m_z=im_y chiral system to scattered intensity depending on the polarization of incident (columns) and scattered (rows) neutrons

This means that there is no magnetic scattering if the polarization of the incident neutron beam is parallel to x and for scattered neutrons with polarization parallel to –x.

The second case is a chiral system where m_z=-im_y giving us the following contributions:

$$A = B = \left|m_y\right|^2 = |m_x|^2$$

$$C = \frac{1}{2}(A + A + iA - iA) = A$$

$$D = \frac{1}{2}(A + A - iA + iA) = A$$

$$E = \frac{1}{2}(A + A + i(iA + iA)) = 0$$

$$F = \frac{1}{2}(A + A - i(iA + iA)) = 2A$$

These contributions result in the tensor shown in Table 5.

	x	$\bar{x}$	y	$\bar{y}$	z	$\bar{z}$
x	0	4A	2A	2A	2A	2A
$\bar{x}$	0	0	0	0	0	0
y	0	2A	A	A	A	A
$\bar{y}$	0	2A	A	A	A	A
z	0	2A	A	A	A	A
$\bar{z}$	0	2A	A	A	A	A

Table 5: Contributions for a m_z=-im_y chiral system to scattered intensity depending on the polarization of incident (columns) and scattered (rows) neutrons

This means that there is no magnetic scattering if the polarization of the incident neutron beam is parallel to –x and for scattered beam with polarization parallel to x

4.3.1 Analytical calculations for PUMA polarization analysis

As we have a new setup we did some simulations for our unique beam profile to better understand the interaction between the different components, optimize components (see Fig. 20 for the collimator as an example), and to build a solid understanding of its principles. For this McStas[6], a tool for simulating neutron scattering experiments by a Monte Carlo approach was used. To supplement this we also did analytical calculations to confirm McStas findings and to better understand and control our experiment.

The analytical solution showed to be much faster and was used to optimize the setup and later to improve our experimental data. For this approach the geometrical structures of the polarization setup were critical as even small deviations in some constraints can lead to rather large differences in calculated results.

To get a successful quantitative interpretation of experimental data the characteristics of all components in the beam path and their influence on the neutron beam have to be taken into account.

In this section the analytical approach necessary to calculate the expected count rates for a given setup of the three analyzer channels is demonstrated. Even more important than the bare count rates, the rates of the different spin states and their flipping behavior are calculated.

[6] McStas can be found under http://www.mcstas.org/

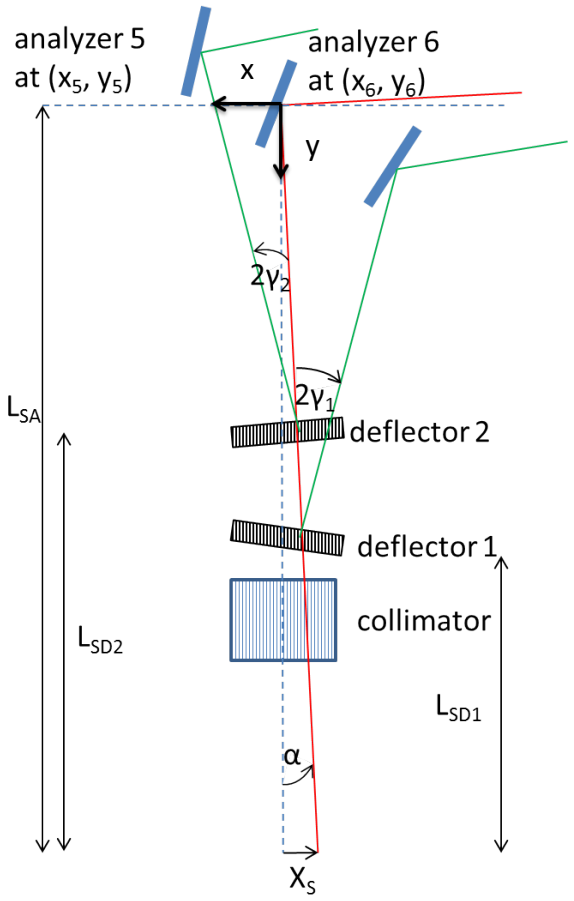

Fig. 33: Notation of the geometrical parameters used for the analytical description of the polarization analysis

The used geometric parameters are illustrated in Fig. 33.

The probability for a neutron to have spin up (↑) or spin down (↓) laterally displaced from the optical axis (x_S) after interacting with the sample is given by

$$W_S^{\uparrow\downarrow}(x_S) = \begin{cases} S^{\uparrow\downarrow} \text{ for } -\frac{B_S}{2} < x_S < \frac{B_S}{2} \\ 0 \text{ else} \end{cases} \quad (84)$$

where B_S is the sample width, or the width of the slit if no sample is present. This makes $S^{\uparrow\downarrow}$the scattered neutron flux. When the neutron leaves the sample with an angular divergence α respective to the optical axis the transmission probability for the collimator is given by

$$W_c(\alpha) = \exp\left(-4\ln 2\left(\frac{\alpha}{\alpha_c}\right)^2\right) \quad (85)$$

with α_C denoting the collimator divergence. After the collimator the transmitted neutrons hit the first of two deflectors. The first deflector is tilted by γ_1 (<0°) meaning the neutron hits under an angle of γ_1-α. The probability of reflection at the first deflector is given by

$$R_1^{\uparrow\downarrow}(\alpha, \gamma_1) = R_0^{\uparrow\downarrow}(\gamma_1 - \alpha) - D_1^{\uparrow\downarrow}(\alpha, \gamma_1) \quad (86)$$

The reflectivity for spin up/down, (↑/↓) neutrons under grazing angle of γ is given by $R_0^{\uparrow\downarrow}(\gamma)$, $D_1^{\uparrow\downarrow}(\alpha, \gamma_1)$ is the probability of double reflection between two wafer-coatings within the deflector which returns the neutron to its original direction. Double reflection occurs when a neutron hits a mirror coating, gets reflected and then hits another mirror before exiting the deflector. The effect of this is a reflection back into the original direction, resulting in a small lateral translation of the beam path.

To get the reflectivity-characteristic of our deflectors a reflectivity curve provided by the manufacturer (Swiss Neutronics) was fitted. As a result of this fit reflectivity for our deflectors was modelled as

$$R_0^{\uparrow} = 2.04772 - \left(0.05616 * \frac{1}{\tanh(\gamma)} * (-0.91817) + 1\right) + \frac{1}{\tanh(-\gamma * (-33.32664))} \quad (87)$$

for spin-up and

$$R_0^{\downarrow} = -0.00408 + \left(\frac{0.00252}{0.002 * \sqrt{\frac{\pi}{2}}}\right) * \exp\left(-2 * \left(\frac{\gamma - 0.0015}{0.002}\right)^2\right) \quad (88)$$

for spin-down reflectivity. In both cases using

$$C1 = \frac{4 * \log 2}{coll^2} \quad (89)$$

where *coll* is the collimation of the deflector. The deflectors work also as collimators with a collimation of 47.25' as a result of their construction, see chapter 3.2.

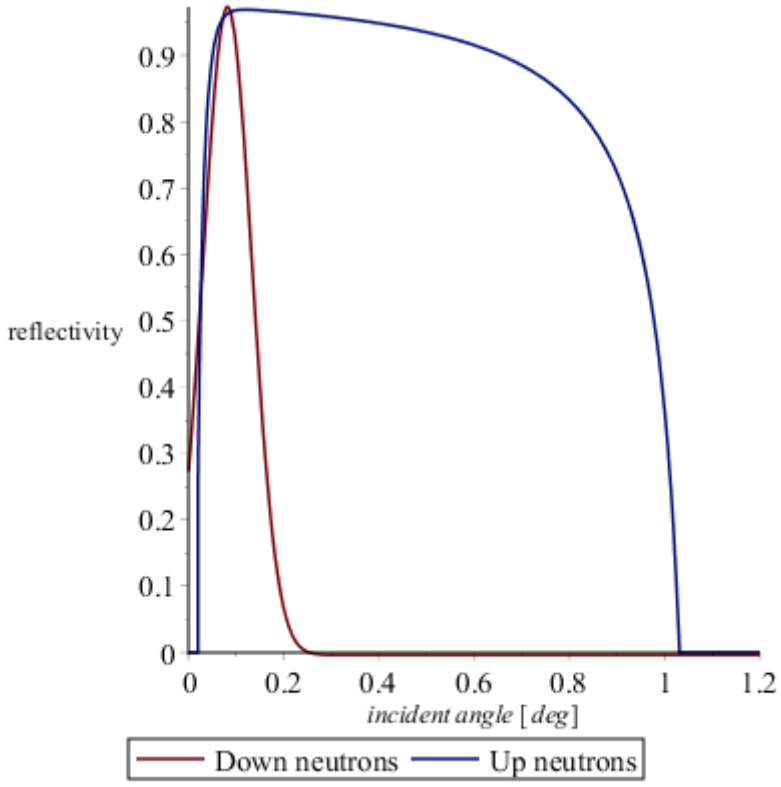

Fig. 34: Reflectivity curves for our deflectors as recreated from manufacturer data

Fig. 34 shows the reflectivity curve for a mono-layer mirror and a beam without any divergence, given by equations (87) and (88).

The probability for a double reflection depends on the geometry of the wafer, explicitly its length L and thickness d. We can write $D_1^{\uparrow\downarrow}(\alpha,\gamma_1)$ as

$$\mathrm{D}_1^{\uparrow\downarrow}(\alpha,\gamma_1)=\begin{cases}\left(\frac{\mathrm{L}}{\mathrm{d}}(\alpha-\gamma_1)-1\right)\mathrm{R}_0^{\uparrow\downarrow 2}(\gamma_1-\alpha) & \text{for } \alpha-\gamma_1>\frac{\mathrm{d}}{\mathrm{L}}\\ 0 & \text{else}\end{cases} \tag{90}$$

The index (here 1) denotes which deflector is under consideration, with deflector 1 being the first deflector in beam direction. From this we get the following transmission function for deflector 1:

$$\mathrm{T}_1^{\uparrow\downarrow}(\alpha,\gamma_1)=1-\mathrm{R}_1^{\uparrow\downarrow}(\alpha,\gamma_1)=1-\mathrm{R}_0^{\uparrow\downarrow}(\gamma_1-\alpha)+\mathrm{D}_1^{\uparrow\downarrow}(\alpha,\gamma_1) \tag{91}$$

For the second deflector we get similar expressions if we replace the index 1 by 2.

Neutrons that are reflected at the first deflector, leaving it under an angle of $2\gamma_1$-α and transmit the second deflector can be described with the following probability formula

$$\mathrm{W}_1^{\uparrow\downarrow}(\mathrm{x_S},\alpha,\gamma_1,\gamma_2)=\mathrm{W}_S^{\uparrow\downarrow}(x_S)W_c(\alpha)\mathrm{R}_1^{\uparrow\downarrow}(\alpha,\gamma_1)\mathrm{T}_2^{\uparrow\downarrow}(2\gamma_1-\alpha,\gamma_2) \tag{92}$$

Because of the large divergence of our beam after interaction with the sample, compared to the width of the analyzer crystals, not all spin-down neutrons in the beam will hit the first deflector. The remaining spin-down neutrons reach the second deflector, which is tilted in opposite direction from the first deflector by an angle γ_2 (>0). For this second deflector we get an equation for the reflection probability in much the same way as for the first deflector. See equation (92).

$$\mathrm{W}_2^{\uparrow\downarrow}(\mathrm{x_S},\alpha,\gamma_1,\gamma_2)=\mathrm{W}_\mathrm{S}^{\uparrow\downarrow}(\mathrm{x_S})\mathrm{W_c}(\alpha)\mathrm{R}_2^{\uparrow\downarrow}(\alpha,\gamma_2)\mathrm{T}_1^{\uparrow\downarrow}(\alpha,\gamma_1) \tag{93}$$

Using these equations for reflectivity of the deflectors ((87) and (88)), double reflection at (90) and transmission (91) through the deflectors we can use the probabilities given by (92)and (93) to simulate our beam profile at the PSD position. This is done by calculating neutron distribution for both spin directions at the distance of the PSD.

A simulation of our beam profile is shown in Fig. 35. The lower row shows the beam profile after the first deflector, while the beam profile after the second deflector is shown on top. Up and down neutron intensities are shown separately with up intensities on the right.

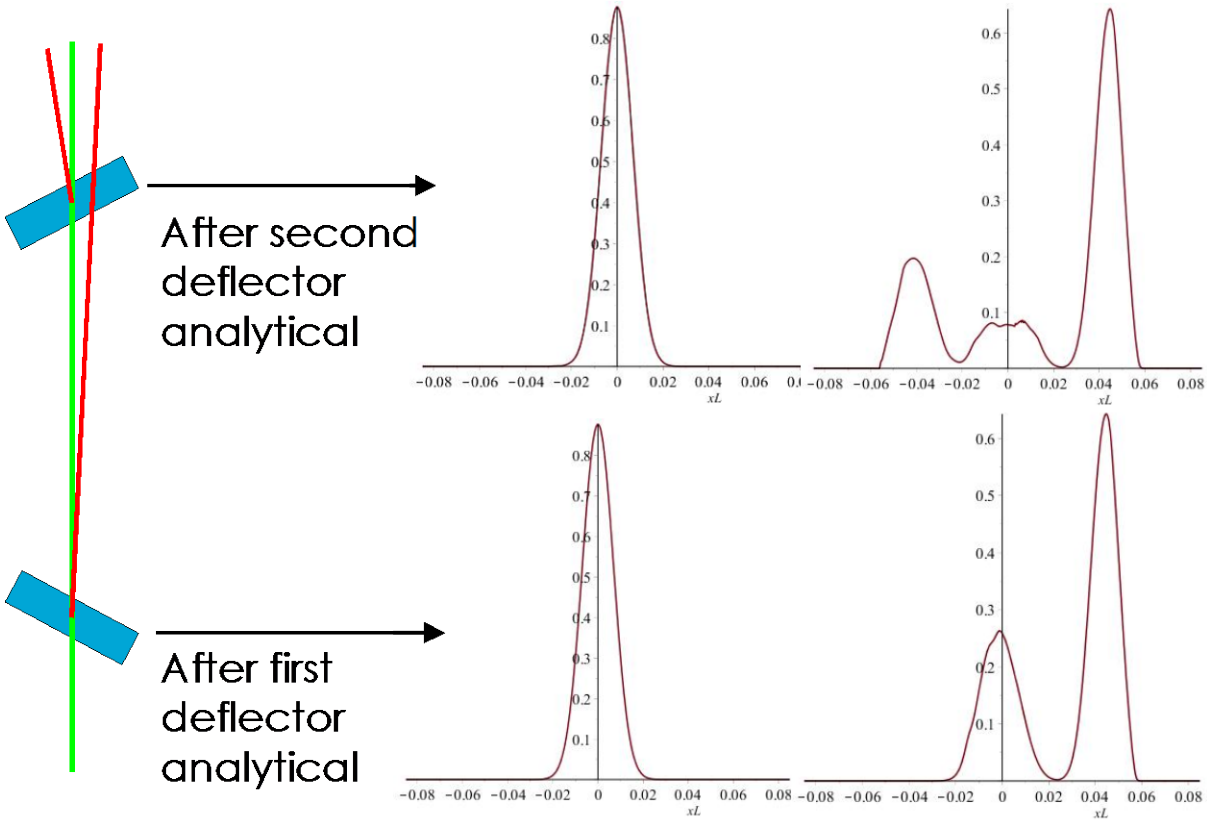

Fig. 35: Results for the analytical calculations after the first and second deflector. Calculations were done in Maple.

A comparison between the analytical calculation and McStas simulation is shown in Fig. 36. Agreement between two methods gets better for smaller sample sizes, with good agreement starting at samples of 2 cm radius. Otherwise McStas produces a broader and more triangular profile. In the shown comparison for a 2 cm sample integrated intensity for the small, left beam is nearly identical, the central beam shows a small deviance, while the right beam shows nearly 23% difference in integrated intensity. The main reason for this is the broader profile of the McStas simulation, but looking at our experimental data (for example in Fig. 18 and Fig. 27) the analytical calculated profile with its sharper and clearer separated peaks is a better fit to our measurements.

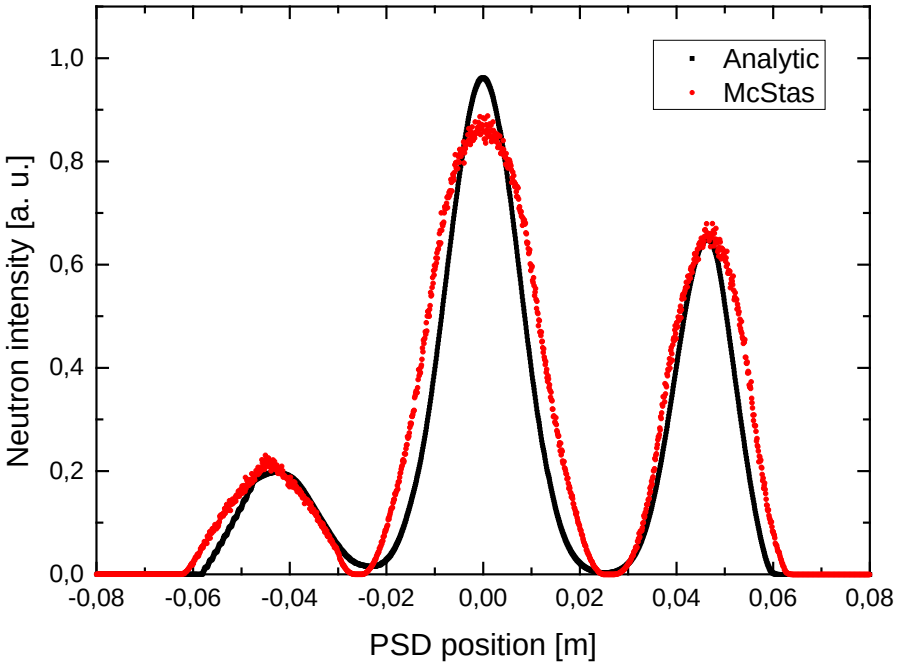

Fig. 36: Comparison between analytical calculations and McStas simulation of the PSD beam-profile for a 2 cm sample

McStas simulations were done by Oleg Sobolev[7] to model the PUMA polarization analysis setup. We learned that the analytical treatment of the problem provided very similar results; again see Fig. 36 for a comparison between McStas and our analytical approach. There simulations for a 2 cm sample size are shown and the peak positions for both methods are a nearly perfect match. The largest deviation is in the form of the low intensity peak produced by the second deflector. Here McStas produces a rather triangular profile not matching any of our measurements. It should be noted that agreement between the analytical approach and McStas was only reached in calculations using sample sizes of 2 cm or less. For larger sample sizes the peak position was still good, but the shape and width of the side peaks started to deviate strongly.

[7] Oleg Sobolev was the PUMA instrumental scientist for the larger part of this work and strongly involved in the polarization analysis setup

If we want to calculate the intensities for our setup we also have to take interactions with the analyzer crystals into account as well as the single detectors.
At a distance y_A from the center of the multianalyzer, neutrons that were deflected at the first deflector and transmitted by the second (see equation (92)) arrive with a lateral displacement of

$$x_1(x_S, \alpha, \gamma_1) = (L_{SA} - L_{SD1} - y_A)\tan(2\gamma_1 - \alpha) + x_S + L_{SD1}\tan(\alpha) \qquad (94)$$

L_{SA} is the sample-analyzer distance and L_{SD1} the distance between sample position and first deflector. Now, with an analyzer centered at (x_A,y_A) and tilted by an angle of θ_A(<0), we can write down the probability that a neutron is reflected by the analyzer and reaches the detector corresponding to the analyzer crystal by:

$$W_{A,1}(x_S, \alpha, \gamma_1) = R_A \exp\left(-4\ln 2\left(\frac{\Theta_0 - \Theta_A + 2\gamma_1 - \alpha}{\eta_A}\right)^2\right)\exp\left(-4\ln 2\left(\frac{x_1(x_S, \alpha, \gamma_1) - x_A}{B_A \sin\Theta_A}\right)^2\right) \qquad (95)$$

The first exponential expression describes the mosaic distribution of the analyzer crystal hit by a neutron under an angle of θ_A-(2γ_1-α). For neutrons with a wavelength of 2.36 Å the ideal Bragg-angle for pyrolytic graphite (PG), as used within the PUMA multianalyzer, is θ_0=-20.6°. Other parameters of the analyzer we need are the mosaicity of the crystal, η_A, and its peak reflectivity, R_A. The finite width of the analyzer blade, B_A, is taken into account in the second exponential expression, describing the probability that the blade is hit by the incoming neutrons.
Just as in the analytical treatment of the resolution function in the paper of Eckold and Sobolev [19], the Gaussian approximation appears as a good approximation. Alternatively it could also be exchanged by an expression like equation (84).
After being reflected at the second deflector (see equation (93)) the neutrons are now located at a distance of L_{SD2} from the sample and have a divergence angle of 2γ_2-α. They hit an analyzer crystal centered at (x_A,y_A) at

$$x_2(x_S, \alpha, \gamma_2) = (L_{SA} - L_{SD2} - y_A)\tan(2\gamma_2 - \alpha) + x_S + L_{SD2}\tan(\alpha) \qquad (96)$$

where they are reflected with the probability

$$W_{A,2}(x_S, \alpha, \gamma_2) = R_A \exp\left(-4\ln 2\left(\frac{\Theta_0 - \Theta_A + 2\gamma_2 - \alpha}{\eta_A}\right)^2\right)\exp\left(-4\ln 2\left(\frac{x_2(x_S, \alpha, \gamma_2) - x_A}{B_A \sin\Theta_A}\right)^2\right) \qquad (97)$$

While calculating the beam profile for our experiment it is necessary to take into account the possibility of double reflections inside our two deflectors. This is effectively the same as if the neutron had passed all mirrors without being reflected. For the neutrons that are transmitted at the second deflector or experience a double reflection we obtain a probability of

$$W_0^{\uparrow\downarrow}(x_S, \alpha, \gamma_1, \gamma_2) = W_S^{\uparrow\downarrow}(x_S) W_c(\alpha) T_1^{\uparrow\downarrow}(\alpha, \gamma_1) T_2^{\uparrow\downarrow}(\alpha, \gamma_2) \tag{98}$$

$$x_0(x_S, \alpha) = (L_{SA} - y_A)\tan(\alpha) + x_S \tag{99}$$

They are reflected by an analyzer at (x_A,y_A) with the probability

$$W_{A,0}(x_S, \alpha) = R_A \exp\left(-4\ln 2\left(\frac{\Theta_0 - \Theta_A + \alpha}{\eta_A}\right)^2\right) \exp\left(-4\ln 2\left(\frac{x_0(x_S, \alpha) - x_A}{B_A \sin\Theta_A}\right)^2\right) \tag{100}$$

(here the small parallel shift of the neutron after double reflection is neglected)
For a configuration using the three analyzers 5,6 and 7, which are centered at (x_5,y_5), (x_6,y_6), (x_7,y_7) with tilt angles θ_5, θ_6, θ_7, respectively, we can represent the individual count rates in the following way:

$$\begin{aligned} I_i = \iint_{-\infty}^{\infty} \Big[& \left(W_1^{\uparrow}(x_S, \alpha, \gamma_1, \gamma_2) + W_1^{\downarrow}(x_S, \alpha, \gamma_1, \gamma_2)\right) W_{i,1}(x_S, \alpha, \gamma_1) \\ & + \left(W_2^{\uparrow}(x_S, \alpha, \gamma_1, \gamma_2) + W_2^{\downarrow}(x_S, \alpha, \gamma_1, \gamma_2)\right) W_{i,2}(x_S, \alpha, \gamma_2) \\ & + \left(W_0^{\uparrow}(x_S, \alpha, \gamma_1, \gamma_2) + W_0^{\downarrow}(x_S, \alpha, \gamma_1, \gamma_2)\right) W_{i,0}(x_S, \alpha) \Big] dx_S d\alpha \\ & \text{for } i = 5,6,7 \end{aligned} \tag{101}$$

We assume here that for all three channels the corresponding detectors have identical efficiencies. The expression includes the possibility of cross talk effects between the three different channels. Usually cross talk can be minimized by a careful choice of the geometric parameters, so that the neutrons reflected at the first deflector reach analyzer 7, neutrons reflected on the second analyzer 5 and transmitted neutrons analyzer 6 exclusively. For this only the probabilities $W_{6,0}$ and $W_{7,1}$ are non-zero and equation (101) is reduced to:

$$I_5 = \int_{-\infty}^{\infty} \int_{-\frac{B_S}{2}}^{\frac{B_S}{2}} \left[S^{\uparrow} W_2^{\uparrow}(x_S, \alpha, \gamma_1, \gamma_2) + S^{\downarrow} W_2^{\downarrow}(x_S, \alpha, \gamma_1, \gamma_2)\right] W_{5,2}(x_S, \alpha, \gamma_2) dx_S d\alpha \quad (102)$$

$$I_6 = \int_{-\infty}^{\infty} \int_{-\frac{B_S}{2}}^{\frac{B_S}{2}} \left[S^{\uparrow} W_0^{\uparrow}(x_S, \alpha, \gamma_1, \gamma_2) + S^{\downarrow} W_0^{\downarrow}(x_S, \alpha, \gamma_1, \gamma_2)\right] W_{6,0}(x_S, \alpha) dx_S d\alpha \quad (103)$$

$$I_7 = \int_{-\infty}^{\infty} \int_{-\frac{B_S}{2}}^{\frac{B_S}{2}} \left[S^{\uparrow} W_1^{\uparrow}(x_S, \alpha, \gamma_1, \gamma_2) + S^{\downarrow} W_1^{\downarrow}(x_S, \alpha, \gamma_1, \gamma_2)\right] W_{7,1}(x_S, \alpha, \gamma_1) dx_S d\alpha \quad (104)$$

The used integration limits for x_S-integration are a result of equation (84). $S^{\uparrow}/S_{\downarrow}$ are the flux of scattered spin up/down neutrons, see equation (84).

Using typical set-up conditions, the deflectors do not reflect spin-up neutrons and, consequently, $W_1^{\uparrow}(x_S, \alpha, \gamma_1, \gamma_2)$ and $W_2^{\uparrow}(x_S, \alpha, \gamma_1, \gamma_2)$ vanish. Therefore equations (102) and (104) are further simplified to yield:

$$I_5 = S^{\downarrow} \int_{-\infty}^{\infty} \int_{-\frac{B_S}{2}}^{\frac{B_S}{2}} W_2^{\downarrow}(x_S, \alpha, \gamma_1, \gamma_2) W_{5,2}(x_S, \alpha, \gamma_2) dx_S d\alpha = A' S^{\downarrow} \quad (105)$$

$$I_7 = S^{\downarrow} \int_{-\infty}^{\infty} \int_{-\frac{B_S}{2}}^{\frac{B_S}{2}} W_1^{\downarrow}(x_S, \alpha, \gamma_1, \gamma_2) W_{7,1}(x_S, \alpha, \gamma_1) dx_S d\alpha = A'' S^{\downarrow} \quad (106)$$

While equation (103) may be written as:

$$I_6 = CS^{\uparrow} + DS^{\downarrow} \quad (107)$$

with

$$A' = \int_{-\infty}^{\infty} \int_{-\frac{B_S}{2}}^{\frac{B_S}{2}} W_2^{\downarrow}(x_S, \alpha, \gamma_1, \gamma_2) W_{5,2}(x_S, \alpha, \gamma_2) dx_S d\alpha \quad (108)$$

$$A'' = \int_{-\infty}^{\infty} \int_{-\frac{B_S}{2}}^{\frac{B_S}{2}} W_1^{\downarrow}(x_S, \alpha, \gamma_1, \gamma_2) W_{7,1}(x_S, \alpha, \gamma_1) dx_S d\alpha \tag{109}$$

$$C = \int_{-\infty}^{\infty} \int_{-\frac{B_S}{2}}^{\frac{B_S}{2}} W_0^{\uparrow}(x_S, \alpha, \gamma_1, \gamma_2) W_{6,0}(x_S, \alpha) dx_S d\alpha \tag{110}$$

$$D = \int_{-\infty}^{\infty} \int_{-\frac{B_S}{2}}^{\frac{B_S}{2}} W_0^{\downarrow}(x_S, \alpha, \gamma_1, \gamma_2) W_{6,0}(x_S, \alpha) dx_S d\alpha \tag{111}$$

Because of this reflection behavior of the deflectors the intensities of channels 5 and 7 are proportional to $S^{\downarrow}$, i.e. the flux of scattered spin-down neutrons while channel 6 counts events of both neutron-spin directions. Since the quantities *A', A", C* and *D* can be calculated from the characteristic data of deflectors and analyzers as well as the geometrical parameters, we are able to determine the polarization of the scattered beam according to[8]

$$P_S = \frac{S^{\uparrow} - S^{\downarrow}}{S^{\uparrow} + S^{\downarrow}} = \frac{1 - D_+ \left(\frac{I_5 + I_7}{I_6}\right)}{1 - D_- \left(\frac{I_5 + I_7}{I_6}\right)} \tag{112}$$

with the abbreviation

$$D_{\pm} = \frac{D \pm C}{A' + A''} \tag{113}$$

While we can calculate these quantities in the demonstrated manner, they can also be determined experimentally. This is a good way to check the accuracy of the analytical calculations.
If we solve for the intensity ratio of deflected and transmitted beams we get:

[8] As usual, the intensities need to be corrected for background before the polarization can be determined. This can be achieved by using the other eight detectors of the multianalyzer system that are not used for the polarization analysis as background counters as described in chapter 5.2 Data reduction.

$$\frac{I_5 + I_7}{I_6} = \frac{1 - P_S}{D_+ - D_- P_S} \tag{114}$$

For an unpolarized beam ($P_S = 0$) we obtain

$$\left(\frac{I_6}{I_5 + I_7}\right)_{P_S=0} = D_+ \tag{115}$$

The remaining parameter D_- can be calculated from an additional measurement for a known polarization P_s such as provided by a ^{3}He-filter with well-known properties:

$$D_- = D_+ + \frac{P_S - 1}{P_S}\left(\frac{I_6}{I_5 + I_7}\right)_{P_S} = \left(\frac{I_6}{I_5 + I_7}\right)_{P_S=0} + \frac{P_S - 1}{P_S}\left(\frac{I_6}{I_5 + I_7}\right)_{P_S} \tag{116}$$

Taking into account these calibration factors and the non-ideal polarization of the incident neutron beam $P_0 \neq 0$, the probability for spinflip scattering is obtained as:

$$\hat{S} = \frac{1}{2}\left(1 - \frac{P_S}{P_0}\right) = \frac{1}{2} - \frac{1}{2P_0}\frac{I_6 - D_+(I_5 + I_7)}{I_6 - D_-(I_5 + I_7)} \tag{117}$$

From this the true spinflip and non-spinflip intensity rates can be calculated using the detector count rates to yield:

$$I_{SF} = \frac{1}{2}I_6 - \frac{D_-}{2}(I_5 + I_7) - \frac{1}{2P_0}\left(I_6 - D_+(I_5 + I_7)\right) \tag{118}$$

and

$$I_{NSF} = \frac{1}{2}I_6 - \frac{D_-}{2}(I_5 + I_7) + \frac{1}{2P_0}\left(I_6 - D_+(I_5 + I_7)\right) \tag{119}$$

Now to measure the incident polarization p_0 we can make use of a Mezei flipper.
For an unpolarized incident neutron beam, meaning P=0, we find:

$$\left(\frac{I_5 + I_7}{I_6}\right)_{P=0}^{off} = \left(\frac{I_5 + I_7}{I_6}\right)_{P=0}^{on} \tag{120}$$

With the assumption, that we have only SF scattering, for example a completely magnetic signal without any nuclear components, there would be a SF probability S of *S*=1. In this case we can determine the incident polarization by using that:

$$P_0 = \left(\frac{I_5^{norm} + I_7^{norm}}{I_{tot}^{norm}}\right)_{S=1}^{off} - \left(\frac{I_5^{norm} + I_7^{norm}}{I_{tot}^{norm}}\right)_{S=1}^{on} \tag{121}$$

Here I_{tot}^{norm} and $I_{5/7}^{norm}$ are the total normalized intensity of all three analyzer channels respective channel 5 and 7. As this is a rather rare occurrence we will use a case where we only have NSF intensity, such as scattering on a lattice reflection, meaning *S*=0. From this we get:

$$P_0 = \left(\frac{I_5^{norm} + I_7^{norm}}{I_{tot}^{norm}}\right)_{S=0}^{off} - \left(\frac{I_5^{norm} + I_7^{norm}}{I_{tot}^{norm}}\right)_{S=0}^{on} \tag{122}$$

If we have normalized all count rates, using determined detector and analyzer efficiencies we can directly measure the polarization of our neutron beam.

This means that with a direct beam setup using our flipper, see 3.6 “Mezei Flipper” we can now use equation (122) to determine the polarization of the incident beam P directly by measuring a pure NSF reflection. This allows easy checking of the polarization during two measurements of an experiment which is very useful to control if the polarization calculated from the helium-cell parameters is correct.

5 Experiments

Of course the developing and implementing a new method of neutron polarization analysis is not an end in itself. During this work several crystalline samples were measured, some of them in the earliest state of development and some with the optimized polarization analysis. First and short experiments where done on Vanadium and a hematite sample as proof of principle. The largest part of this chapter will be used for copper-oxide, which again, started as another proof of principle experiment, but led us to some interesting, and unexpected new findings showing the value and potential of polarized neutron experiments in general and our new method in particular.
In the following chapter each of these experiments will be described in some detail. There will be also some remarks regarding the characteristics of the finished setup. We will start with a direct beam test, followed by a general overview of what was done with the raw data from a given experiment, and finally the first experiments done with the new polarization setup will be discussed.
For our first test experiments, before the measurements on CuO starting August 2016, we used a ^{3}He-filter cell with a P_{He} of 80.9 % and 2.38 bar pressure resulting in a polarization for the incident neutron beam of P_n=0.9996 for λ=2.36 Å. The resulting transmission is T=0.1832.
For experiments after finishing the setup, meaning everything after August 2016, notably the copper-oxide measurements, this was relaxed to P_{He}=75 %, p=0.975 bar and P_n=0.9277 for λ=2.36 Å. Transmission for this cell was significantly higher at T=0.3037 resulting in an intensity gain of more than 65%.

5.1 Testing the analytical model

One of the first points of interest was if our analytical calculation for the beam profile was reproducible in a measurement.
Without the multianalyzer crystals (either by not installing the analyzer, or more simply by rotating the crystals away from their reflecting angle), the PSD can be used to observe the distribution of the scattered neutrons. This is of some interest for the polarization analysis to monitor the effects of the deflectors, their position and their angle on the neutron beam. In our typical configuration using two deflectors we get three distinct peaks on the PSD, one direct beam and one additional component per deflector. A typical profile for an unpolarized direct beam is shown in Fig. 37 a) in black. The central peak is identical to the transmitted beam, while the two side peaks can be attributed to the two used deflectors. The smaller one on the left originates form the second deflector and the larger on the right from the first one.

If we now move the analyzers into reflecting position most of the neutrons should be relayed to the single detector tubes of the MD. This can be seen in the PSD image as a loss of intensity as the neutrons hitting the analyzers/single detectors no longer reach the PSD. The beam profile with reflecting analyzers is shown in Fig. 37 a) as the red curve. When the dip in the profile is centered this means that the analyzer is hit in its center by the incoming neutron beam.

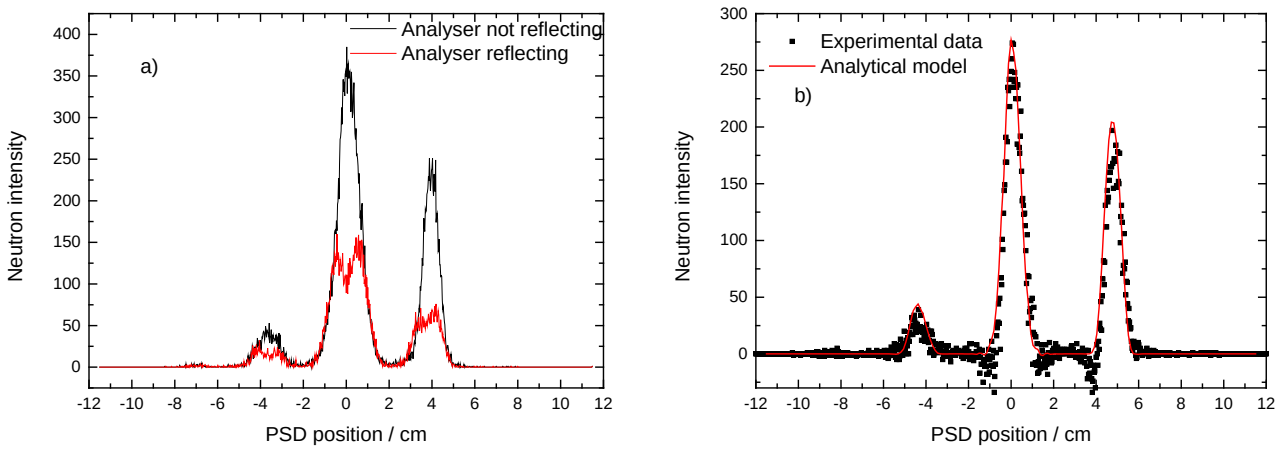

Fig. 37: a) Intensity profile of the position sensitive detector in the unpolarized, direct beam with (red) and without (black) analyzers.
b) Reflected intensity (black) and calculated angular profile (red) according to parameter set listed in Table 6

For this test, a sample slit of 1cm was used, simulating a rather large sample. Because the resulting beam is somewhat larger than the effective width of a single analyzer crystal ($B_A \sin\theta_0$ = 0.88 cm), only around 50% of the incoming neutrons are reflected towards the MD.

Using the analytical formalism introduced in 4.3.1 “Analytical calculations for PUMA polarization analysis” the difference between both profiles, meaning the neutrons reaching the single detectors, can be calculated. As shown in Fig. 37 b) the calculated curve almost perfectly describes the experimental data if the parameter set from Table 6 is used[9].

If we integrate over the three peaks of the reflected/calculated angular intensity distribution the result will be proportional to the count rates of the corresponding MD single detectors. With these data, the calibration parameters *A*’, *A*”, *A, C, D, D*$_+$, *D*$_-$ can be obtained using equations (108) to (113). Using the parameters from Table 6 and equation (112) we arrive at the conclusion that in this

[9] Note, that for the direct beam (zero scattering angle) the effective collimation of the beam is determined by the combination of all collimator divergencies and the mosaicity of the monochromator.

configuration roughly 8% of spin-down neutrons are not reflected by the deflectors. These neutrons reach the central analyzer and detector channel (no. 6) and have to be taken into account while calculating the spin-flip/non-spin-flip intensities. This allows us to calibrate our experimental data so that we get quantitative and accurate information about the polarization of the scattered beam. For example a perfect unpolarized beam should result in the same count rates in both channels. This however will not be the case, as experimental imperfections, such reflectivity <1 will result in an intensity distribution differing from the ideal. To correct for this we have our calibration parameters. In a test measurement we found good agreement between our data and a calculated calibration parameter of D_+=1.05. See equation (115). The calibration parameter $D_\pm$ strongly depends on sample size, or, with no sample, the width of the slits in front and after the sample position. The same parameter only weakly depends on the rest of the possible parameters of the deflector-MAD-system; even beam divergence of the scattered beam has only some small influence. Nevertheless the calibration parameters have to be carefully adapted to the actual setup of each experiment.

k_f	Scattered wave vector	2.662 Å^{-1}
B_S	*Width of sample slit*	10 mm
α_C	Collimator divergence	0.5°
θ_0	Bragg angle of the analyzer	-20.6°
η_A	Analyzer mosaicity	0.4°
B_A	Analyzer width	25 mm
d	Thickness of deflector wafer	0.55 mm
L	Deflector length	40 mm
L_{SA}	*Distance sample-analyzer center*	1413 mm
L_{SD1}	*Distance sample-deflector1*	613 mm
L_{SD2}	*Distance sample-deflector2*	663 mm
γ_1	*Tilt angle of deflector 1*	-0.81°
γ_2	*Tilt angle of deflector 2*	0.71°
x_5	Transverse displacement of analyzer 5	20 mm
x_6	Transverse displacement of analyzer 6	0 mm
x_7	Transverse displacement of analyzer 7	-20 mm
y_5	*Longitudinal displacement of analyzer 5*	-56.8 mm
y_6	Longitudinal displacement of analyzer 6	0 mm
y_7	*Longitudinal displacement of analyzer 7*	92.8 mm
θ_5	*Rotation angle of analyzer 5*	-19.1°
θ_6	Rotation angle of analyzer 6	-20.6°
θ_7	*Rotation angle of analyzer 7*	-22.2°
A'	**Expected intensity of spin-down neutrons in channel 5**	74.35
A''	**Expected intensity of spin-down neutrons in channel 7**	221.86
C	**Expected intensity of spin-up neutrons in channel 6**	282.28
D	**Expected intensity of spin-down neutrons in channel 6**	27.42
D_+	**Calibration parameter**	1.05
D_-	**Calibration parameter**	-0.86

Table 6: List of parameters for polarization analysis as used in the fit shown in **Fig. 37** b). Some parameters are mostly fixed (normal type) if the analyzer itself isn't tilted, some change depending on the exact setup (*italic type*), and the parameter after the break in the table are calculated (**bold type**).

5.2 Data reduction

The first step in our data reduction is to calculate the time dependent polarization of the He-cell. Typically we start with a cell polarization between P_{He}= 73-75%. The cell has a relaxation time T_R greater than 100 h, as shown in the paper about the magnetostatic cavity used in this work by Hutanu et al. [8] giving a relaxation time of 150 h, or our own measurements, showing T_R=100 h, see 3.1.1 “Relaxation time in the PUMA polarization analysis setup”. The data for our setup and guide field is shown Fig. 13. There are small variations in relaxation time for each cell, but the impact of the magnetic environment the cell is used in is much bigger. Under ideal circumstances one should always confirm relaxation time for a given setup by measuring beam polarization from time to time, but using our measured T_R=100(22) h still gives good results for calculating incident beam polarization as there are only minor deviations in final result between using our measurement or the data from the Hutanu paper. With this information the time dependent He-polarization can be calculated with the following equation:

$$P_{He}(t) = P_{He} \cdot e^{-t/T_R} \tag{123}$$

Using the timestamp for each scan, and each data point of each scan, we can now calculate the time-dependent Helium polarization of our spin filter cell. From this we can calculate the neutron polarization of the incident beam, using equation (124)

$$P(0) = \tanh(P_{He}(t) \cdot 0{,}0732 \cdot p[bar] \cdot l[cm] \cdot \lambda[\text{Å}]) \tag{124}$$

We now should have a $P(0)$value for each data-point which is later used to determine the SF/NSF components of scattered beam.

5.2.1 Normalizing detectors

All detectors have to be normalized to take differences of their counting behavior, originating in small deviations of the detectors and their electronics, into account. One way to do this is to place the detectors of the MD equidistant from each other (for example 4°) and expose all of them to a reflected beam without a sample and with only the central analyzer crystal in reflective position. Then, in this configuration, conduct a CAD scan. This means that we rotate the whole MD as far as possible around the analyzer center while the analyzers stay immobile, moving each detector

through the beam. The scan only detects the reflected beam from the central channel, as no sample, deflector, or other analyzer should be in the beam path. An example of such a scan where all but the central analyzer are in non-reflecting position is shown in Fig. 38.

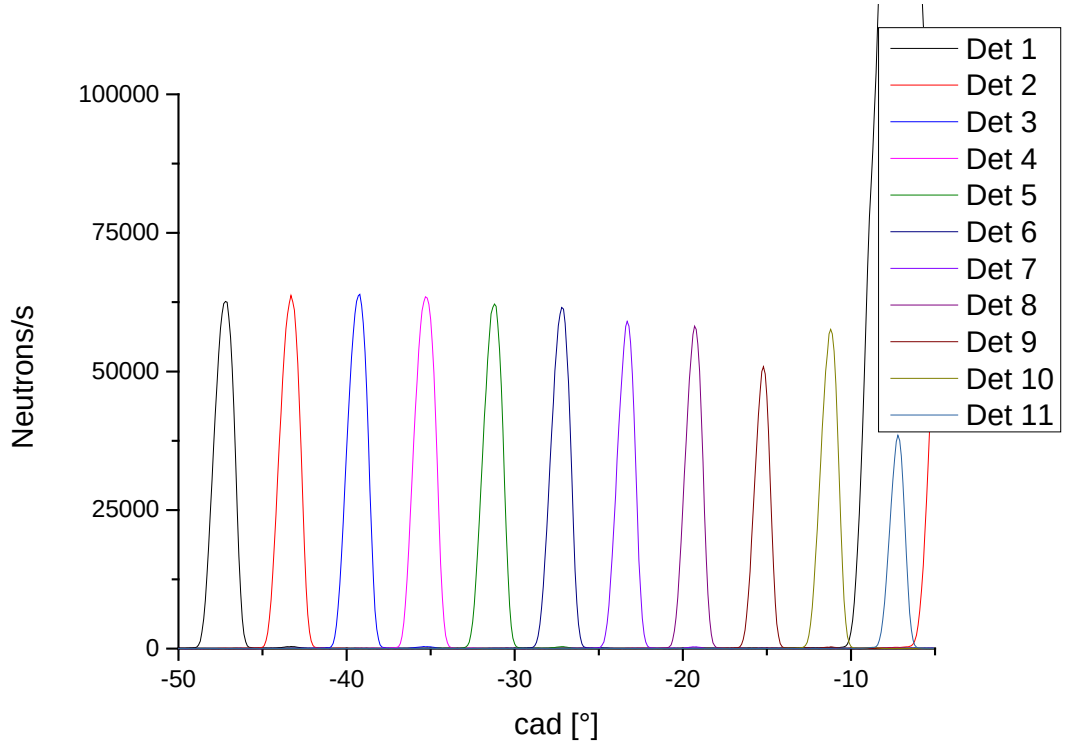

Fig. 38: cad-scan of all eleven detectors of the MD used for normalizing the detector intensities

What we see here is how each of the eleven detectors is moving though the beam, producing a series of equidistant Gaussian profiles. The upcoming, very strong signal for small absolute value of cad-angles is the direct beam, not reflected by the central analyzer. It is first observed in detector 1 and then starts to turn up in detector 2, as expected. Integrating over the whole peak (excluding the direct beam peaks) gives us a data set to normalize our count rates for the respective detectors. Here only detectors number nine and eleven have an abnormally large aberration, but even the other detectors still have up to 15% differing counting rates.

5.2.2 Background determination

After normalizing the count-rates the next step is elimination of our detector background. Since we use only three of the eleven MD single detectors to measure the signal there are eight detectors counting background. Therefore for background reduction with the MA polarization analysis setup it

is a good idea to use these eight detectors, as all of them still count the neutron background in the analyzer box to establish mean background values and to give information about possible background variations. This can be done by subtracting the mean counts of detectors 1-4 from detector 5, of 9-11 from detector 7 and the mean of 1-4 and 8-11 from detector 6 in the simplest case. Using just the closest side detectors without taking their mean will not work as even in pure background there can be large intensity variations from scan-point to scan-point for a single detector. If there is a background gradient its influence on the used detectors can be estimated by comparing the side detectors[10]. If there is a localized higher background , for example if the measurement takes place near the direct beam, the side detectors can be used to extrapolate if the background trend influences one or more of the used detectors.

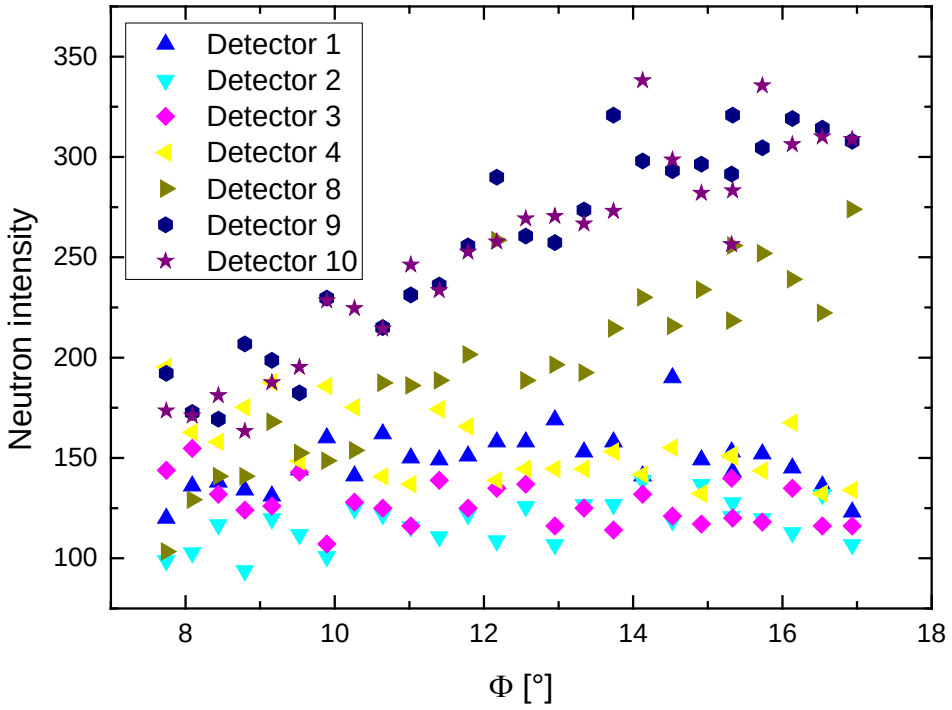

Fig. 39: Count rates of the side detectors during a scan. Detectors 1-4 show constant background while detectors 8-10 show an increasing background with higher values of the sample angle Φ. It is interesting to note that the increase in background for detector 8 starts later then for detector 9 and 10, giving us an indication where the increasing background originates. (Detector 11 not shown for massive over-counting)

[10] In this work the side detectors used to determine background counting rates were placed at the extreme ends of their movement-range. For future observations it's recommended to place them in an equidistant fashion as shown in Fig. 76 in the appendix

Another example could be stray neutrons from somewhere within our instrument, or a beam coming from one of the neighboring experiments. So when detector one and two show increased counting rates after normalizing all detectors while detectors three and four do not show increased intensity this indicates a localized phenomenon that's not concerning detector five. On the other hand, a background that shows a trend over detectors 1-4 but not 8-11 has to be taken into account for detector five, and depending on the trend also for six. An example for a background trend is shown in Fig. 39.

How to do the background correction also depends on the type of scan. Using a constant q-scan as an example, where the scan duration was determined by monitor counts, we have very different counting times for each energy value and thus different background count-rates. So we can't use the mean of detector four to correct detector five without normalizing for time. What we can do is to use the mean of detector one to four for each energy-point to correct detector five. In this case background correction has to be done point by point as the whole analyzer/detector box is moving during the scan. This opens up the possibility of the detectors encountering different background environments, such as stray neutrons from neighboring experiments, during different parts of the scan.

On the other hand, using the mean of detector four as background is a good estimation for a constant energy-scan without any contamination resulting in a background trend.

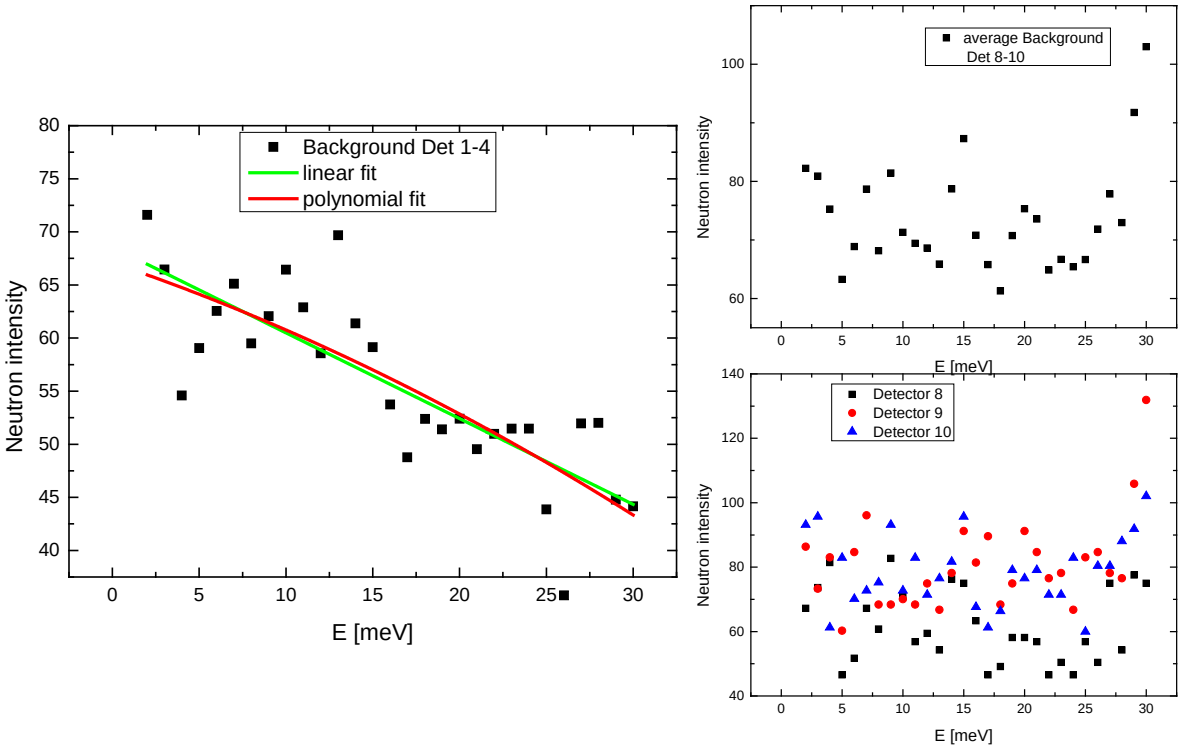

Fig. 40: Background for an energy scan. On the left is the average count-rate of detector 1-4, showing a clear trend to lower background for higher energies. On the right side is the average of detector 8-10 on top showing a higher, but trendless background. The steep increase for the last two points is the result of higher intensity in the two outermost detectors. This indicates a localized effect. Again detector 11 is ignored due to highly over-counting.

A complex example for the backgrounds used to correct an energy scan is shown in Fig. 40. Not only is there an energy dependent trend, there are also localized background difference which can be seen where the low numbered detectors show decreasing background for higher energies while the higher numbered detectors show constant level background (with the exception of the last two energy values). Best practice for such an incident was to take the trend of detectors 1-4 into account for the background of detectors 5 by using the fitted value for each energy, the mean of detectors 8-10 for the background of detectors 7 and a combined approach for detector 6.

5.2.3 Calculating SF/NSF intensities

Now we take the background corrected intensities of the three detectors and apply the correction factors calculated using equation (113) to find the SF and NSF intensities of our scattered beam using equations (118) and (119).

During an experiment the correction factors are calculated by using the software available at PUMA. Needed for the calculation are the distances between the sample and the first deflector, as well as the distance between deflector and analyzer center. All other distances and angles result from these distances see 3.7 “Calculating the polarization analysis Multianalyzer/-detector positions”.

To calculate the correction factors via the script available at PUMA we also need the effective collimation of the beam. Usually collimation of the primary beam is not needed for SF/NSF calculation. In this case only collimation occurring after scattering at the sample is of interest. But when using the direct beam effective collimation is a result of the combination all used collimators (α_1, α_2, polarization analysis collimator), and also of the mosaicity of the monochromator. As a direct beam configuration can be utilized during some calibration steps it is good to know how to get effective collimation.

The effective collimation of a series of collimators can be described by

$$\alpha_{eff} = \sqrt{\frac{1}{\frac{1}{(\alpha_1)^2} + \frac{1}{(\alpha_2)^2} + \frac{1}{(\alpha_3)^2} + \cdots}} \tag{125}$$

The resulting effective collimation of our system (from α_1, α_2, coll,…) can then be utilized as a parameter to calculate the correction parameters for the SF/NSF calculations. The full set of parameters necessary to get the correction parameters for the SF and NSF intensities is shown in Table 6.

Now, using equations (118) and (119) we can calculate two numbers, one for the spin-flip (SF) and one for non-spin-flip (NSF) component of our scattered neutron beam.

5.2.4 Data processing example

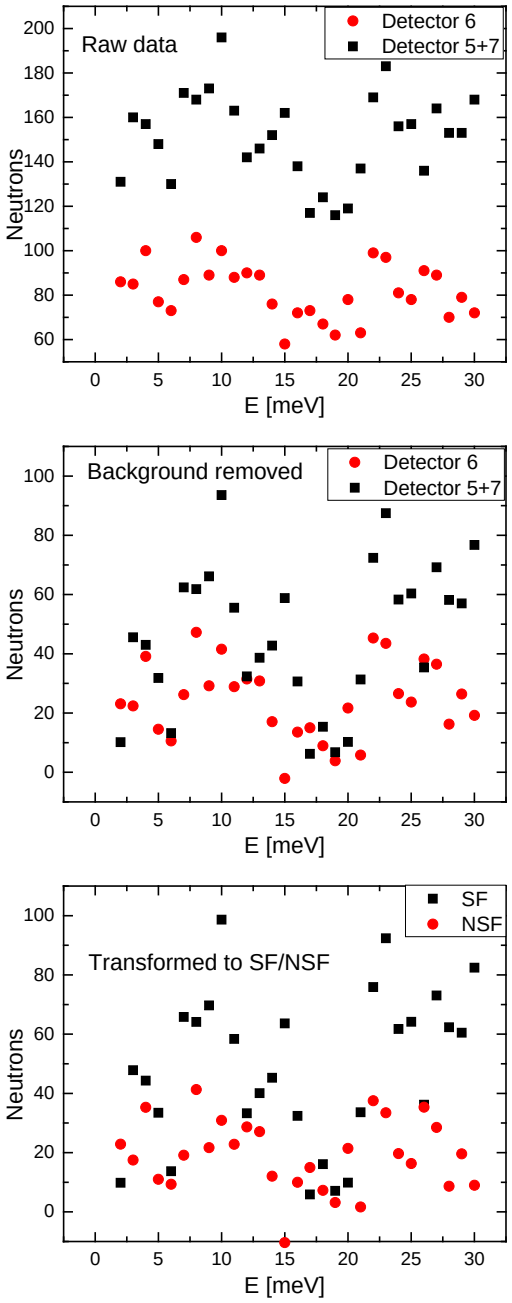

Fig. 41: Three plots of the same data set used to illustrate the data reduction process

An illustration of the whole data processing is given in the figure on the left (Fig. 41). The first plot on top shows the raw data, but with the intensities of detectors five and seven already added up. This is done for a better comparability between plots, as the side detectors (5 and 7) already detect mostly SF intensity. A plot of this scan where the intensities are shown for each individual detector is shown in Fig. 79 in the appendix. Information about the experiment this scan belongs to can be found section 5.5.2.

The middle plot shows the data after background removal, as described in section 5.2.2 “Background determination”.

The major changes between these two plots illustrate how important a careful background reduction is for the analysis of polarization analysis raw data.

The third plot shows the after the detector counts have been transformed into SF/NSF intensities. There are only small changes compared to the background corrected intensities. The reason for these is that some of the neutrons reaching detector six underwent a spin flip. As this is taken into account by equations (118) and (119) NSF intensity is somewhat lower than the raw counts from detector 6.

Note that there is one NSF point, at 15meV, which has a negative intensity. This is because after background correction detector six had zero counts for this energy value. So the NSF intensity for 15 meV can be considered to be equally zero.

If one now adds error bars and plots the average of each two neighboring data points to smooth the data we arrive at the final plot for this scan, shown in Fig. 62. Compared to the background reduction step calculating SF/NSF intensities introduced only small changes to the plot. Nevertheless this is an extremely important step for the correct interpretation of our raw data.

5.3 Vanadium

Now, after we understand the basis of our setup as well as the used components and knowing how to process our data we can take a look at our test experiments. The first one was a measurement of Vanadium to see if our measured ratio between SF and NSF intensities matches the well-known behavior of a Vanadium sample.

Vanadium produces pure incoherent neutron scattering. Incoherent scattering of a polarized neutron beam from a pure Vanadium sample consist of 2/3 spin-flip and 1/3 non-spin-flip events, see [20]. Vanadium scatters neutrons in nearly pure incoherent fashion with a NSF cross section of $\frac{d\sigma}{\mathrm{d}\Omega}|_{++} = \frac{d\sigma}{\mathrm{d}\Omega}|_{--} = \frac{1}{3}B^2I(I+1)$ and a SF cross section of $\frac{d\sigma}{\mathrm{d}\Omega}|_{+-} = \frac{d\sigma}{\mathrm{d}\Omega}|_{-+} = \frac{2}{3}B^2I(I+1)$. Our ^{3}He cell gives us an incoming beam with a polarization of P_0 providing us with a spin-up and spin-down flux described by

$$\Phi_0^{\uparrow} = \frac{1+P_0}{2}\Phi_0^{\text{total}} \quad \text{and} \quad \Phi_0^{\downarrow} = \frac{1-P_0}{2}\Phi_0^{\text{total}} \tag{126}$$

(ϕ_o^{total} being the total incident flux).

After the sample, the now scattered beam can be described by:

$$S^{\uparrow} \propto \frac{1}{3}\Phi_0^{\uparrow} + \frac{2}{3}\Phi_0^{\downarrow} = \frac{3-P_0}{6}\Phi_0^{\text{total}} \quad \text{and} \quad S^{\downarrow} \propto \frac{2}{3}\Phi_0^{\uparrow} + \frac{1}{3}\Phi_0^{\downarrow} = \frac{3+P_0}{6}\Phi_0^{\text{total}} \tag{127}$$

and the polarization of it as:

$$P_S = \frac{S^{\uparrow} - S^{\downarrow}}{S^{\uparrow} + S^{\downarrow}} = -\frac{P_0}{3} \tag{128}$$

In our three detectors we observed count rates of I_5=239, I_6=1637 and I_7=1434 during a test measurement of a Vanadium sample. Using the calibration relation (112) we get a P_S=-0.28 which is in good agreement with the known polarization of our incident beam. At the time of this measurement the ^{3}He-filter provided P_0=0.85

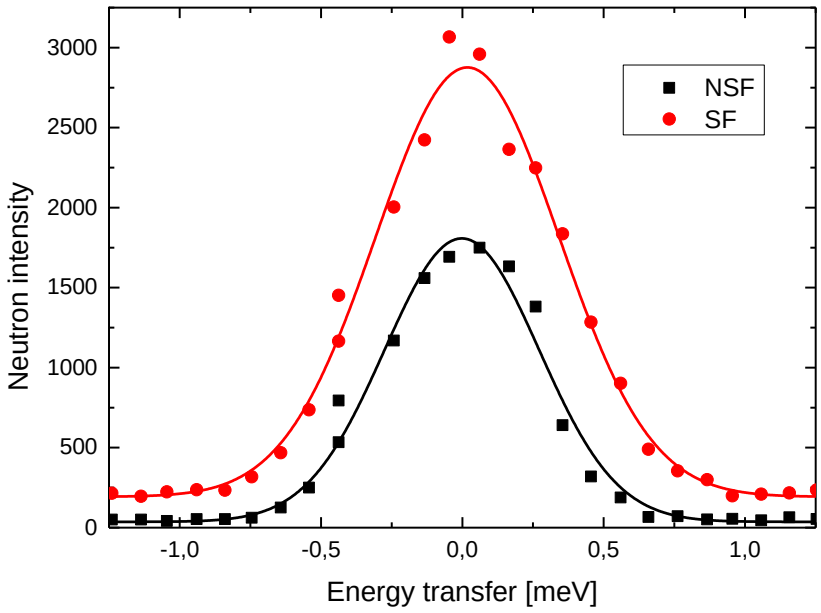

Fig. 42: Vanadium energy spectra showing incoherent spin-flip (SF) and non-spin-flip (NSF) scattering

5.4 Hematite

To further test our setup and to see if we could discriminate between nuclear and magnetic features some measurements on α-Fe_2O_3 (hematite) where done. The sample used was provided by Dr V. Hutanu[11].

α- Hematite is a system of space group $R\bar{3}c$, with lattice parameters a=6.005, b=6.005, c=13.67, α=90°, β=90°, and γ=120°. Mosaicity of the sample was 0.22°.

Under ambient conditions, Fe_2O_3 (hematite) shows an antiferromagnetic structure with spins oriented perpendicular to the trigonal axis characterized by magnetic super-lattice reflections of the type (0 0 3*l*) with *l* odd [21]. As the crystal consists of several antiferromagnetic domains, a neutron beam polarized perpendicular to the scattering plane is expected to become depolarized by the reflection at (003). In contrast, the pure nuclear reflection (006) will leave the beam unchanged. This gives us the option to test if we can detect a magnetic signal under ambient conditions. The used ^{3}He-cell was roughly one day old and hat a very high polarization and pressure (*p*=2,35 bar P_{He}=82,0%, resulting in a starting P_0=0,9995). One can clearly see the non-optimized setup and polarization in the PSD measurements shown in Fig. 43. The not yet optimized setup shows in the very small secondary side peak in the (003) scans, and the polarization problems of our incident beam in the (006) scans. As shown in sub-chapter 3.6 about our flippers they have a very high flipping ratio, so the remaining neutrons in the central channel of the (006) flipper on scan show that several days after installing the ^{3}He-cell the beam was still highly, but not fully, polarized. As the He-polarization was very high, and the cell was under large pressure we would have expected the central beam to vanish. The reason for the lower than expected beam polarization is the less than optimal improvised guide field around the sample before

we installed our quasi-Helmholtz field (see section 3.4) and probably also not optimal handling of the cell itself. The low intensity can be explained by the almost black ^{3}He cell, as well as not optimally chosen deflector angles and generally non-optimized instrumental setup. In addition peak count rates where determined for the three analyzer channels using the PUMA polarization analysis setup. From this we determined the polarization of the scattered beam, the results being in good agreement with our expectations when considering the not optimized experimental conditions. The results are listed in Table 7.

[11] Dr. Hutanu from the RWTH Aachen is instrument scientist of POLI, a polarized hot neutron diffractometer neighboring PUMA

	(003)	(006)
$I_5 + I_7$	4335	2657
I_6	5629	26553
P_s	0.09	0.82

Table 7: Intensities and scattered beam polarization for the magnetic (003)-reflection and the nuclear (006)-reflection

Our data clearly shows that the beam scatter at the magnetic reflection is in fact almost completely depolarized and the 82% polarization of the nuclear Bragg peak reflects the polarization of the incident beam as given by the ^{3}He cell and the magnetic environment at this time.
Normally we would have repeated this experiment with the optimized setup to have better statistics and measurements more representative of our instrument. But a lot of beam-time was lost due to technical problems with our beam-line as well as the reactor itself. As this was a proof of principle experiment that already showed that our setup was working it was decided to not invest more time into this sample.

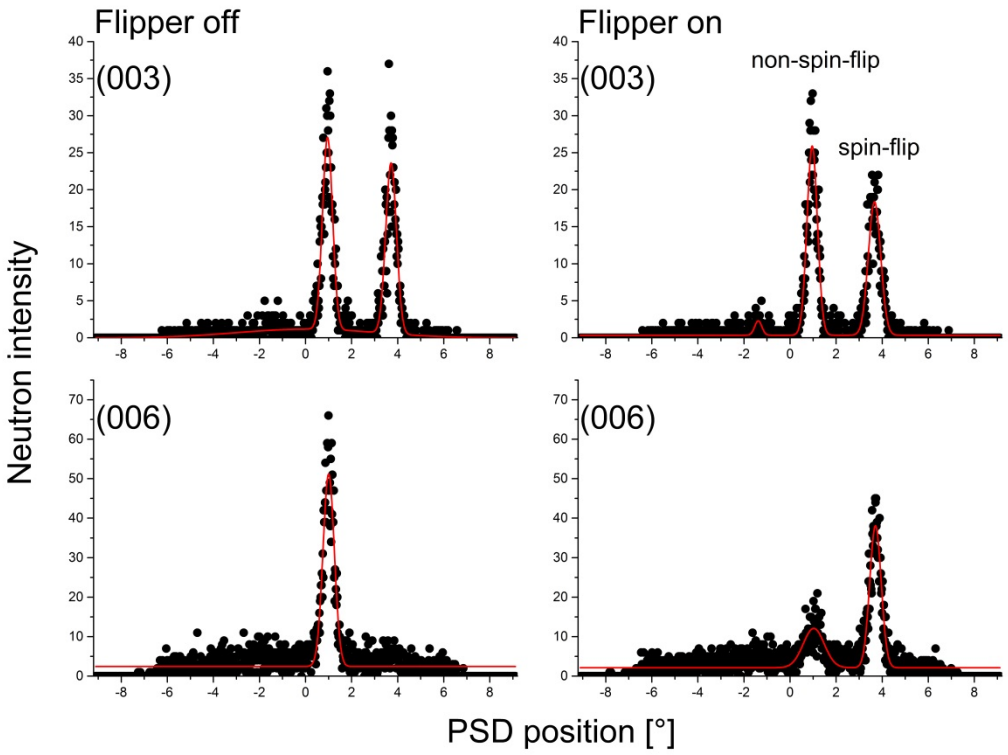

Fig. 43: First test experiment on Hematite using PSD and flipper for prove-of-concept. Upper row is the magnetic (003)-reflection; lower the nuclear (006)-reflection. Left-hand side shows the undisturbed signal and right-hand side the effect of the flipper.

5.5 Copper (II) oxide

After the proof of principle measurements ended on Vanadium and Hematite our next experiments where done with a Copper(II) oxide (CuO) sample. As another, well known, substance it was first intended as a final test measurement. But even so, as we will show, much new information could be found by probing CuO with our method.

CuO as a system started to get attention during the 1980-90s as a model substance to achieve better understanding of high temperature superconductors. This research avenue seemed to come to an end with the turn of the millennium. But in the last few years CuO again became a model substance, this time for high temperature multiferroic systems.

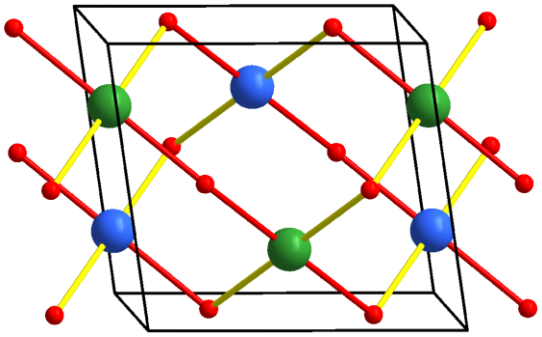

Fig. 44: Crystal structure of CuO, red spheres represent O positions, while blue/green indicate Cu (y=0.25/0.75)

CuO is a compound within the monoclinic space group C2/c with lattice parameters of a=4.6927(4) Å, b=3.4283(4) Å, c=5.1370(5) Å and a monoclinic angle of β=99.546(9) ° at room temperature [22]. A sketch of the crystal structure is shown in Fig. 44. It has three antiferromagnetic phases [23]. The most interesting feature is that it is also multiferroic. Multiferroic means that that a material shows two or more ferroic properties. This mostly means ferroelectricity and ferromagnetism, but can also include ferroelasticity or other ferroic properties. CuO is a system with three anti-ferromagnetic phases, at rather high temperatures. This makes CuO an interesting sample for understanding multiferroics and a possible intermediate step towards materials with multiferroic behavior under ambient conditions. In the low temperature AF1 phase, below T_{N1} =213 K, spins are oriented parallel or antiparallel to the monoclinic *b*-axis of the crystal. The AF1 phase shows a commensurate modulation of q_C=(0.5 0 -0.5)In the AF2 phase, between T_{N1} and T_{N2}≈ 230 K we have a somewhat more complex spin arrangement, forming a cycloidal order where the spins lie in a plane. The AF2 phase is also the phase showing multiferroic properties at an unusually high temperature for such

phenomena [24].Here we have an incommensurate modulation of q_{IC}=(0.506 0 -0.483) along which an additional spin component appears giving rise to the incommensurate helimagnetic structure. The cycloidal is formed by a slight phase shift between each Cu atom which leads to rotation like behavior. A sketch of the AF1 and AF2 magnetic arrangement is shown in Fig. 45, with an additional illustration of the cycloidal structure in Fig. 46.

The AF3 phase has a very narrow temperature range, smaller than one degree and located around 230 K. It should also be an incommensurable phase with a sinusoidal structure in direction of the b-axis, but its magnetic structure has yet to be determined. In this work the AF3 phase was not observed, but for a future experiment using this sample and setup, locating it and getting some confirmation of its magnetic structure should be possible.

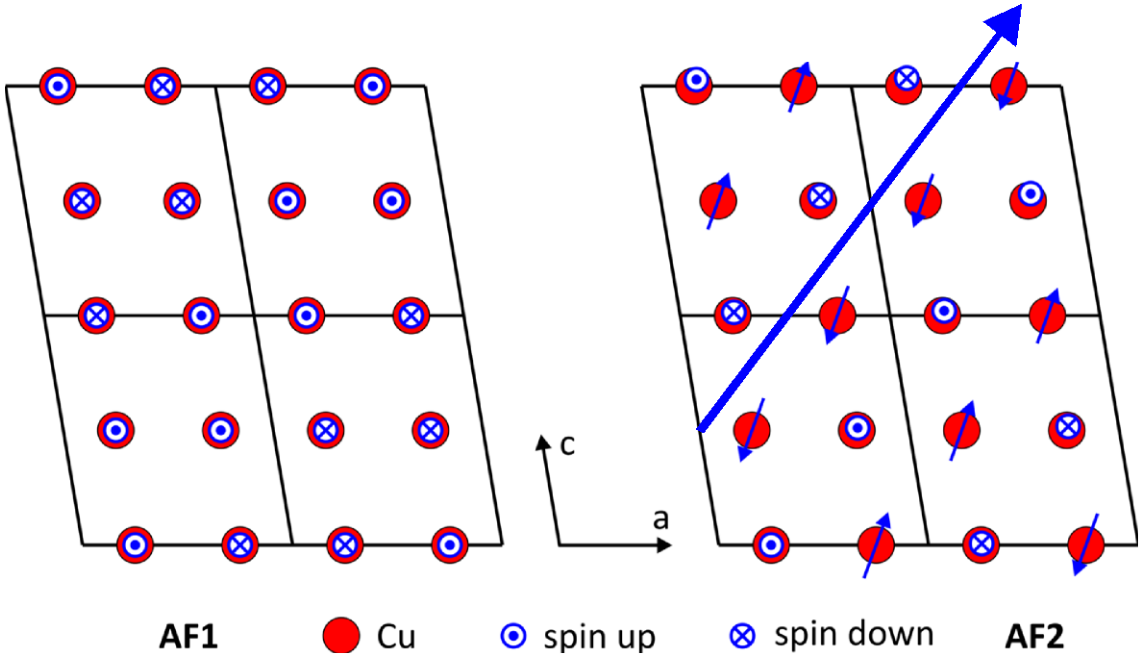

Fig. 45: Sketch of the magnetic structure of CuO in the a-c-plane. On the left the AF1 and on the right AF2 phase are shown. The increased de-centering of the spin up/down dots indicates the cycloidal direction (along the blue arrow).

As this work is mostly concerned with the development and installation of the polarization analysis at PUMA there is less of a focus on the scientific samples. A more detailed look at most of the measurements and findings on copper oxide, as well as a detailed overview of multiferroics can be found in the PhD thesis of Fabian Ziegler[12]. His work and the work at hand are closely interwoven with the present thesis having a stronger focus on the experimental development and implementation.

An exception for this split between our focus on the experimental method and setup and his focus on a more detailed look at the science of multiferroic CuO where some measurements taken after Fabian finished his work, these will be remarked on in the following text.

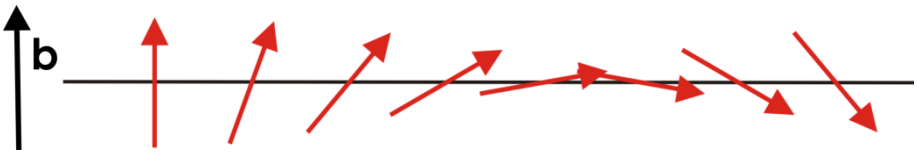

Fig. 46: Sketch of the spin cycloidal in the AF2 phase, giving a side view of the spin direction along the blue arrow in **Fig. 45**

[12] "Investigation of the Structure and Dynamics of Multiferroic Systems by Inelastic Neutron Scattering and Complementary Methods"
Göttingen 2018

The goal of our CuO experiments was measuring the magnon spectra of CuO in the multiferroic AF2 phase, as most prior inelastic neutron measurements where done either in the AF1 phase or in the paramagnetic phase. In addition some magnon spectra in the AF1 phase where measured to compare the two phases, showing that our system can easily distinguish between their magnetic structures.
In addition to this we searched for a known electromagnon located in the AF2 phase at 3 meV, as well as for one predicted at 13.5 meV, see [25, 26]. As electromagnons are excitations with phonoic and magnetic characteristics our setup should be a very good tool for investigation.

5.5.1 Sample preparation

Our sample of CuO was a rather large crystal grown by MaTecK[13] with an original length of ca. 3 cm and a diameter of 8-10 mm.
Some grid pattern γ-ray measurements of the crystal were done to assert its quality. These scans are shown in Fig. 47, where x is the position where the beam hits the sample and ω the rotation angle of the sample. After the CuO was placed in the beam a series of rocking scans was done to create a map of the whole sample. As shown by the upper row in Fig. 47 the crystal contained several smaller grains, luckily mostly located in the cylindrical part of the sample. This gave the CuO sample an effective mosaicity larger than 1°. In order to improve the mosaicity of our sample we made a cut as shown in Fig. 48, discarding the cylindrical part for our experiments. A diamond wire saw was used for cutting. The resulting, more or less, wedge shaped crystal, showed an improved effective mosaicity of roughly 0.5°. This was established by the gamma diffraction data shown in the lower row of Fig. 47. The sample resulting from this cut can still be considered rather large with a length of 15 mm, a sketch of the cut is shown in Fig. 48.

[13] MaTeck is a supplier of research materials specialized in single crystals located in Juelich https://mateck.com/

Photos of the sample before and after the cut are in the appendix as Fig. 77.

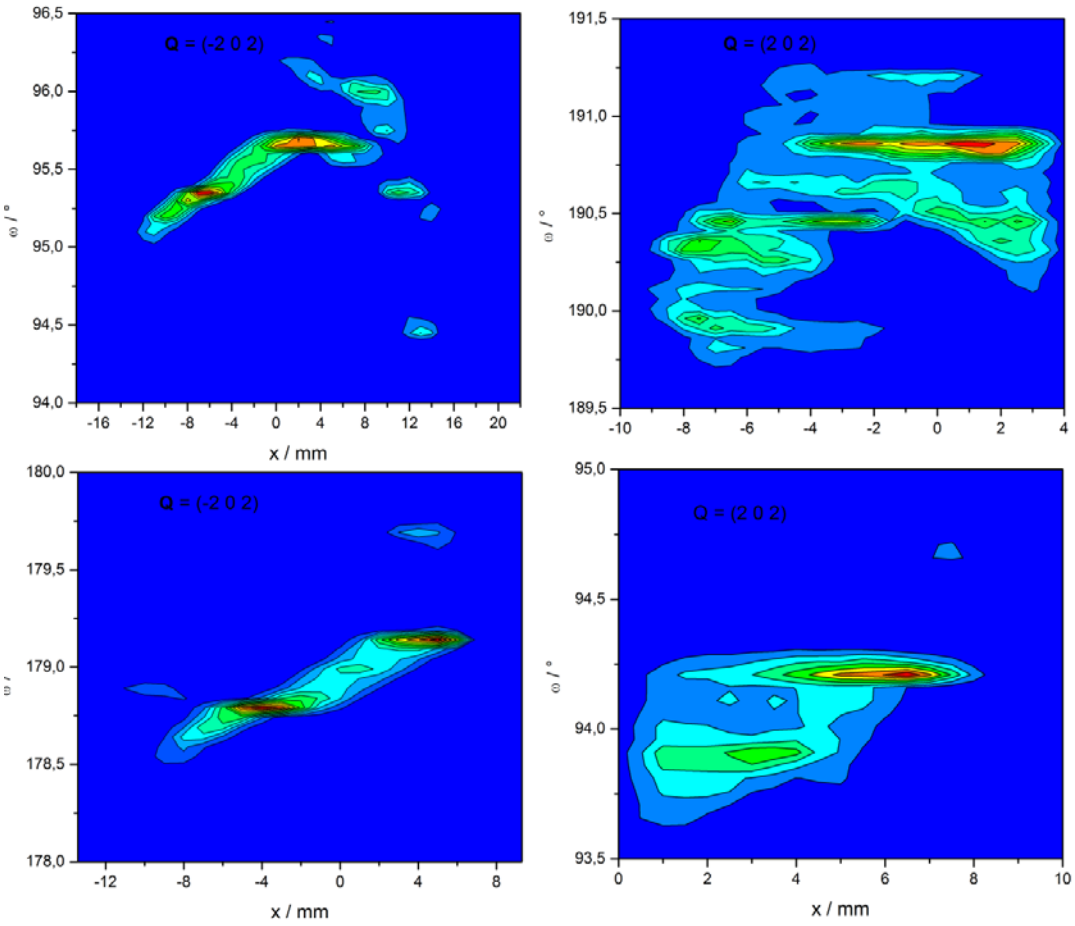

Fig. 47: Gamma-diffraction contour maps of our CuO sample. Top plots are before, bottom plots after cutting the crystal, showing that the cut part consisted of an accumulation of crystal grains

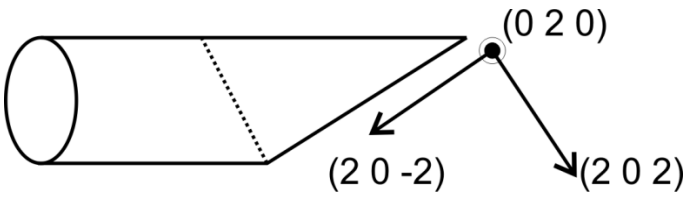

Fig. 48: Sketch of our CuO crystal with orientation. Total length is 30mm, with an 8mm diameter. Dotted line indicates the cut after γ-diffraction examination of the sample

For our neutron experiments the crystal was mounted on a standard aluminum sample stick using an aluminum angle to get a proper orientation of the sample.

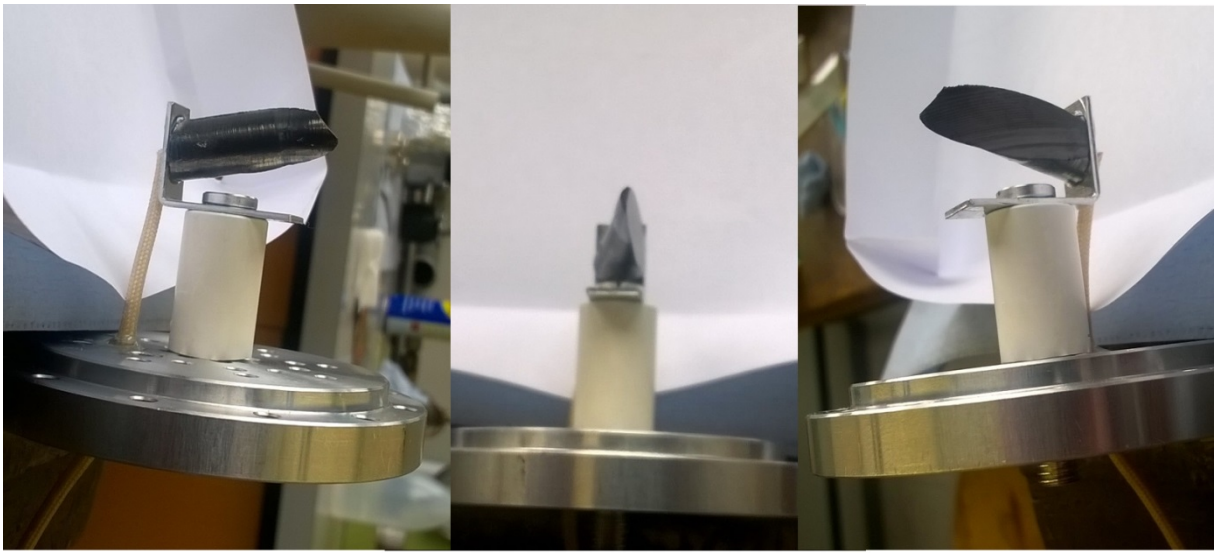

Fig. 49: Final setup of our CuO sample. The sample is glued with its (2 0 -2) plane to the sample holder, facing us in the central photo. In the right photo we look onto the (2 0 2) plane.

An additional temperature sensor, a Pt-100 thermometer, was glued on the Al angle bracket holding the sample to get a more direct measurement of the sample temperature. Cold head temperature in the normal PUMA cryostat setup is controlled by a Si-diode thermometer located directly at the cold head of the cryostat. To minimize neutron scattering from Aluminum the sample stick was shielded by a boron nitrate casing. A photo of the final sample configuration is shown in Fig. 49.
The sample was then enclosed in an Al sample can, filled with He-gas and sealed with indium wire for the improvement of thermal homogeneity.
The sensor located at the cold head is fine for regulating cold head temperature but we expected a strong temperature gradient between the sensor position and our sample. Our additional temperature sensor showed how much the temperature of the sample was lagging behind the temperature measured at the cold head.
One reason for this long thermal equalization time was that in our first CuO measurement the sample was mounted in a “standing up” position. Because of this the only thermal contact between the cold head on top and the sample was through the He gas and the very thin Aluminum walls of the sample can. Additionally the can was not completely gas tight and lost the Helium over time so that only the can walls remained.
To improve the thermal conductivity during our following measurements the sample was mounted hanging down from the cold head. This slightly increased the risk of the sample falling down during

the experiment, but gave us much better thermal contact between sample and cold head via the sample stick.

5.5.2 Elastic measurements on CuO

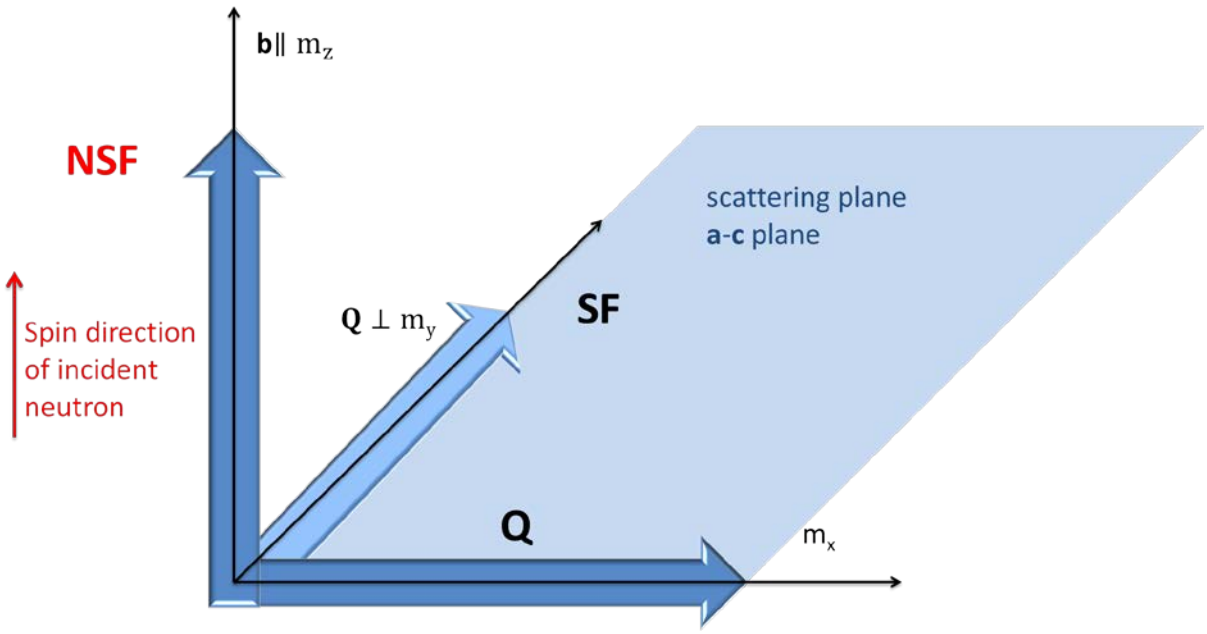

Fig. 50: Sketch of the CuO scattering setup. The scattering plane in this case is identical with the crystallographic a-c plane. Neutron spin direction is parallel to z, and ***Q*** parallel to y. Non-spin-flip scattering occurs when magnetization perpendicular to the a-c-plane/parallel to b is probed. Spin-flip scattering occurs when magnetization is perpendicular to ***Q***, so when it is oriented in the scattering plane.

For the PUMA polarization analysis setup we have a neutron beam polarized in **z**-direction giving **z**- and **–z**-polarization. Two different spin contributions can be detected with the system, SF and NSF. The measured intensities correspond to $I_{SF} \propto |m_y|^2$ and $I_{NSF} \propto |m_z|^2$. This connects the magnetic scattering selection rules from Table 4 with our experimental setup.

For our experiment, the ***a**-c****-plane was chosen as scattering plane because the satellite reflections we are interested in have only a- and c-components. As provided by the setup vertically polarized neutrons where used. A sketch of the magnetic scattering setup and selection rules for the experiment is shown in Fig. 50. Magnetic moments perpendicular to the scattering plane are, in this way, parallel to the incident neutrons and to the incident neutron spin direction. From the selection rules (section 4.3) we know that NSF intensity is the result of magnetization perpendicular to the scattering plane. Magnetic moments parallel to the scattering plane and perpendicular to ***Q*** will

result in SF intensity. As all three antiferromagnetic phases of CuO have spin components parallel to the **b** direction, but only the AF2 phase shows magnetization inside the **a**-**c**-plane. Therefore elastic SF scattering can be used as a probe for the AF2 phase.

This can be illustrated by the temperature scan shown in Fig. 51. We scanned over the commensurate and incommensurate satellite reflection while varying temperature. This was done to locate the phase transitions and calibrate the temperature sensor but is also useful to show the emergence of difference in scattering behavior for the AF1 and AF2 phase.

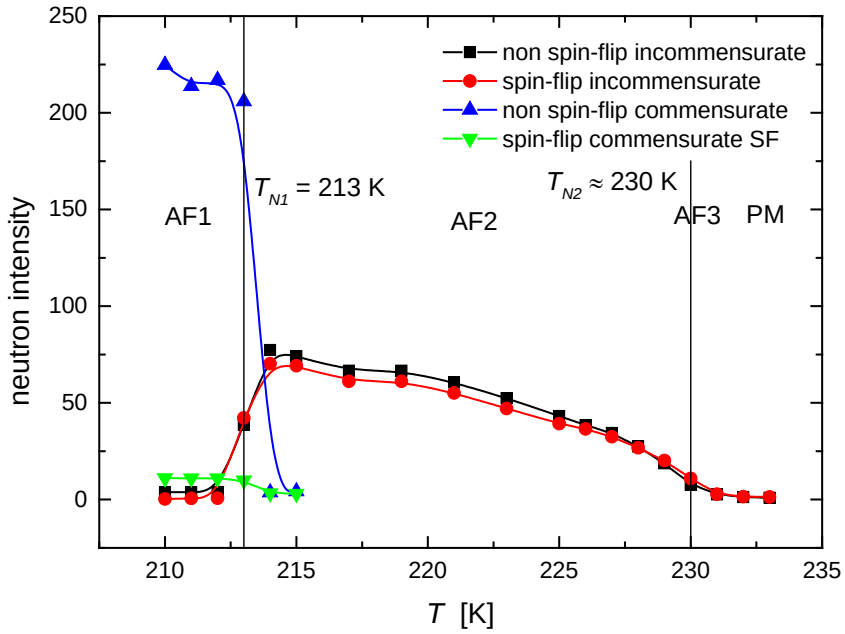

Fig. 51: Temperature variation of the satellite intensities of CuO for spinflip and non spinflip channels. Lines are drawn to guide the eye. (Please note, that the data represent raw intensities that are not corrected for a non-ideal polarization of the incoming neutron beam.)

Within the commensurate phase (AF1), the magnetic moments of the copper ions are either parallel or antiparallel to the neutron spin. Hence, superlattice reflections within the scattering plane do not contain any SF contribution and the neutron beam remains polarized as shown in Fig. 51. This is in clear contrast to the behavior of the incommensurate satellite observed for temperatures between T_{N1} *and* T_{N2}: In the AF2 phase we have additional magnetic contributions depending on the scattering geometry.

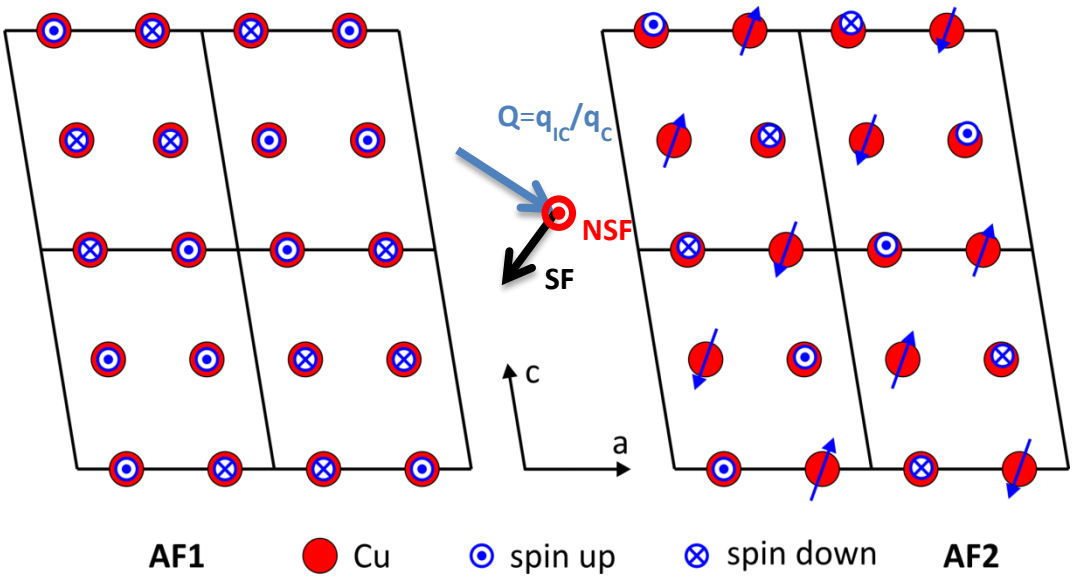

Fig. 52: Orientation of the scattering vector **Q** relative to the magnetic structure for the elastic measurements

A sketch of our scattering geometry is shown in Fig. 52. In the AF2 phase at $\boldsymbol{Q} = \boldsymbol{q}_{IC}$, the scattering vector is almost perpendicular to the plane of the rotating spins and the scattered beam becomes completely depolarized as NSF- and SF-scattering interact with the magnetization of the spin helix. The spin helix is nearly circular according to [24]. Consequently, as our $\boldsymbol{Q}$ is nearly perpendicular to the rather perfect circular structure the intensities for the SF and NSF channels are almost identical. SF intensity is a little bit lower than NSF intensity as the angle between scattering plane and $\boldsymbol{Q}$ is not exactly 90°.

We also see coexisting of both AF1 and AF2 phases around T_{N1} during the phase transition. As the scans were done with 1 K temperature steps we assume that none of our scans found the AF3 phase, which is expected to be smaller than 1 K.

5.5.3 Inelastic measurements on CuO

In addition to these elastic measurements some inelastic experiments on CuO using polarized neutrons with the new PUMA polarization setup where executed. In early experiments, Ain et al. and Yang et al. have investigated the magnon dispersion of the commensurate phase and found a steep branch that can hardly be resolved by inelastic neutron scattering at energies below 10 meV [27, 28]. Rather, resolution effects lead to the observation of an intensity maximum centered at the superlattice reflections that becomes broader and broader in q with increasing energy. Jacobsen et al. did some similar measurements published in [29]. In the last measurement of this work in September 2018 we replicated some scans from this paper. The results of both works are in agreement, but we have better resolution data, as well as the intrinsic bonus of our method, simultaneous detection of both spin states and additional low energy data.

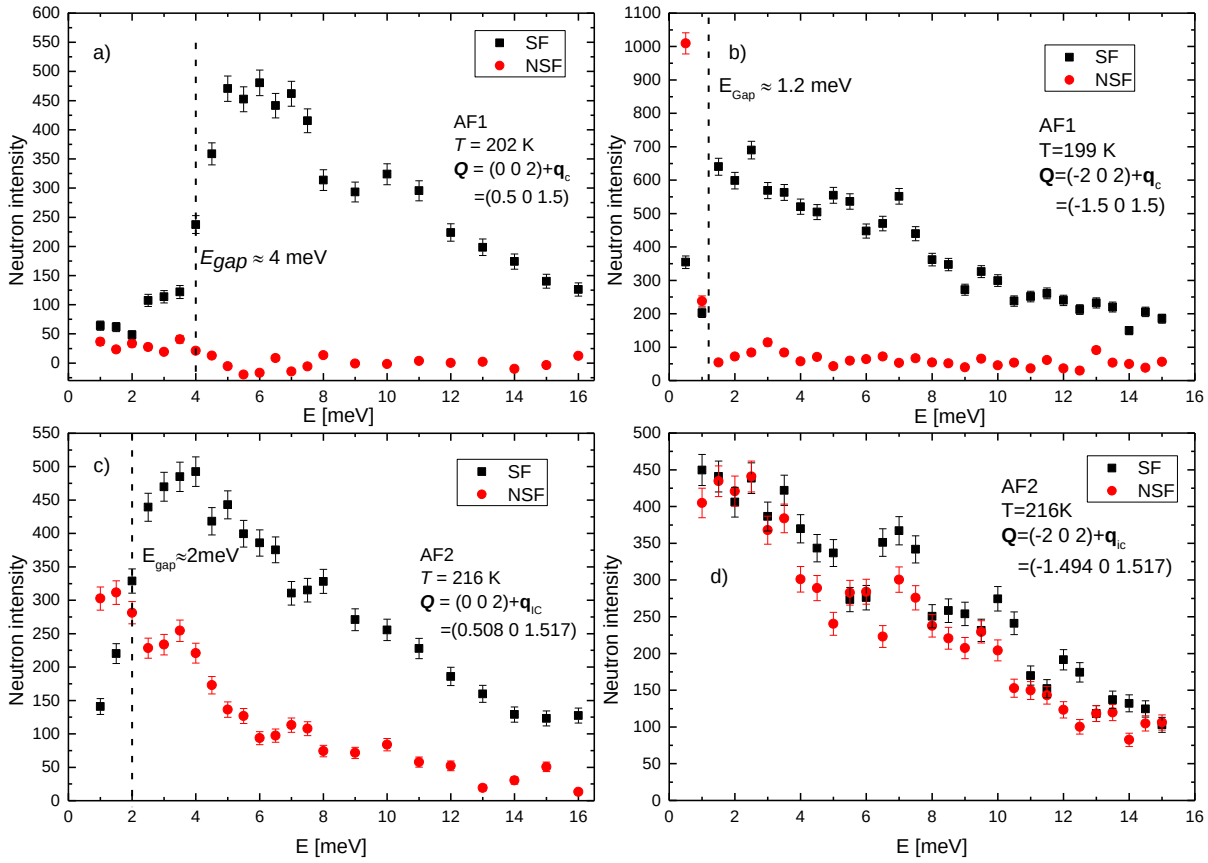

Fig. 53: Energy scans at the satellite position in different zones. Left in (0 0 2), right in (-2 0 2). Both are measured in the commensurate phase (top row) and the incommensurate phase (bottom row). Plotted is non-spinflip (red) and spinflip (black) scattering. These spectra are corrected for background and for the finite polarization of the incident beam according to equations (118) and (119).

The left hand side of Fig. 53, a) and c), displays energy spectra taken at the magnetic zone center at (002)+$\boldsymbol{q}_{IC,C}$. In this Brillouin zone, the scattering vector $\boldsymbol{Q}$ is almost perpendicular to the propagation vector $\boldsymbol{q}_{IC,C}$ and, hence, only magnetic excitations are observed that exhibit components parallel to $\boldsymbol{b}$ or $\boldsymbol{q}_{IC,C}$. NSF intensity in Fig. 53 a) reaches only background level as all spins in the AF1 phase are oriented parallel or antiparallel to $\boldsymbol{b}$, the same as our neutron polarization. Because of this the spins can only be excited inside the scattering plane and we can only detect SF intensities in the AF1 phase. The NSF intensity in scan Fig. 53 c) can be illustrated by the sketch in Fig. 54 b), while the SF intensity is a result of the cone mode shown in Fig. 54 c) (on the right).

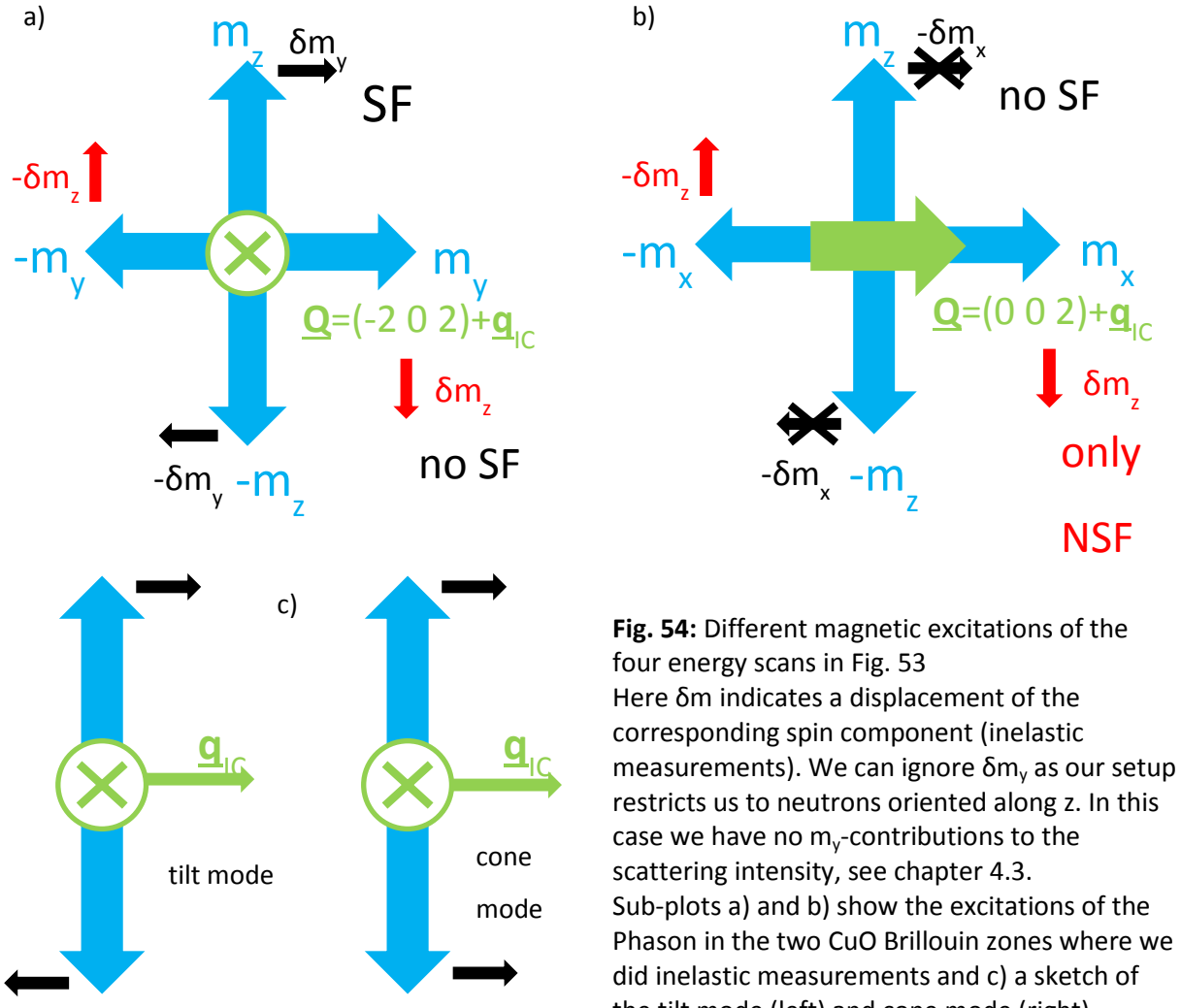

Fig. 54: Different magnetic excitations of the four energy scans in Fig. 53
Here δm indicates a displacement of the corresponding spin component (inelastic measurements). We can ignore δm_y as our setup restricts us to neutrons oriented along z. In this case we have no m_y-contributions to the scattering intensity, see chapter 4.3.
Sub-plots a) and b) show the excitations of the Phason in the two CuO Brillouin zones where we did inelastic measurements and c) a sketch of the tilt mode (left) and cone mode (right) excitation

Looking at the two (0 0 2) scans in Fig. 53 one in the commensurate phase at 202 K, a), and the other in the incommensurate phase at 216 K, c), the two phases show significantly different behavior. In the commensurate phase we observe only spin-flip scattering, with very low intensity for energies

lower than 4 meV. At this energy we observe a steep increase in intensity which merges into a continuous decrease for energies above 7 meV. This is consistent with the known steep magnon branch. This spin gap of 4 meV was not observed prior to this experiment.

In the commensurate phase (Fig. 53 a) we observe SF intensity because the magnetic moments are oriented parallel to the **b**-axis of the system. Therefore they can only be displaced in the a*-c* plane giving us SF scattering.

From the incommensurate phase (Fig. 53 c) we get a different behavior. What we observe is a smaller spin gap of 2 meV for SF intensity, as well as the occurrence of NSF intensities at lower energies. This is due to the existence of a spin spiral with components along ***b*** and ***Q***, giving us two different magnon modes. First a displacement within the spin spiral plane (***b***-***Q*** plane) in the form of a phason mode. This one cannot change the neutron spin, resulting in NSF scattering. This is sketched in Fig. 54 b) where we see ***Q*** parallel to m_x (m_x= component of magnetization along x-axis). This leads to displacement of m_z (perpendicular) producing NSF intensity and no displacement along m_x so that we get no intensity in the SF channel.

The second mode is the result of displacements perpendicular to the ***b***-***Q*** plane. This is almost parallel to $\boldsymbol{q}_{IC}$ and results in a SF behavior very similar to the commensurate phase with a (smaller) spin gap an intensity maximum around 4 meV and a decrease in intensity towards higher energies. The picture of a tilting mode distorting spins orthogonal to the cycloidal plane and thus producing SF scattering may give the right idea for this mode. A sketch of the tilting (left) and cone mode (right) is shown in Fig. 54 c)

SF scattering in both phases has a strong resemblance with each other, with the exception that the spin gap of the tilt mode in the incommensurate phase is reduced by a factor of 2.

The phason mode is shown to exist by the occurrence of NSF scattering. The phason also shows indications for a steep dispersion. In contrast to the SF mode no spin gap is observed, only a continuous increase in intensity towards lower energies.

In the (-2 0 2) zone the commensurate scan (Fig. 53 b)) looks very similar to the (0 0 2) scan in the same phase, but with a considerably smaller gap of only around 1.2 meV.

For the incommensurate phase in the (-2 0 2) zone (Fig. 53 d)) we observe no spin gap in SF and NSF channels. Here *Q* is perpendicular to the cycloidal plane so intensity in both channels can be explained by a spin displacement inside the plane. See Fig. 54 a); ***Q*** is along the modulation direction and thus perpendicular to both m_y and m_z. As the spin helix is nearly perfectly circular this gives us intensity in both channels with equal intensities.

From this point forward the discussed experimental data is unique to this work as the measurements where done after Fabian Ziegler finished his thesis:

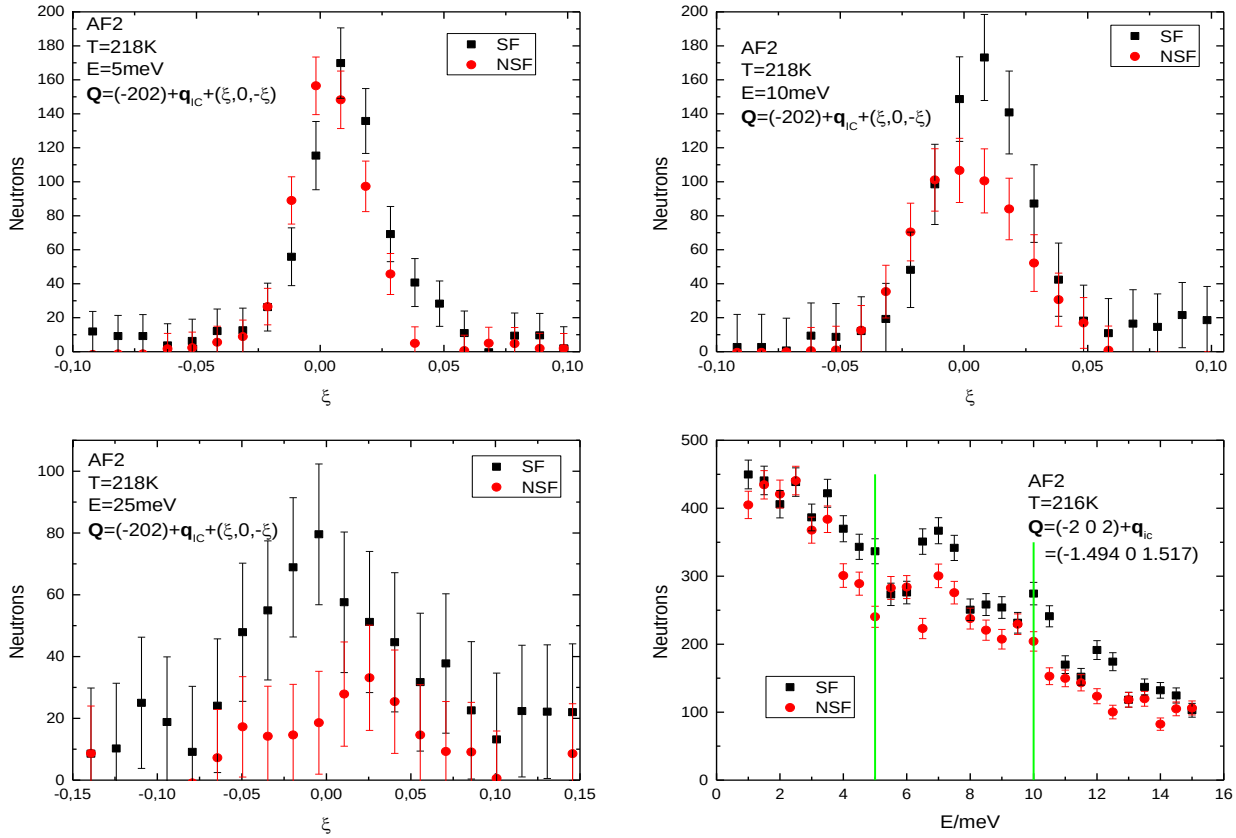

Fig. 55: Constant energy scans of the AF2 phase of copper-oxide in (-202) direction. Top row are 5 and 10meV scans with the final 25meV scan in the bottom row. Bottom right shows a constant q -can in the same Brillouin-zone and crystallographic direction. The green lines indicate the positions of the 5 and 10meV scans

The first data of these experiments we will discuss are the constant energy scans with ***Q***=(-2 0 2)+$\boldsymbol{q}_{IC}$+(ξ 0 -ξ) shown in Fig. 55 a-c). These three constant energy scans show a broadening of the signal as well as a growing drift in intensity between SF and NSF channels towards higher energies. The constant ***Q*** scan (Fig. 55 d) in the same phase and zone shows no significant difference between

SF and NSF scattering for low energies and only punctual differences between the channels. From the constant energy scans it appears that in the higher energy range NSF intensity is decreasing faster than SF intensity. While the constant ***Q*** scan indicates only small deviations between SF and NSF intensities for the probed energy range we already see a notable difference in SF/NSF intensity at 10 meV in the constant energy scan. This gets much more pronounced for the 25 meV scan. If the constant energy scans are carefully fitted (taking the rather low intensity into account) and the FWHM are plotted we also clearly see the mentioned broadening of the measured signals towards higher energies, see Fig. 56. Again the channels start to drift apart for energies higher than 5 meV.

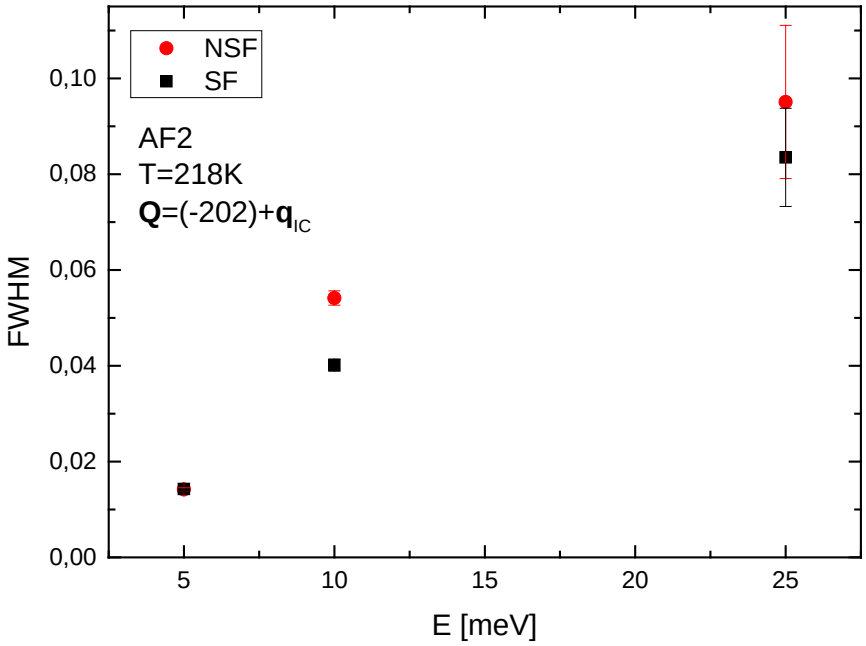

Fig. 56: FWHM plotted for the constant energy scans shown in Fig. 55. Broadening of the peaks towards higher energies can be explained by the steep dispersion of the measured magnon branch

This can be explained by the known steep dispersion of the measured magnon, see Ain et al [27]. The resolution ellipsoid of our setup cannot resolve the dispersion leading to broader signals for higher energies up to the point where the dispersion could be dissolved, but this energy range was outside the scope of this experiment.

We also made a series of constant energy scans in the (0 0 -2) zone of the AF2 phase. Scans were done for 2, 3, 4, 12, 13, 14, and 20 meV, see Fig. 57. These energies were chosen because there is a known electromagnon at 2.9 meV observed using THz spectroscopy, see Jones et al. [25], as well as a some theoretical hints for another one at 13.5 meV, see Cao et al. [26]. Electromagnons are excitations combining magnetic and phononic components.

As all of these polarized inelastic measurements in the second Brillouin-zone are scans right at the edge of the capabilities of PUMA a low intensity is to be expected.
But nevertheless these scans still exhibit some interesting features. Even with the increased counting errors it is interesting to note that in the 3 and 13 meV scans the SF and NSF signals have a greater difference in their intensity then in the other scans. Also, in both of them there are slight indications of emerging side peaks in the positive ξ direction.
As each detector produces a similar amount of noise and detector 5 only gets very little signal this is an interesting case to look at the influence of signal to noise for our setup. A comparison between using the signal from just detector 7 and from detector 7 and 5 is shown in Fig. 58. These are the two most extreme examples. For the 2 meV scan there is only a very small difference, SF intensity goes down as well as the SF error. The same is true for the 13 meV scan, showing the greatest difference for all considered scans. But even with reduced SF intensity the qualitative findings remain the same. We have more SF than NSF intensity, the NSF peak is broader and there are indications for an emerging side peak.
For lower intensities it would be recommended to analyze the data without detector 5, but here there is no difference in qualitative information from the scan and the increased noise is taken into account by the larger errors. For scans with higher statistics there is no benefit of excluding detector 5.

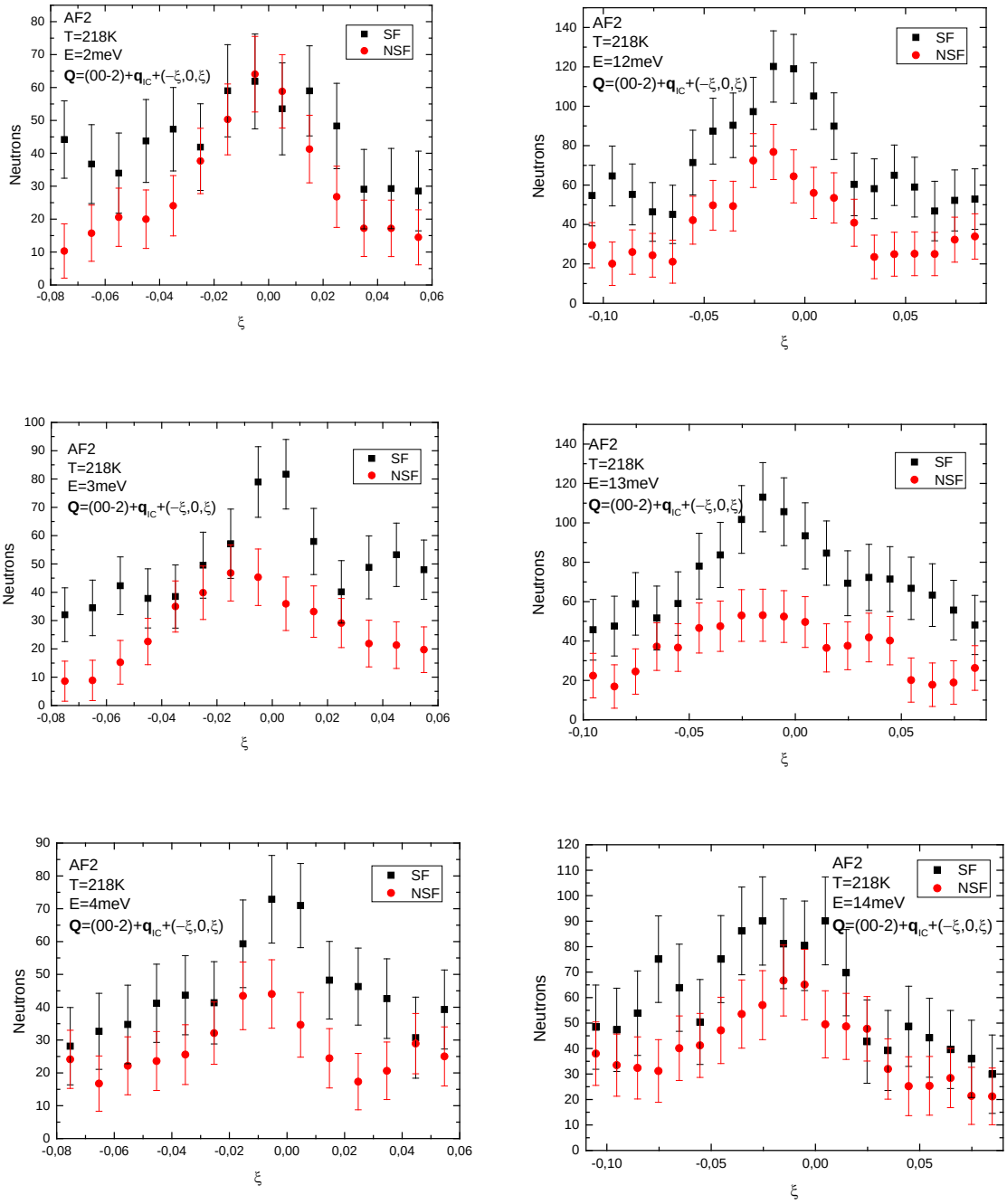

Fig. 57: Constant energy scans of the (0 0 -2) zone in the AF2 phase of copper oxide

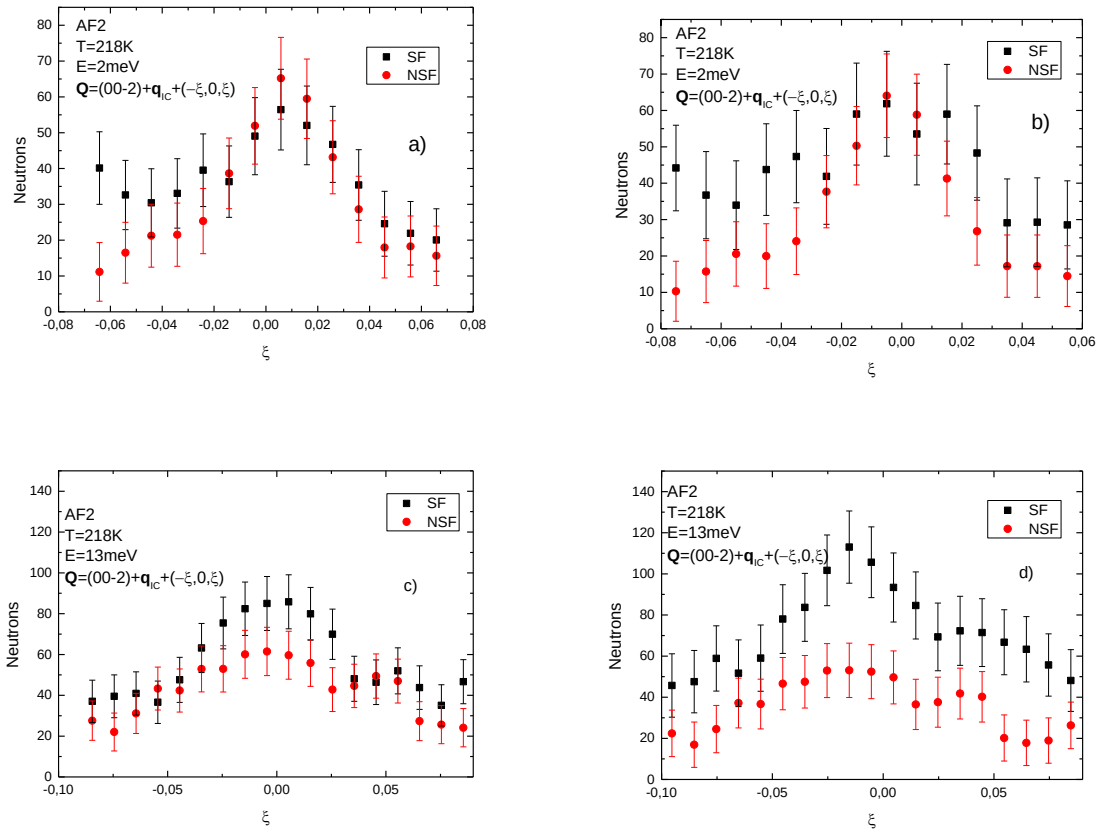

Fig. 58: Comparison of two constant energy scans, where a) and c) only take detectors 6 and 7 into account while b) and d) use all three component beams. For these scans ignoring detector 5 leads to lower noise (smaller error bars) and increases the share of NSF intensity.

All of the features get a bit clearer when looking at the FWHM of the peaks, shown in Fig. 59.

It is interesting to note that the scans around 3 and 13 meV behave in a mirrored way. First the 2meV scan shows broad signals, then the 3meV scan somewhat sharper peaks and finally the 4meV scan shows the sharpest peaks. This corresponds to sharp peaks at 12 meV, somewhat broader peaks at 13 meV and again a broad signal at 14 meV. So that the 2meV scan behaves like 14meV, 3meV like 13 meV and 4 meV like 12 meV.

In addition at 3/13 meV we see that the NSF signal is broader than the SF signal in contrast to the other scans.

As already shown in Fig. 57 the peaks generally broaden towards higher energies. There are also slight indications of a shoulder on the positive ξ of the 3 and 13 meV scans.

There is also a slight drift in peak position towards smaller ξ for higher energies, more prominent in the SF channel, see Fig. 60.

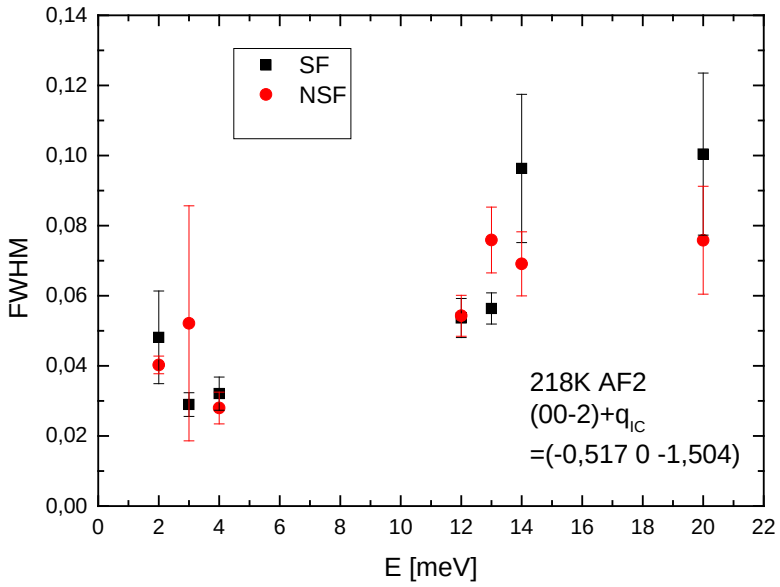

Fig. 59: FWHM of the peaks found in a series of constant energy scans in the AF2 phase of copper oxide

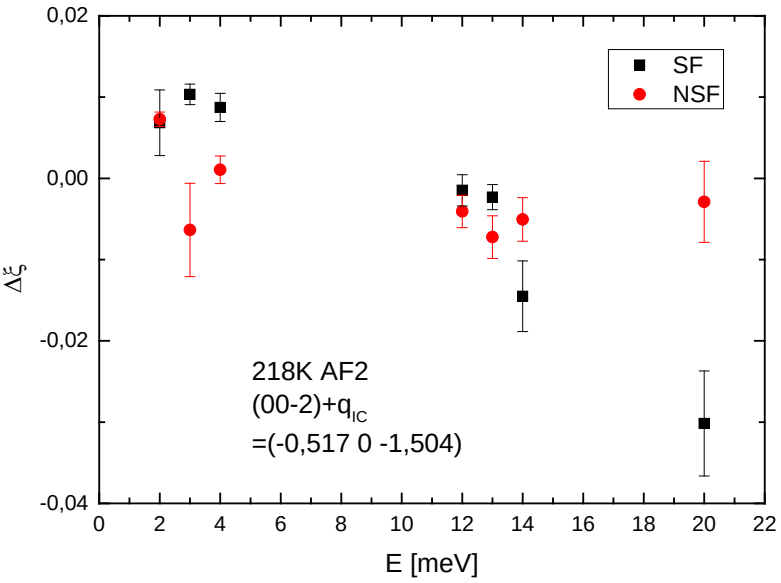

Fig. 60: Peak positon for (0 0 -2) AF2 scan. Shows a slight drift towards smaller ξ for higher energies

Just looking at our measured SF intensities of the 12 and 14 meV scans shows indication for splitting of the magnon branches in accord with Ain et al [27]. They give a slope of 550 meVÅ for the magnon dispersion. This gives us an expected splitting of 0.041 ξ at 12 meV and 0.048 ξ at 14 meV. We observe a splitting of $\Delta\xi = 0.038$ at 12 meV and at 14 meV we have$\Delta\xi = 0.031$, see Fig. 61. In Fig.

61 the 12, 13, 14 meV scans are shown with a multiple Gauss-fit to the SF intensity. The central peak is fitted in green with a single Gaussian for the 13 meV scan and two Gaussians for the 12 and 14 meV scans indicating a splitting of the magnon branches. Peak-position for these fits is indicated with green arrows.

As the data was carefully background corrected all of the measured intensity should be a real signal. Because of this the intensity next ot the central peak was fitted with two additional Gaussians (in blue). The complete multi-fit is shown in black, showing a good match to our data. However the possible branch splitting in the 12 meV scan should be taken with care as the statistics are rather weak. Furthermore the same is true for the 20 meV data. A fit showing a splitting of $\Delta\xi = 0.036$ can be achieved but is not fully convincing.

Splitting of the magnon branches in CuO has not been measured at such low energies before

In both the 12 and 14 meV scan we see hints of a broad shoulder on the high ξ side as well as asharper peak on the low ξ side of the magnon peak.

However, in our 13 meV scan there is no discernable magnon splitting, only a broader central peak. Also side features are more symmetric than in the energy scans directly above and below. This could be the result of phonon magnon interaction from the possible electromagnon at 13.5 meV, but with our data it is not possible to settle the form of this dispersion at this moment.

If these features in the 13 meV scan are the result of a phonon this may indicate a rather flat slope. It strongly depends on the slope of the phonon and its interaction with the resolution ellipsoid of our instrument.

But a conclusion for the nature of the electromagnon dispersion could not be made.

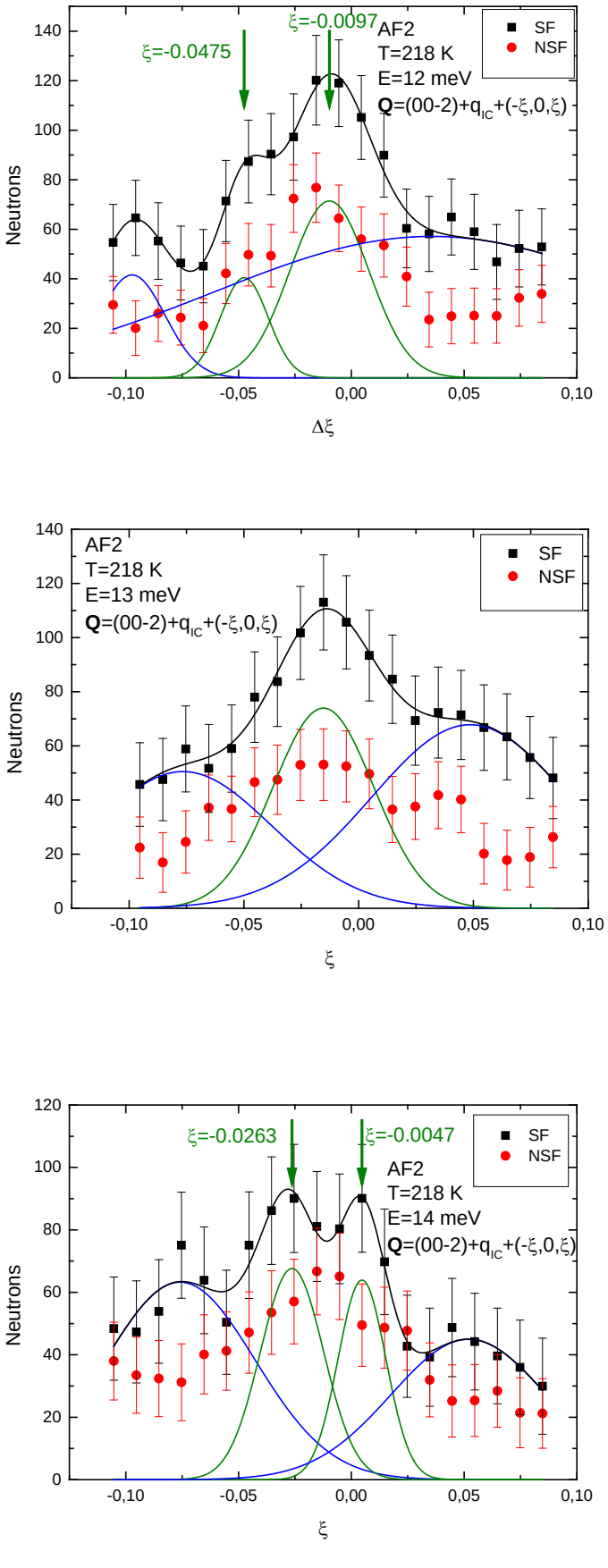

Fig. 61: 12,13 and 14 meV scans with Gauss fits to SF measurements.
The 12 and 14 meV scans show splitting of two steep magnon branches which is absent in the 13 meV scan.
All scans also show hints for additional features (blue fit curves) besides the central magnon peak (green fit curves)

As an electromagnon cannot be distinguished from a magnon by inelastic neutron scattering there is no proof that the signal around 13 meV is indeed one. But the symmetrical behavior (hints for a side peak in positive ξ direction and a NSF signal broader than the SF signal as opposed to all other energy scans) between the scans around the known electromagnon at 3 meV and the scans around 13 meV is a good indication that the proposed electromagnon at 13 meV really exists.
Overall the constant energy scans show hints at some interesting features and normally further experiments would be in order to get better statistics, scan over a wider *q*-range and more energy values. But due to technical problems at the reactor and external time constraints further, more conclusive, measurements are outside the scope of this work.

5.5.4 Low temperature scans

In addition to the 200 K (2 0 -2) scan we also did one with much lower temperatures to compare with a scan from a recent publication, Jacobsen et al. [29]. They did their neutron polarization analysis at the IN20 TAS located in Grenoble, measuring magnetic scattering at the AFM zone center in two directions, $\left(\frac{1}{2}\ 0\ \frac{3}{2}\right)$ and $\left(\frac{1}{2}\ 0\ \frac{1}{2}\right)$ at a temperature of 2K. An anisotropic spin gap was reported for both directions, as well as an asymmetric energy peak at 23 meV. The paper also presents a model to explain the observed features, explaining the 23 meV signal with the onset of a group of four degenerated optical modes and the anisotropy in the spin gap with splitting of the acoustic modes.

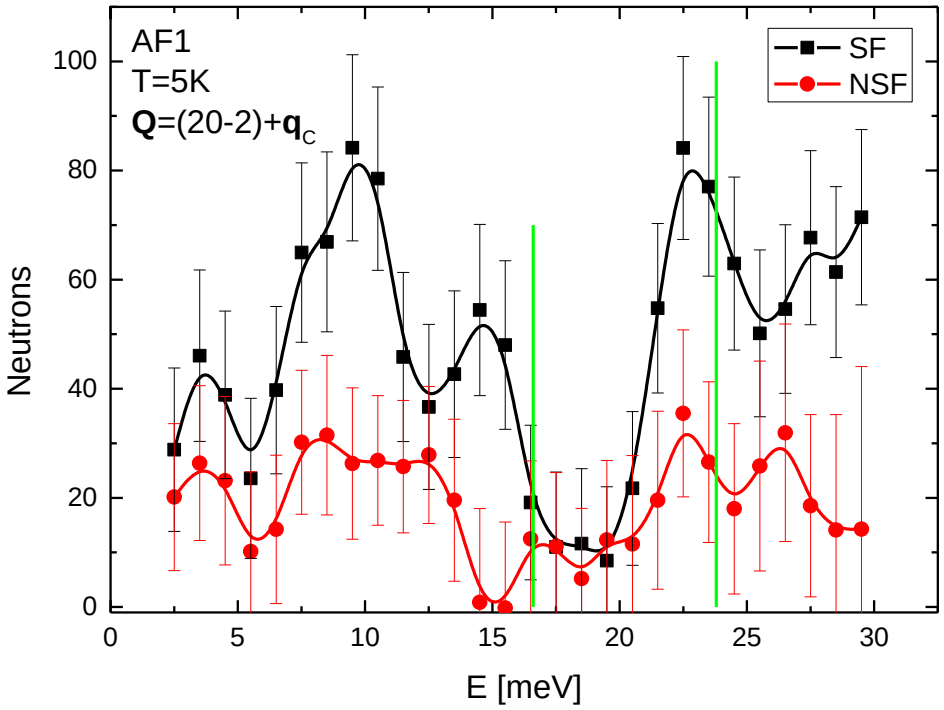

Fig. 62: Energy scan of the AF1 phase @5K from 2-30 meV. The green lines indicate the positon of the two lowest energy magnon modes calculated after the model form Gaw [30]. Red and black lines to guide the eye.

In comparison to Jacobsen et al. [29] FIG. 5 (b) we see considerably more details in our scan, see Fig. 62. We confirm the existence of a peak at 23 meV, but in addition to this we get a few more features. The most obvious it the strong intensity dip at 18 meV. Furthermore we see three peaks in the lower energy range at 4, 10 and 15 meV. The 15 meV peak in SF intensity correlates with a minimum in NSF intensity.

Our scan took roughly 10 hours, or 20 minutes per data point being on the boarder of feasibility for polarized inelastic neutron experiments.

The energy resolution for our scan lies between 0.96 meV at 2 meV energy transfer, over 1.66 meV for an energy transfer of 15 meV up to 2.9 meV for our highest scan point at 30 meV.

As the Jacobsen paper included a model for magnon dispersions we used this model to see if we could match it to our data. The magnon model form the Jacobsen paper gives around 50 meV for the lowest magnon branch, much higher than anything we observed. As this is not consistent with the fits shown in this publication we assume that there occurred a typo in writing down the model. In the publication the PhD thesis of Stephen M. Gaw [30] is cited for more details on the magnon dispersion

model. Model and calculated parameters differ from the paper, but this model produces two magnon branches with their lowest energies in **Q**=(1.5 0 1.5) direction. The calculated energies are 16.6 meV for the lower and 23.8 meV for the higher branch a factor of ~2 lower than what the Jacobsen model gives. Interestingly these energies are close to two of the peaks measured in our energy scan. Interestingly the Jacobsen paper also mentions that their model gives a good description of AF1 magnon spectrum, except for anisotropic signals at low energies where they expect a further splitting of the magnon modes. This could be a possible explanation for the additional signals we see below 15 meV, but to come to a conclusion a refined model should be fitted to our data. Unfortunately this was outside the scope of this work.

6 Conclusion and future investigation

The main goal of this work was the development and implementation of a polarization analysis setup with the unique feature of measuring both spin states simultaneously for PUMA.
This setup is now fully commissioned and in use. Test measurements and the first experiments also demonstrated that the method for simultaneously detecting both spin channels is working and a valuable asset for probing magnetic structures with neutrons.
Analytical calculations, McStas simulations and test experiments are in good agreement. This shows the fine grasp and control we have achieved with the PUMA polarization analysis. Furthermore our test measurements on Hematite and Vanadium showed that our method works as intended.
The measurements on CuO proved that this new technique can generate new information about magnetic excitations as several previously unknown magnon modes were observed. Measurements with polarized neutrons allowed us to make a detailed analysis of the different behavior of magnons in different magnetic phases and Brillouin zones. We observed two different excitations in the AF2 phase one of which might correspond to an already observed electromagnon. Also spin gaps in the spin-flip channel where observed for the first time. There were also measurements in the AF2 phase giving hints about a second electromagnon around 13 meV, as well as a low temperature energy scan in the AF1 phase showing more structures than previously known due to our better energy resolution.
These measurements showed us what can be done with the technique, and where its limits lay. For example for large samples a different polarization analysis instrument may prove to be a better fit if there is no interest in measuring SF and NSF intensities simultaneously.
The PUMA polarization analysis can half the time needed for a polarization experiment, as both spin channels are detected at the same time. This gain in intensity is true under certain conditions, such as for a sample with a diameter of 1 cm or less and a scattered beam with a divergence smaller than 30’. For differing conditions the gain in time will be less, up to the point where a conventional setup will be more efficient.
Furthermore the PUMA polarization analysis is uniquely suited for high resolution experiments or kinetic polarized neutron studies. The realization of a kinetic polarized neutron experiment should be among the most complex TAS experiments ever done.
The first kinetic test experiments could unfortunately not be finished during this work, due to several technical problems with our beamline and the reactor itself. Nevertheless every component for a future kinetic polarized neutron experiment is available and tested. In the following this next planned experiment, as well as some options for further refinements of the setup are outlined.

The setup should also prove to be valuable for observing both spin states at the same time during relaxation processes.

6.1 Kinetic investigations with polarized neutrons

One of the original goals for this project was the execution of kinetic polarized neutron experiments. Due to a series of technical problems all components for this only became ready to use in the last months of this work so that the execution was outside the scope of this thesis.
Besides the normal experimental mishaps we experienced problems with the shutter of our beamline, once of an electronic nature that could be fixed after our experiment was aborted without collecting useful data, and once a mechanical problem that required the complete disassembly of PUMA. Fixing the problem and reassembling PUMA took two full beam cycles. An additional cycle was lost due to damage on a secondary reactor component shutting down the whole reactor. One more cycle was lost due to massive software problems at the spectrometer, and finally we also experienced reduced beam time due to a lack of fuel elements.
Due to these problems during this thesis there where two years where no test or experiments could be conducted as PUMA, or the whole FRMII, was inoperable. In two cases these problems manifested during a measurement, prematurely ending the planed experiment.
After finishing the polarization analysis and CuO experiments we searched for a possible test experiment utilizing all features of PUMA. For this first planed kinetic experiment using the experimental setup developed in this work we will examine $CoCr_2O_4$ under the influence of an oscillating magnetic field. A roughly 2x3x5 mm^3 crystal was obtained from MaTecK in the last months before the end of this work so only some preliminary work for a kinetic experiment can be described in this thesis. $CoCr_2O_4$ undergoes a reversal of its spontaneous polarization and magnetization under a weak external magnetic field of roughly 0.1 T, see [31]. Using an oscillating electro-magnet to trigger the reversal of the spontaneous polarization and magnetization in the ferroelectric phase (between 15-26 K) the crystal seems to be a good model for investigating the kinetic behavior of such changes.

6.1.1 Oscillating magnetic field; construction and first tests

As we want to do kinetic polarized neutron experiments under a varying magnetic field a suitable magnet was needed. The magnetic field has to be parallel/anti-parallel to the guide field and strong

enough to trigger (e. g.) phase transitions in a sample. As the magnet is intended to work inside a cryostat it had to be as compact as possible. In the end an electromagnet with a volume of 105x60x30 mm^3 was build that also functions as the sample holder. A sketch of the final design for the magnet is shown in Fig. 63.

We tested several different coil setups, using different cores (soft iron, mu-metal with and without heat treatment…) and copper wire of varying diameters. In the end we chose a round wire with 0.8mm diameter. Even if smaller diameter wire would have been preferable for its higher density of windings the smaller wires turned out to get too hot. Wires with a diameter larger than 0.8 tended to be too stiff, thus making a tight winding impossible. In addition to this thicker wire simply means fewer windings and so to a weaker magnet. For the core material heat treated mu-metal with a maximal magnetic permeability of up to 250000 Hm^{-1} was chosen.

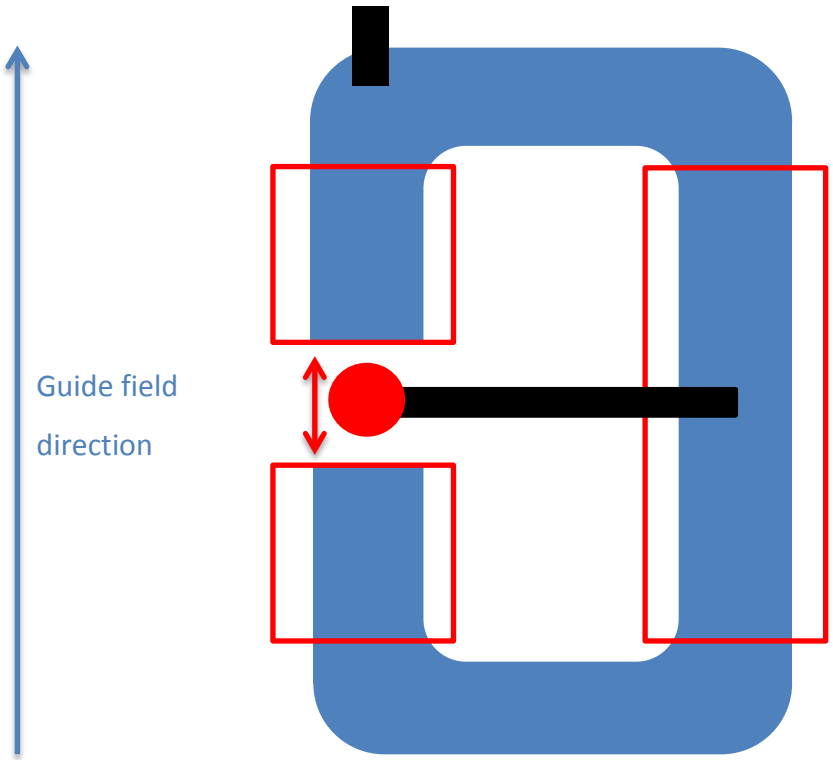

Fig. 63: Sketch of the magnet for the oscillating field. Red frames show the position of the coil segments, the red ball the sample position. Black rectangle above the sample is the screw that connects the magnet with the coldhead. Double headed red arrow indicates the direction of the produced magnetic field.

As we couldn't wind our coil directly on the core, for obvious geometric reasons, some workaround had to be found. This was done by winding a set of small coils on a plastic core with a slightly bigger diameter than our Mu-metal core and a length corresponding to the opening in the core. Then the plastic core was inserted into the opening and the coil carefully pushed to its final position. In the end the six resulting coil parts were soldered together to form a single coil around our core.

In the end there were 458 windings in total with an ohmic resistance of 2 Ω at room temperature. This high resistance can be explained by transfer resistance at the soldered connections between each of the six partial coils.

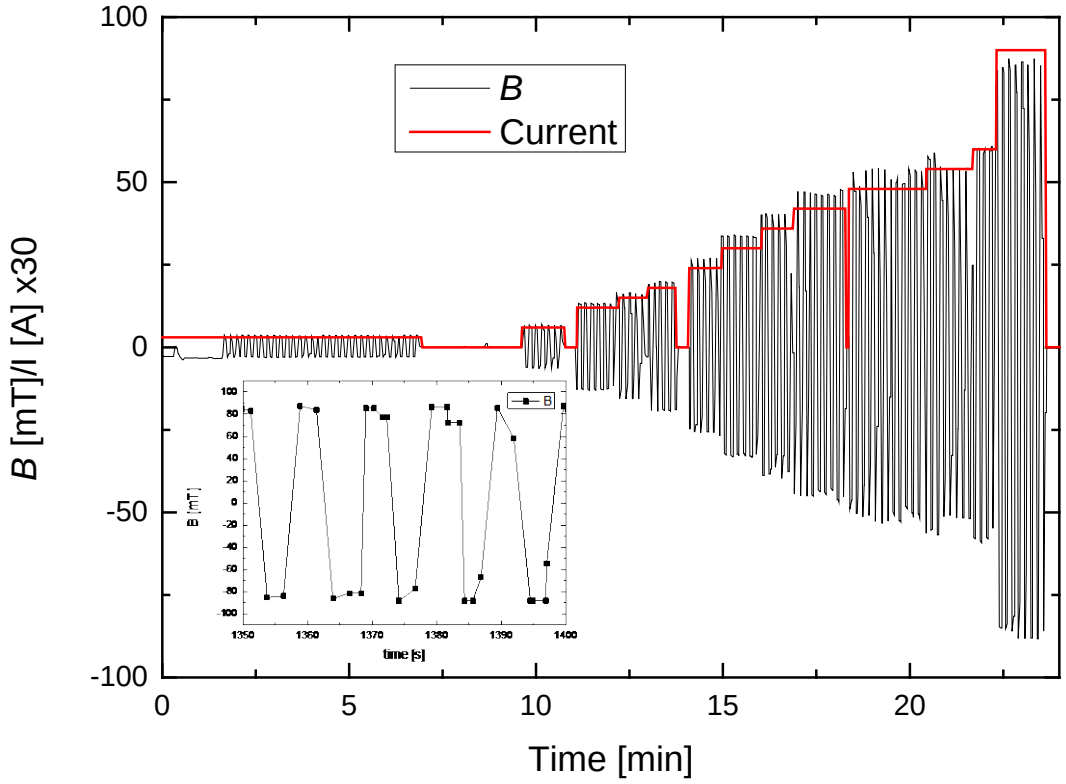

Fig. 64: B-field over time. The field closely follows the given current. Insert shows a close up to better illustrate switching behavior. The red curve is the given current amplified by a factor 30 it closely matches the amplitude of our magnetic field.

The magnet provides a magnetic field of up to 0.12 T under ambient conditions at a current of 5 A. A test of the magnet's behavior for up to I=3 A is shown in Fig. 64. Magnetic field strength closely follows given current. Even so, field strength should be measured during an experiment to make sure how changes in temperature and interactions with the guide field influence the magnetic field at sample position. Also shown in Fig. 64 is a small insert of a close up of the plot showing that the field profile over time is almost rectangular.

A switching frequency of some 100 Hz was reached under ambient conditions.

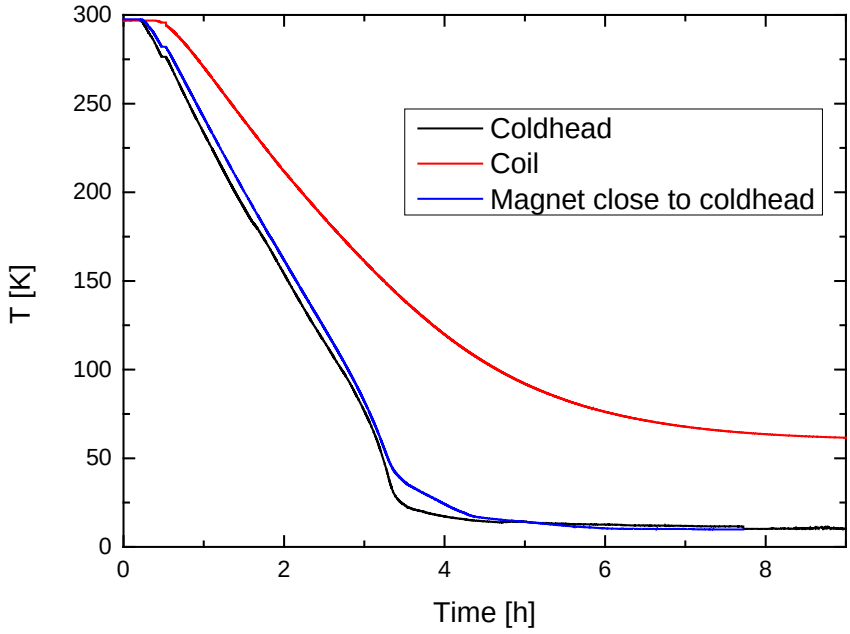

Fig. 65: Temperature of the coldhead, coil and magnetic core close to coldhead over time.

During operation the magnet could be cooled down to a temperature of 12 K as measured close to the cold head that corresponds to a temperature of 62 K on the windings, some distance removed from the coldhead, see Fig. 65. After this work was finalized a stable temperature of 5 K at the sample position was achieved with an inactive magnet and 24 K while the magnet received a current of 2.5 A producing a 133 mT field. A photo of the finished magnet is shown in Fig. 66.

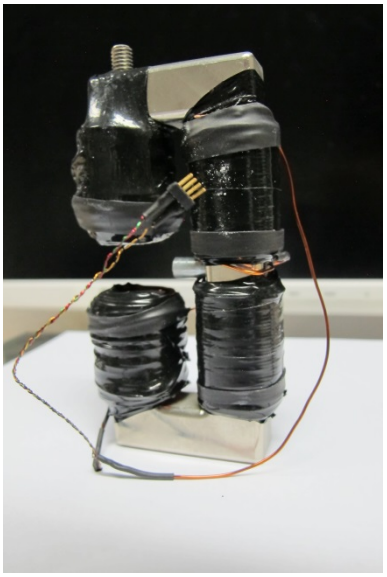

Fig. 66: Photo of the magnet

6.1.2 $CoCr_2O_4$

$CoCr_2O_4$ is like CuO a multiferroic material, meaning that it shows both ferroelectricity as well as ferromagnetism. In general multiferroics are interesting research subjects, as they show a wide range of uncommon magnetic behaviors, as well as high potential for technical applications of the same. Cobalt-dichromate is also the first example of a multiferroic material where both the spontaneous magnetization and spontaneous polarization are of spin origin and that shows reversal of the electric polarization by reversal of its magnetization. Yamasaki et al. investigated the electric response to an external magnetic field in 2006 [31].

The space group of $CoCr_2O_4$ is $Fd\bar{3}m$ at roomtemperature, and it shows a ferromagnetic phase between T_C=94 K and T_S=26 K as well as a ferroelectric phase between T_S and $T_{lock\text{-}in}$=15 K, and a possible phase transition at 5 K as found in [32]. The ferroelectric phase shows cone shaped spin states with a spiral component described by an incommensurate vector of (0.63 0.63 0) within the (0 0 1) plane as well as a ferrimagnetic component along the [0 0 1] direction. This structural transition to a conical spin states is also paired with the emergence of spontaneous electric polarization along the [-1 1 0] direction. In the ferroelectric phase, a small external magnetic field of around 0.1 T is sufficient for a reversal of its spontaneous polarization and magnetization.

At $T_{lock\text{-}in}$ the spin spirals period become commensurate, it “locks” to the lattice parameter.

Using an external oscillating magnetic field, described in the following section, and the time resolved measurement option of PUMA such an experiment could be a good test for kinetic measurements using polarized neutrons.

This could be a unique option for testing a kinetic inelastic neutron experiment with our setup.

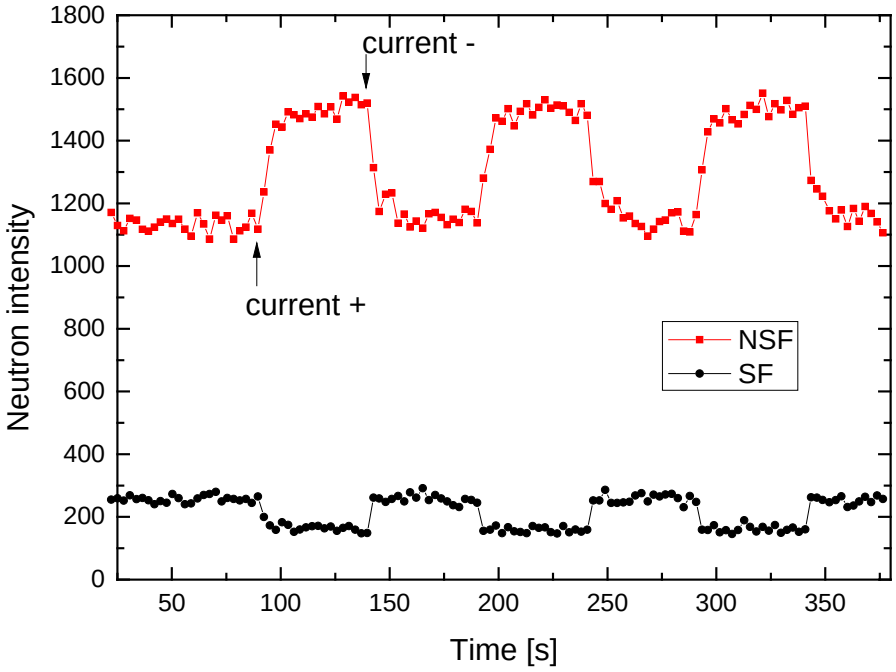

Fig. 67: First test measurement on $CoCr_2O_4$ (0 4 0) lattice reflection with an alternating external magnetic field of ≈0.1 T

A first test measurement of the crystal at PUMA was recently done, shown in Fig. 67. The (0 4 0) lattice reflection was measured under the influence of an external magnetic field, switching between ± 0.1 T and at a temperature somewhat above 30 K. Measurement starts with positive magnetic field current until the 90 seconds mark where the field direction is reversed. Positive current means that the sample and guide field are parallel to each other and minus current means anti-parallel. The data set contains three full periods and taking each data point took a little over 2 seconds. We see that NSF and SF intensities of the lattice reflection behave differently under the external field. The sample was in the ferromagnetic phase and the magnetic field parallel to the guide field. Even without stroboscopic techniques, where the periodical excitation of the sample by our magnet with a timed detection of scattered neutrons, see [33], we can already see that with current in – direction SF intensity increases. With field current switched in + direction the overall intensity of the reflection increases. There is also some asymmetry in the increase and decrease of NSF intensity when the field is switched. Increasing NSF intensity takes around 8 seconds, while after switching back it takes 14 seconds to go back to a constant count rate. Also after switching to + the increase in intensity looks like a fast linear increase, while the decrease starts very steep and then goes over into a tail, looking more logarithmic.

In contrast to this the SF signal shows a more symmetric and abrupt reaction to field switches.

Even with this very short test measurement we already see some features like an influence of the external magnetic field. Considering this doing a full kinetic experiment looks very promising.

6.2 Possible future improvements and advanced approaches for the PUMA polarization analysis

6.2.1 Intensity optimization

As shown in Fig. 37 a) a lot of the beam intensity is lost at the analyzer (red curve). The reason for this is that the three component beams are broader than the projection of the analyzer blades. The blades have a width of 25 mm resulting in a projected width of 8.8 mm if the (002) reflection of PG is used. As the beam divergence is broader than the analyzer blades some neutron flux is missing the analyzers and therefore is lost for the detectors.
By using the (004) reflection of the analyzers a larger angle could be chosen, increasing the projected width of each analyzer to 16.5 mm. This would increase the amount of scattered neutrons redirected towards the detectors even if the analyzer reflectivity is reduced. Fig. 68 illustrates this effect

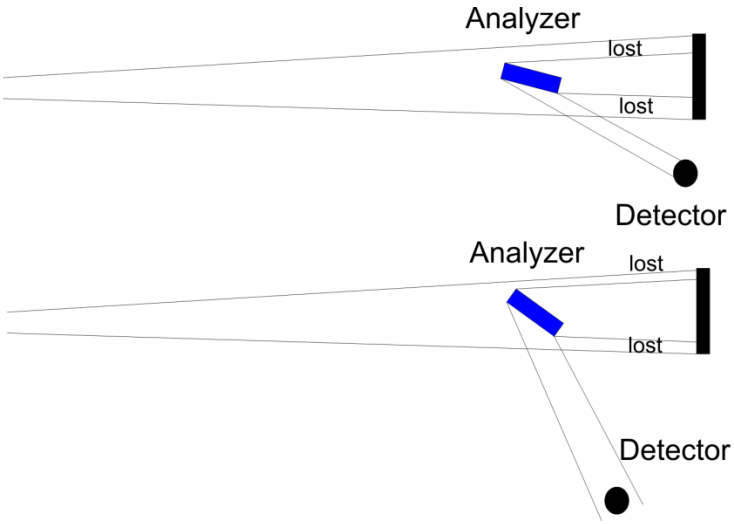

Fig. 68: Sketch to illustrate the effect of using a higher order reflection for the analyzers

6.2.2 Full 3d polarization analysis

Another option would be to further develop PUMA for a full 3d polarization analysis. For this, there are basically two existing options, CryoPAD and MuPAD. Both systems work by providing a field free

sample environment, CryoPAD by utilizing the Meissner effect and MuPAD with a Mu-metal shielding. A detailed description of both PADs can be found in [6, 7].
This could not be combined with the oscillating magnetic field discussed above in 6.1.1
A combination of full 3d polarization analysis and kinetic experiments, using an external magnetic field seem not feasible as the magnetic field at the sample would add a magnetic field to the field free zone of the PAD. This eliminates the main advantage of the PAD, as now the spin of the incident (and scattered) neutrons will start to orient itself along the field. In this way the full 3d approach for incident beam-sample interaction gets lost. On the other hand experiments with, for example, an electric field would still be possible and offer additional insights. Another problem with a full 3d analysis would be the size of CryoPAD/MuPAD. Installation of a PAD instead of our quasi-Helmholtz-coil means that the optical rails have to be farther removed from the sample position. This results in a further elongated experimental setup. There is simply no space in the experimental hall to combine our option to measure both spin channels simultaneously with a 3d option.

7 Handbook for the PUMA polarization setup

7.1 Setup check-list

1. Change PUMA to MAD setup
    a. check for wire connections, voltage, etc. (remember 5mm atx offset[14])
    b. Check k_i and k_f setting

2. Install PE insert in the analyzer window
3. Install both optical benches
    a. Clear the shorter optical rail on the monochromator side. Check that there is enough room for the helium box and a slit
    b. Rail on analyser side
        i. Use the 1 m rail with the supporting
        ii. Check that the rail is perpendicular to the entry window of the analyser
        iii. Re-check after every new component on the optical rail and
4. Install Quasi-Helmholtz guide field
    a. Lower coil, install the three holders on the sample table. Check the wires between coil and power source for range of movement
    b. Install holder for the upper coil on the rail on the monochromator side of the setup. Take care that both coils are above each other
    c. Use the connector of the shielding drum for the holder of the upper coil
    d. Check guide field orientation and strength
5. Install slits on both rails
6. Install PG-filter
7. Collimator
    a. Install 30‘ Collimator on rail 2 behind the slit
    b. Check alignment of the rail
    c. PSD collimator scan, integrated, move to highest intensity
8. Two deflectors
    a. Deflector 1 (if possible use deflector No.3)
        i. Install deflector 1 80 cm away from the analyser rotating center on rail 1

[14] Atx offset is necessary during the installation of the MA to avoid collisions

ii. (*)Deflector scan, PSD integrated. Scan around the range of expected intensity (should be around -0,8° for deflector 1)
iii. Move to maximal intensity, take a PSD histogram
iv. Determine angle of deflector using the histogram, if necessary move deflector take a histogram to confirm position
v. Note distance between deflector 1 and analyser window (gives the distance to the analyser rotation center and the detector)
vi. Note distance between deflector 1 and sample (accuracy should be around a few mm)
vii. Reconfirm orientation of the rail

b. If rail needs to be adjusted, redo collimator and deflector scans
c. Deflector 2 (if possible use deflector No.2)
i. Install deflector 1 75 cm away from the analyser rotating center on rail 1
ii. (*)Deflector scan, PSD integrated. Scan around the range of expected intensity (should be around 0,75° for deflector 2)
iii. Move to maximal intensity, take a PSD histogram
iv. Determine angle of deflector using the histogram, if necessary move deflector take a histogram to confirm position
v. Note distance between deflector 2 and analyser window (gives the distance to the analyser rotation center and the detector)
vi. Note distance between deflector 2 and sample (accuracy should be around a few mm)
d. Reconfirm orientation of the rail

9. If rail needs to be adjusted, redo collimator and deflector scans
10. Install ^{3}He-cell
11. Initiate software

(*) Alternative: calculate multianalyser/-detector position using measured distances and α_1=-0,8° α_2=0,75°, position the analyser/detector and do deflector scans

Guide and detector scans to confirm

Scan for deflectors to confirm

Iterate

7.2 Detailed setup guide

As this is a new setup for PUMA this work includes this handbook how to install the polarization analysis, first in the form of a detailed description of the installation process, and then as a shorter list of necessary steps.
The PUMA polarization set-up consists of several components (in order of typical installation):

- Insert for analyzer window
- Optical benches
- Quasi-Helmholtz guide field
- Slits
- PG-filter
- Collimator
- Two deflectors
- ^{3}He-cell

1 Change to MAD setup:

Prior to the installation of any component the coupling between the analyzer box and the sample table needs to be changed. This is done by rotating the coupling by 90° and necessary to get space for the polarization set-up. That the coupling was rotated by 90° can and should be checked using the laser located on the monochromator castle window. When the coupling was changed it is important to check if the breaks have been reengaged. If the breaks are unlocked the distance between the analyzer and the sample will change while driving the spectrometer. This will result at least in wrong calibration calculations and probably even collisions between optical bench and sample table. In the best case this will make a recalibration of the setup necessary and could even lead to damages on the bench, the components installed on the bench, or the whole setup.
Before closing the shielding do not forget to connect the data cable from the MSTD-16 and MPSD8 module in the MAD.

2 Install PE insert in the analyzer window:

After changing the coupling between the analyzer box and sample table, which is necessary to move away the collimator holder for the normal setup allowing the installation of the MAD, an insert for the opening of the analyzer box can be installed. The insert, tooled from borated PE, reduces the opening to 4x4cm and minimizes background neutrons inside the Analyzer/Detector box.

3 Install optical benches:

The polarization set-up uses two optical benches to install all its components. On the reactor side of the spectrometer the normally installed optical rail is used to carry one slit, the helium cell and the upper part of the quasi-Helmholtz-coil. The optical rail on the analyzer side needs to be installed after switching the coupling between sample table and analyzer (note distance between sample and analyzer-center).

The optical rail installed at the analyzer side is 80 cm long and has a mark that shows the distance to analyzer center. Installing the rail it is important to mount it parallel to the neutron path. For proper alignment of the rail a machinist square can be used. From experience it is a good idea to orient it using the vertical metal plate connecting the rail to the analyzer box. Before the final alignment the lower support strut should be connected. When the rail is properly installed an adjusting aid with some adjustable screws is used to fix the orientation of the rail. There is also an additional support structure connecting the end of the rail with the MAD sample table coupling that doubles as a buffer for vibrations of the optical rail.

Small errors in the alignment of the optical bench can be compensated by rotating the deflectors and the collimator, but it is always preferable to have the best possible alignment already at the level of optical rail installation.

As the rail is in principle a long lever that is only fixed by three screws and the (soft) aluminum adjustment help, one should be very careful while moving around the bench and when installing additional components. If the bench is moved all prior adjustment of installed components is lost and has to be redone.

4 Install guide field:

Installing the guide field starts with installation of the lower coils three mountings. There is only one possible configuration for the mountings as they are asymmetrical and use two different sizes of screws. After the coil is placed carefully place the cable between coil and power-supply in a way that it doesn't catch anywhere during rotation of the sample table. And make sure that the cable is not in the neutron beam.

The upper coil is installed on the optical bench on the reactor side of the spectrometer. For this the holding devise of the shielding drum for the sample table is used. The upper coil should be in good alignment with the lower one.

5-7 Install slits, PG-filter and collimator:

The two slits are to be installed directly in front and after the sample, on the ends of the optical rails. The PG-filter follows behind the slit, in beam direction, on the analyzer side. Behind the filter follows the collimator, this can be a 30', or less common a 15', collimator. When the collimator is installed it needs to be calibrated using neutrons.

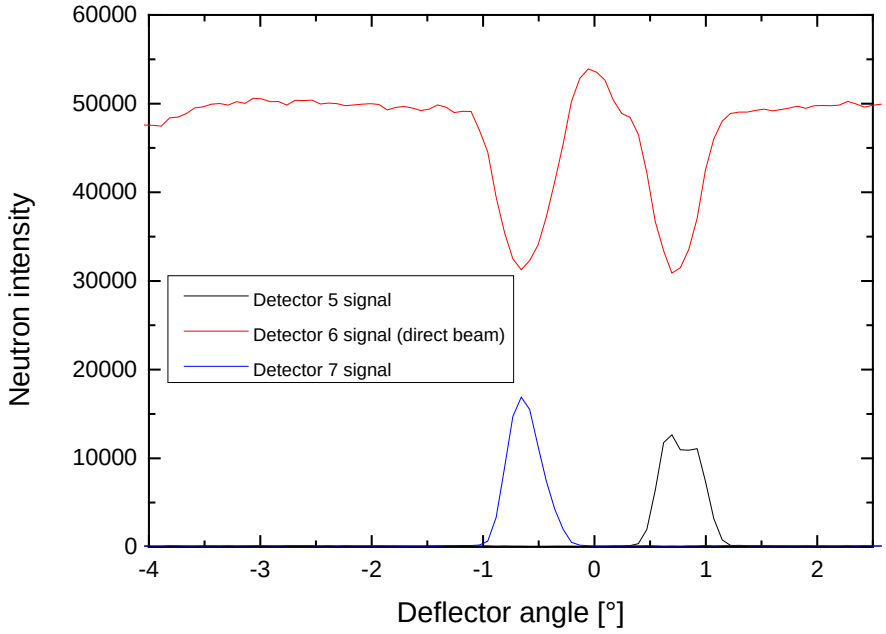

Fig. 69: Scan for optimal position of first deflector using PSD

To adjust the collimator a direct beam setup is used. The measurement can be done in two ways. One method is calculating the positions for the MAD using the software available at PUMA, and moving everything in position. Count while moving the collimator. If everything is aligned properly we get a Gaussian intensity profile as a function of collimator angle in the central detector, where the maximum of intensity corresponds to a collimator parallel to the beam.

The method we preferred is using the PSD and integrating intensity over the whole detector. Again, this gives a Gaussian with its maximum at the position where the collimator is parallel to the beam. After the optimal position has been noted down reference the collimator and move it into position coming from low motor-steps. This eliminates a potential backlash problem.

8 Install deflectors:

When this is done the first deflector can be installed at the correct position 80 cm distant form the analyzer center. To calibrate the deflector again rotate it in the direct beam. Again, this can be done by using either the MAD single detectors or the PSD.

Using the single detectors, if everything is correctly aligned rotating the deflector should give a constant count-rate in the central detector until the deflector starts to deflect neutrons away. These will turn up in the right detector. The maximum of intensity for the right detector gives a good position for the deflector.

Again, we preferred using the PSD, where we integrated over parts of the PSD corresponding to the position of the analyzer crystals. This gives an integrated intensity profile as in Fig. 69 where the dips

correspond to the reflecting position where neutrons are deflected away from the center of the PSD. We calibrate for the detector 7 channel signal, as the first deflector is associated with detector 7. After the deflector has been positioned, again reference and move form low angels to the determined position. Afterwards take a histogram to check the beam profile. This is one of the reasons the PSD is preferred above the single detectors as a histogram can be used to control the angle between deflector and beam. This is done by identifying the position of the central and deflected signals on the PSD. As each PSD channel corresponds to 0.3 mm we now have the distance between the beam components at PSD position, D_S. As we also know the distance between deflector and PSD, L_{DPSD}, we can now calculate the angle using $\gamma = \tan\left(\frac{D_S}{L_{DPSD}}\right)^{-1} \cdot \frac{1}{2}$.

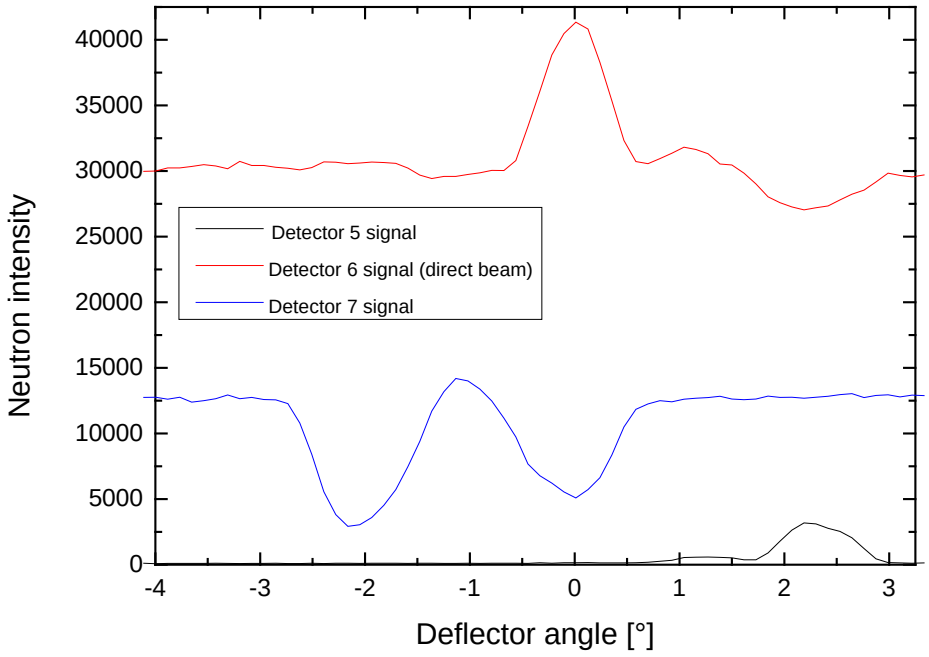

Fig. 70: Scan for optimal position of second deflector using PSD

For the second deflector the procedure is essentially the same, there is just a different looking plot, as shown in Fig. 70. What we see is how the second deflector moves through the direct beam, as well as the first deflected beam. Coming from negative angles, we first see it deflecting intensity from channel 7 away from the detector. Then it starts to deflect intensity from channel 7 back into the central channel until it is reaching its intended position where its deflected beam starts to hit detector channel 5. We optimize for this position. Note that this peak is broader and less well defined

compared to the peak from the first deflector, meaning that we have a bit more play how to position the second one. Again, check the angle of deflector 2 and note it down.

After this the positions of the relevant components should be noted down for the calculation of correction factors for the data analysis and nothing should be touched anymore.

Then, if it hasn't already be done, the positions for the MAD can be calculated and the analyzer and single detectors are moved into position.

From this point forward one can switch to the single detector setup and test the calculations by simply counting for a second. This should produce counts in the three central detectors. If this is not the case the first step should be to control if the MAD moved into position, then re-check all distances and angles used in the calculation, and finally a series of iterating deflector and guide scans.

10 Install ^{3}He-cell:

Put the cell in its holders and check the cell polarization with a short direct beam or lattice reflection measurement.

11 Initiate software setup:

There are three software setups;

a) 'defcal' setup for calibrating the components, PSD is used as detector
b) 'polarization' setup for the normal polarization analysis using the 11 single detectors of the MD. Data will be preprocessed by the mesydaq software and appear as standard FRMII NICOS data
c) 'polarizationkinetic' setup for kinetic polarization analysis using the MD single detectors. Data is saved in listmode '.mdat' with time stamps for each event (time resolution is 50 ns)

Start the experiment.

Take a look at section 5.2 to see how to handle the data.

8 Appendix

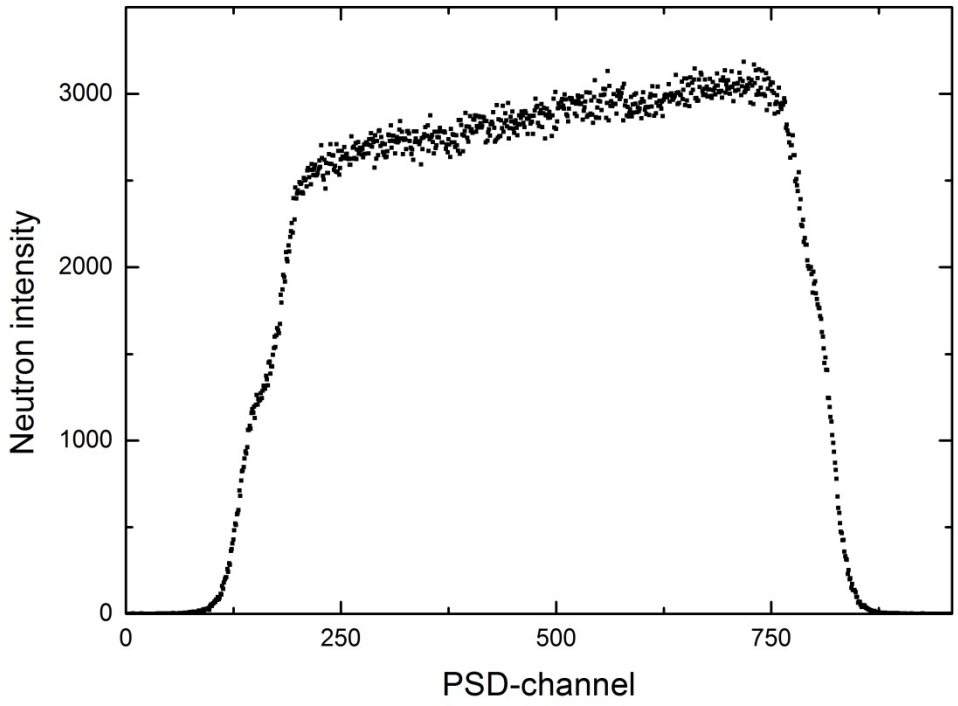

Fig. 71: Differences in efficiency along the full PSD range. A vanadium sample was used to expose the whole detector equally

8.1 Intermediate steps for guide field calculations

We get the following solution for a Poisson equation for the vector potential ***A***:

$$\boldsymbol{A}(\boldsymbol{r}) = \frac{\mu_0}{4\pi} \int d\boldsymbol{r}' \frac{\boldsymbol{j}(\boldsymbol{r}')}{|\boldsymbol{r} - \boldsymbol{r}'|} \tag{129}$$

If we write this out in cylindrical coordinates we get the following equations for the components of ***A***:

$$A_z = 0 \tag{130}$$

$$A_r = A_x \cos\varphi + A_y \sin\varphi$$
$$= \frac{\mu_0}{4\pi} NIR \int_0^{2\pi} d\varphi' \left(\frac{1}{\sqrt{z^2 - 2zz_0 + z_0^2 + R^2 + r^2 - 2rR\cos(\varphi - \varphi')}} + \frac{1}{\sqrt{z^2 + 2zz_0 + z_0^2 + R^2 + r^2 - 2rR\cos(\varphi - \varphi')}} \right) \sin(\varphi - \varphi') \quad (131)$$

$$A_\varphi = A_y \cos\varphi - A_x \sin\varphi$$
$$= \frac{\mu_0}{4\pi} NIR \int_0^{2\pi} d\varphi' \left(\frac{1}{\sqrt{z^2 - 2zz_0 + z_0^2 + R^2 + r^2 - 2rR\cos(\varphi - \varphi')}} + \frac{1}{\sqrt{z^2 + 2zz_0 + z_0^2 + R^2 + r^2 - 2rR\cos(\varphi - \varphi')}} \right) \cos(\varphi - \varphi') \quad (132)$$

From this we can start to calculate the magnetic field, using:

$$\boldsymbol{B} = \nabla \times \mathbf{A}$$
$$\boldsymbol{B}_r = \frac{1}{r}\frac{\partial \boldsymbol{A}_z}{\partial \varphi} - \frac{\partial \boldsymbol{A}_\varphi}{\partial \boldsymbol{z}}$$
$$\boldsymbol{B}_z = \frac{1}{r}\frac{\partial (r\boldsymbol{A}_z)}{\partial r} - \frac{1}{r}\frac{\partial \boldsymbol{A}_r}{\partial \varphi} \quad (133)$$
$$\boldsymbol{B}_\varphi = \frac{\partial \boldsymbol{A}_r}{\partial \boldsymbol{z}} - \frac{\partial \boldsymbol{A}_z}{\partial \boldsymbol{r}}$$

Also we get the following using Cartesian coordinates:

$$\boldsymbol{B}_x = \boldsymbol{B}_r \cos\varphi - \boldsymbol{B}_\varphi \sin\varphi$$
$$\boldsymbol{B}_y = \boldsymbol{B}_r \sin\varphi + \boldsymbol{B}_\varphi \cos\varphi \quad (134)$$

If we now calculate $\boldsymbol{B}_z$ using Biot-Savart for vector potentials (Equations (130), (131),(132)) we get after some transformations the following expression:

$$\boldsymbol{B}_z = \frac{\boldsymbol{A}_\varphi}{r} + \frac{\partial \boldsymbol{A}_\varphi}{\partial r} - \frac{1}{r}\frac{\partial \boldsymbol{A}_r}{\partial \varphi}$$
$$= \frac{\mu_0}{2\pi} NIR \int_{-1}^{1} dy \left(\frac{ry - R}{\sqrt{z^2 - 2zz_0 + z_0^2 + R^2 + r^2 - 2rRy}^3} + \frac{ry - R}{\sqrt{z^2 + 2zz_0 + z_0^2 + R^2 + r^2 - 2rRy}^3} \right) \frac{1}{\sqrt{1 - y^2}} \quad (135)$$

Appendix

Using $y = \cos\varphi'$ to calculate an expression for $\boldsymbol{B}_r$ we get equation (12).

Calculations for guide field profile along the beam path, starting with

$$\boldsymbol{B}_z(z=0) = \frac{\mu_0}{2\pi} NIR \int_{-1}^{1} dy\, 2 \frac{ry - R}{\sqrt{z_0^2 + R^2 + r^2 - 2rRy}^3} \frac{1}{\sqrt{1-y^2}} \tag{136}$$

$$\boldsymbol{B}_r(z=0) = 0 \tag{137}$$

If we, look at $z_0 = \frac{R}{2}$ we get for $\boldsymbol{B}_z$ and $\boldsymbol{B}_r$ the following equations:

$$\boldsymbol{B}_z = \frac{\mu_0}{2\pi} NIR \int_{-1}^{1} dy \left(\frac{ry - R}{\sqrt{z^2 - zR + \frac{5}{4}R^2 + r^2 - 2rRy}^3} + \frac{ry - R}{\sqrt{z^2 + zR + \frac{5}{4}R^2 + r^2 - 2rRy}^3} \right) \frac{1}{\sqrt{1-y^2}} \tag{138}$$

$$\boldsymbol{B}_r = -\frac{\mu_0}{2\pi} NIR \int_{-1}^{1} dy \left(\frac{z - \frac{R}{2}}{\sqrt{z^2 - zR + \frac{5}{4}R^2 + r^2 - 2rRy}^3} + \frac{z + \frac{R}{2}}{\sqrt{z^2 + zR + \frac{5}{4}R^2 + r^2 - 2rRy}^3} \right) \frac{y}{\sqrt{1-y^2}} \tag{139}$$

To simplify our problem we can consider it to be two dimensional, as the field lines can be expressed as level lines of A_y, meaning that

$$\boldsymbol{B}(y=0) = \begin{pmatrix} B_x \\ 0 \\ B_z \end{pmatrix} = \nabla \times \boldsymbol{A} = \begin{pmatrix} \frac{\partial A_z}{\partial y} - \frac{\partial A_y}{\partial z} \\ \frac{\partial A_z}{\partial x} - \frac{\partial A_x}{\partial z} \\ \frac{\partial A_y}{\partial x} - \frac{\partial A_x}{\partial y} \end{pmatrix} = \begin{pmatrix} -\frac{\partial A_y}{\partial z} \\ -\frac{\partial A_x}{\partial z} \\ \frac{\partial A_y}{\partial x} - \frac{\partial A_x}{\partial y} \end{pmatrix} \text{ for } A_z = 0 \tag{140}$$

Using cylindrical coordinates this leads to equation (19).

8.2 All magnetic scattering combinations

Full set of contributions to the scattering function for a case where x is parallel to **Q** (m_x vanishes):

(xx): 0

$(x\bar{x})$: $\left|-im_y + m_z\right|^2 = \left|m_y + im_z\right|^2 = (m_y + im_z) + (m_y^* - im_z^*) = \left(\left|m_y\right|^2 + |m_z|^2 - i(m_y m_z^* - m_y^* m_z)\right) = 2F$

(xy): $\frac{1}{4}\left|m_y + m_z - i(m_y + m_z)\right|^2 = \frac{1}{4}\left(m_y + m_z - i(m_y - m_z)\right)\left(m_y^* + m_z^* + i(m_y^* - m_z^*)\right) = \frac{1}{2}\left|m_y\right|^2 + \frac{1}{2}|m_z|^2 - i\frac{1}{2}(m_y m_z^* - m_y m_z^*) = F$

$(x\bar{y})$: $\frac{1}{4}\left|-m_y + m_z + i(m_y + m_z)\right|^2 = \frac{1}{4}\left(m_y - m_z + i(m_y + m_z)\right)\left(m_y^* - m_z^* - i(m_y^* + m_z^*)\right)$
$= \frac{1}{2}\left|m_y\right|^2 + \frac{1}{2}|m_z|^2 - i\frac{1}{2}(m_y m_z^* - m_y m_z^*) = F$

(xz): $\frac{1}{2}\left|im_y - m_z\right|^2 = \frac{1}{2}\left|m_y + im_z\right|^2 = \frac{1}{2}(m_y + im_z)(m_y^* - im_z^*) = \frac{1}{2}\left|m_y\right|^2 + \frac{1}{2}|m_z|^2 - i\frac{1}{2}(m_y m_z^* - m_y^* m_z) = F$

$(x\bar{z})$: $\frac{1}{2}\left|im_y - m_z\right|^2 = \frac{1}{2}\left|m_y + im_z\right|^2 = \frac{1}{2}(m_y + im_z)(m_y^* - im_z^*) = \frac{1}{2}\left|m_y\right|^2 + \frac{1}{2}|m_z|^2 - i\frac{1}{2}(m_y m_z^* - m_y^* m_z) = F$

$(\bar{x}x)$: $\left|im_y + m_z\right|^2 = \left|m_y - im_z\right|^2 = \left|m_y\right|^2 + |m_z|^2 + i(m_y m_z^* - m_y^* m_z) = 2E$

$(\overline{xx})$: 0

$(\bar{x}y)$: $\frac{1}{4}\left|m_y + m_z + i(m_y + m_z)\right|^2 = \frac{1}{4}\left(m_y + m_z + i(m_y - m_z)\right)\left(m_y^* + m_z^* - i(m_y^* - m_z^*)\right)$
$= \frac{1}{2}\left|m_y\right|^2 + \frac{1}{2}|m_z|^2 + i\frac{1}{2}(m_y m_z^* - m_y m_z^*) = E$

$(\overline{xy})$: $\frac{1}{4}\left|m_y + m_z + i(m_y - m_z)\right|^2 = \frac{1}{2}\left|m_y\right|^2 + \frac{1}{2}|m_z|^2 + i\frac{1}{2}(m_y m_z^* - m_y^* m_z) = E$

$(\bar{x}z)$: $\frac{1}{2}\left|im_y + m_z\right|^2 = \frac{1}{2}\left|m_y - im_z\right|^2 = \frac{1}{2}\left|m_y\right|^2 + \frac{1}{2}|m_z|^2 + i\frac{1}{2}(m_y m_z^* - m_y^* m_z) = E$

$(\overline{xz})$: $\frac{1}{2}\left|im_y + m_z\right|^2 = \frac{1}{2}\left|m_y - im_z\right|^2 = \frac{1}{2}\left|m_y\right|^2 + \frac{1}{2}|m_z|^2 + i\frac{1}{2}(m_y m_z^* - m_y^* m_z) = E$

(yx): $\frac{1}{4}\left|m_y + m_z + i(m_y - m_z)\right|^2 = \frac{1}{2}\left|m_y\right|^2 + \frac{1}{2}|m_z|^2 + i\frac{1}{2}(m_y m_z^* - m_y^* m_z) = E$

$(y\bar{x})$: $\frac{1}{4}\left|m_y + m_z - i(m_y - m_z)\right|^2 = \frac{1}{2}\left|m_y\right|^2 + \frac{1}{2}|m_z|^2 - i\frac{1}{2}(m_y m_z^* - m_y^* m_z) = F$

(yy): $\left|m_y\right|^2 = A$

Appendix

$(y\bar{y})$: $|m_z|^2 = B$

(yz): $\frac{1}{2}|m_y + m_z|^2 = \frac{1}{2}(m_y + m_z)(m_y^* + m_z^*) = \frac{1}{2}|m_y|^2 + \frac{1}{2}|m_z|^2 + \frac{1}{2}m_y m_z^* + \frac{1}{2}m_y^* m_z = C$

$(y\bar{z})$: $\frac{1}{2}|im_y - im_z|^2 = \frac{1}{2}|m_y - m_z|^2 = \frac{1}{2}(m_y - m_z)(m_y^* - m_z^*) = \frac{1}{2}|m_y|^2 + \frac{1}{2}|m_z|^2 - \frac{1}{2}m_y m_z^* - \frac{1}{2}m_y^* m_z = D$

$(\bar{y}x)$: $\frac{1}{4}|m_y + m_z - i(m_y - m_z)|^2 = \frac{1}{2}|m_y|^2 + \frac{1}{2}|m_z|^2 + i\frac{1}{2}(m_y m_z^* - m_y^* m_z) = F$

$(\overline{yx})$: $\frac{1}{4}|m_y + m_z - i(-m_y + m_z)|^2 = \frac{1}{4}|m_y - m_z + i(m_y + m_z)|^2$

$$= \frac{1}{4}\left(m_y - m_z + i(m_y + m_z)\right)\left(m_y^* - m_z^* - i(m_y^* + m_z^*)\right)$$

$$= \frac{1}{2}|m_y|^2 + \frac{1}{2}|m_z|^2 - i\frac{1}{2}(m_y m_z^* - m_y^* m_z) = F$$

$(\bar{y}y)$: $|m_z|^2 = B$

$(\overline{yy})$: $|m_y|^2$

$(\bar{y}z)$: $\frac{1}{2}|-m_y + m_z|^2 = \frac{1}{2}|m_y|^2 + \frac{1}{2}|m_z|^2 - \frac{1}{2}m_y m_z^* - \frac{1}{2}m_y^* m_z = D$

$(\overline{yz})$: $\frac{1}{2}|im_y + im_z|^2 = \frac{1}{2}|m_y + m_z|^2 = \frac{1}{2}|m_y|^2 + \frac{1}{2}|m_z|^2 + \frac{1}{2}m_y m_z^* + \frac{1}{2}m_y^* m_z = C$

(zx): $\frac{1}{2}|im_y + m_z|^2 = \frac{1}{2}|m_y - im_z|^2 = \frac{1}{2}|m_y|^2 + \frac{1}{2}|m_z|^2 + \frac{1}{2}i(m_y m_z^* - m_y^* m_z) = E$

$(z\bar{x})$: $\frac{1}{2}|-im_y + m_z|^2 = \frac{1}{2}|m_y + im_z|^2 = \frac{1}{2}|m_y|^2 + \frac{1}{2}|m_z|^2 - \frac{1}{2}i(m_y m_z^* - m_y^* m_z) = F$

(zy): $\frac{1}{2}|-m_y + m_z|^2 = \frac{1}{2}|m_y|^2 + \frac{1}{2}|m_z|^2 + \frac{1}{2}m_y m_z^* + \frac{1}{2}m_y^* m_z = C$

$(z\bar{y})$: $\frac{1}{2}|m_y + m_z|^2 = \frac{1}{2}|m_y|^2 + \frac{1}{2}|m_z|^2 - \frac{1}{2}m_y m_z^* - \frac{1}{2}m_y^* m_z = D$

(zz): $|m_z|^2 = B$

(zz): $|m_y|^2 = A$

$(\bar{z}x)$: $\frac{1}{2}|im_y + m_z|^2 = \frac{1}{2}|m_y - im_z|^2 = \frac{1}{2}|m_y|^2 + \frac{1}{2}|m_z|^2 + \frac{1}{2}i(m_y m_z^* - m_y^* m_z) = E$

$(\overline{zx})$: $\frac{1}{2}|-im_y + m_z|^2 = \frac{1}{2}|m_y + im_z|^2 = \frac{1}{2}|m_y|^2 + \frac{1}{2}|m_z|^2 - \frac{1}{2}i(m_y m_z^* - m_y^* m_z) = F$

$(\bar{z}y)$: $\frac{1}{2}|m_y - m_z|^2 = \frac{1}{2}|m_y|^2 + \frac{1}{2}|m_z|^2 - \frac{1}{2}m_y m_z^* - \frac{1}{2}m_y^* m_z = D$

$(\overline{zy})$: $\frac{1}{2}|m_y + m_z|^2 = \frac{1}{2}|m_y|^2 + \frac{1}{2}|m_z|^2 + \frac{1}{2}m_y m_z^* + \frac{1}{2}m_y^* m_z = C$

$(\bar{z}z)$: $|m_y|^2 = A$

$(\overline{zz})$: $|m_z|^2 = B$

All of these possible contributions can be expressed by only six different terms. They are shown in section 4.3 “Theory of polarized neutron scattering”

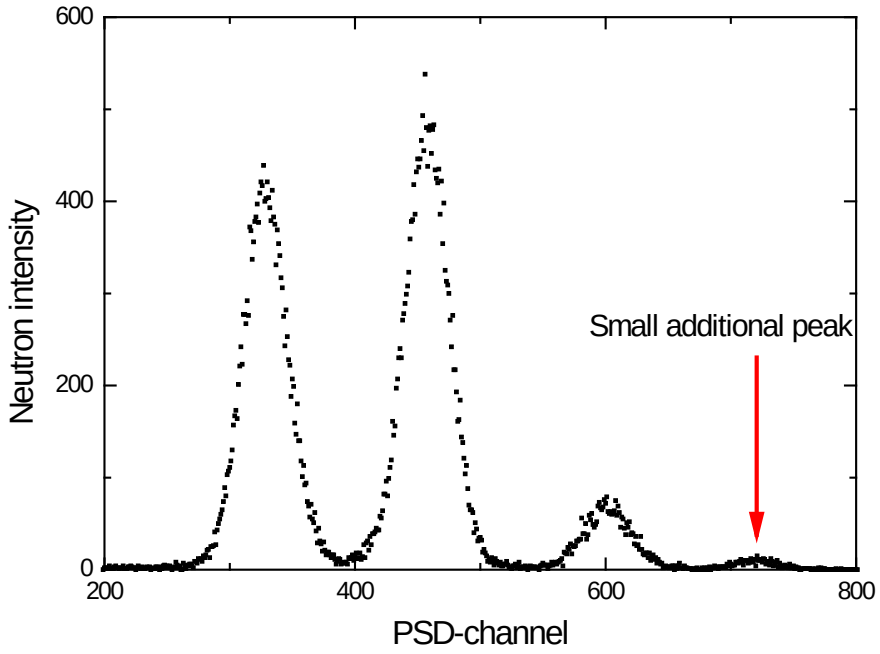

Fig. 72: Occurrence of a small fourth peak. This was observed when deflector 2 was in front of deflector 3 and vanished when 3 was in front. Probably a chance interaction of small manufacturing imperfections is responsible.

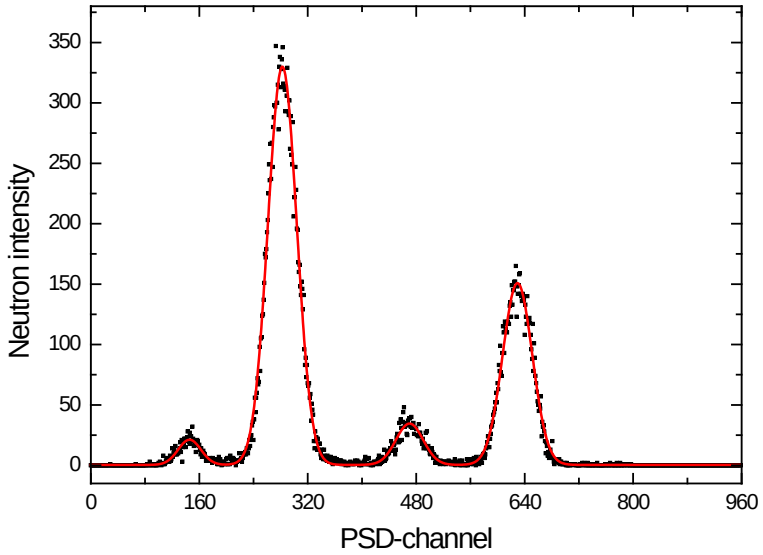

Fig. 73: PSD image for a three deflector beam profile. There is a significant change in the deflected/direct beam quotient compared to the two deflector setup from **Fig. 17** (0,81 to 0,623)

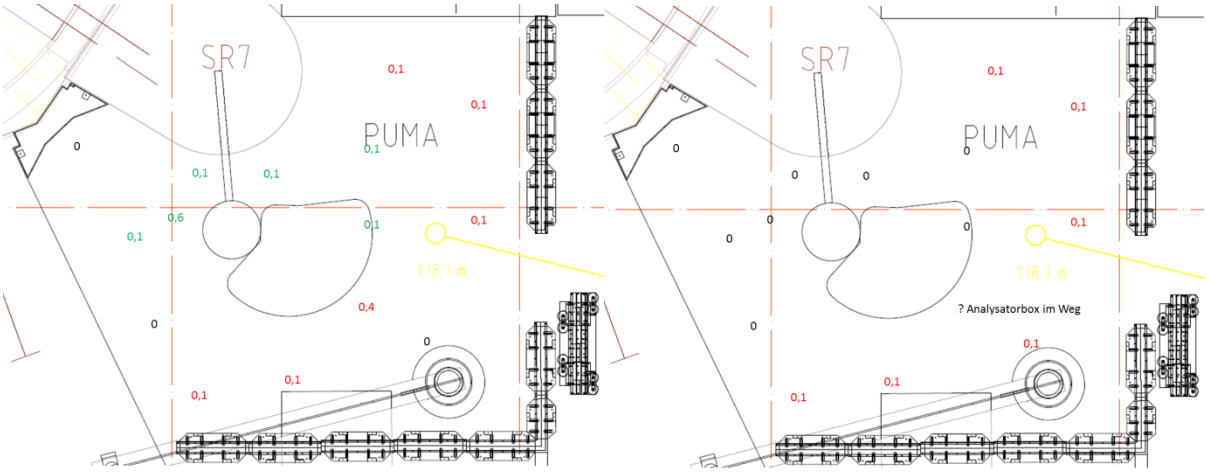

Fig. 74: Magnetic field in the experimental area of PUMA on 03.05.2016. On the left directly above ground level and on the right in 1m height. Green numbers show south-pole, red ones a north-pole, in units of [mT]

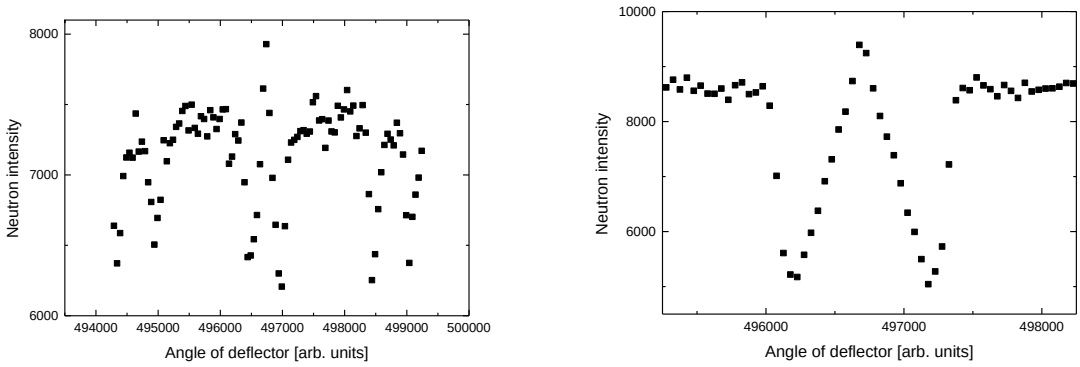

Fig. 75: Two scans for deflector calibration (deflector 2 September 2015). On the left without a PG-filter and on the right with filter inserted into the beam-path. In addition to the effect of eliminating higher order neutrons, the behavior of the deflector as collimator is clearly shown.

x-position [cm]	-20	-10	0	10	20
I[A]					
0	0.9	0.1	0.1	0.1	0.8
1	2.1	1.6	1.4	1.6	1.8
2	3.3	2.8	2.8	2.8	3
3	4.5	4.2	4.2	4.2	4.5
4	5.5	5.5	5.4	5.4	5.5
5	7	7	6.6	6.6	7
6	8.3	8.1	8	8.1	8.3
7	9.9	9.2	9.2	9.2	9.5
8	10.8	10.7	10.7	10.7	10.7
9	12.3	11.9	11.6	11.8	11.9
10	13.7	13.4	12.8	13.2	12.8

Table 8: Measured magnetic flux of the PANDA guide field in [mT] coil in units of mT. Direction of x is arbitrary.

y-position [cm]	-20	-10	0	10	20
I[A]					
0	0.7	0.1	0.1	0.1	0.9
1	1.8	1.6	1.4	1.6	1.8
2	3	2.8	2.8	2.8	3
3	4.5	4.2	4.2	4.2	4.5
4	5.4	5.4	5.4	5.4	5.5
5	7	6.7	6.6	6.9	7
6	8.2	8.1	8	8.1	8.2
7	9.2	9.4	9.2	9.5	9.5
8	10.7	10.8	10.4	10.8	10.7
9	11.9	11.9	11.7	12	12
10	12.8	13.3	12.9	13.2	13.4

Table 9: Same as **Table 8** but in y-direction, perpendicular to x.

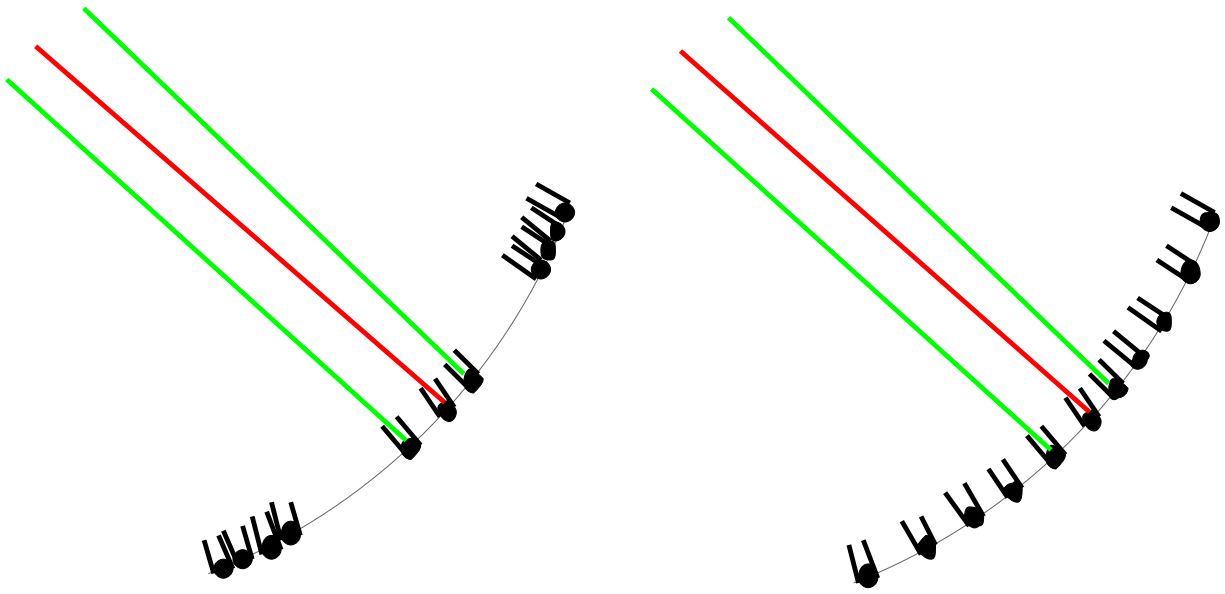

Fig. 76: On the left a sketch for the detector position as used during this work. On the right a sketch for an equidistant positioning of the detectors recommended to help estimating background during an experiment.

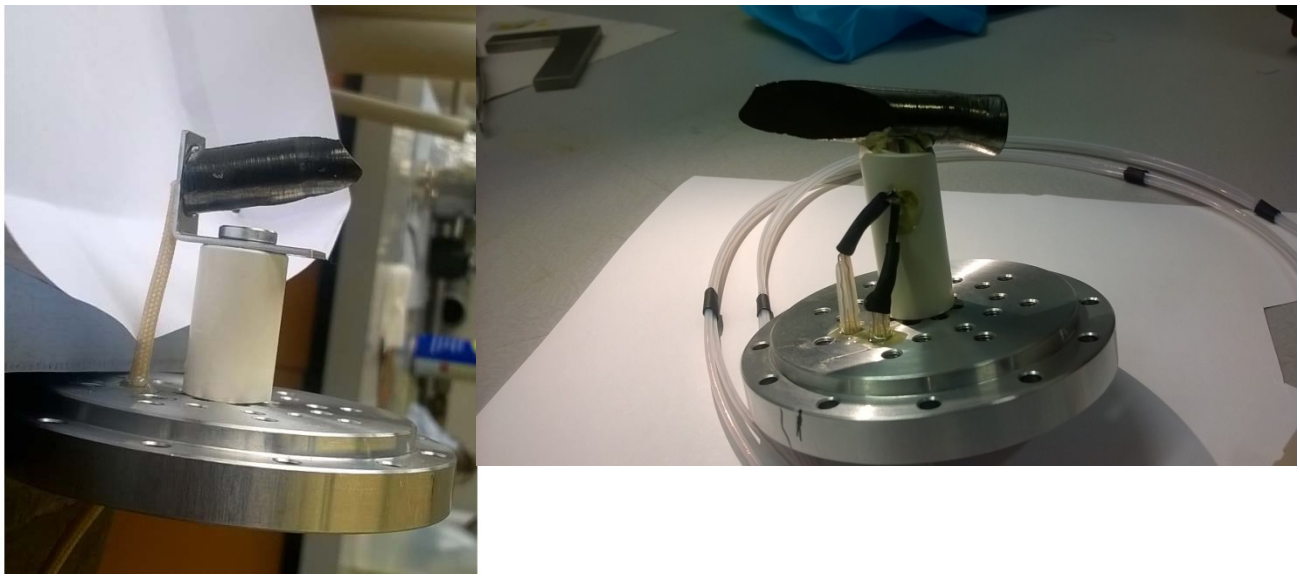

Fig. 77: CuO-sample after (left) and before (right) the cut. Note the boron nitride shielding for the sample holder and the wires for the second temperature sensor. On the left the sensor is directly behind the sample and on the right inserted into the sample holder

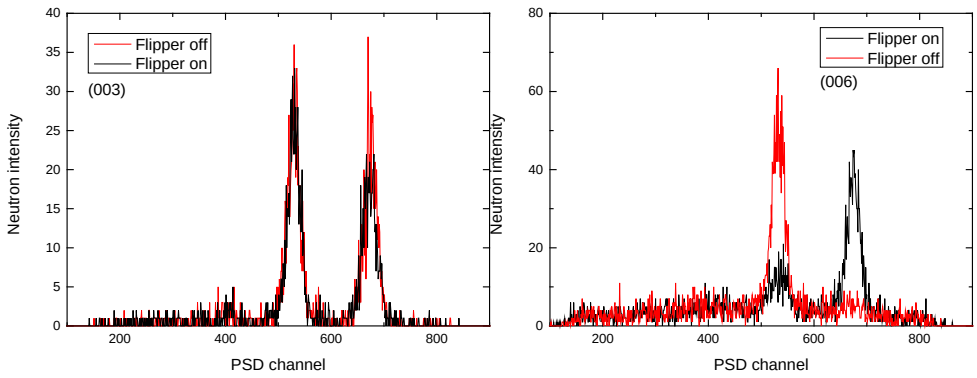

Fig. 78: Alternative display of Fig. for the first test experiment on Hematite. On the left measurement of AFM (003) reflex, on the right nuclear (006) reflex

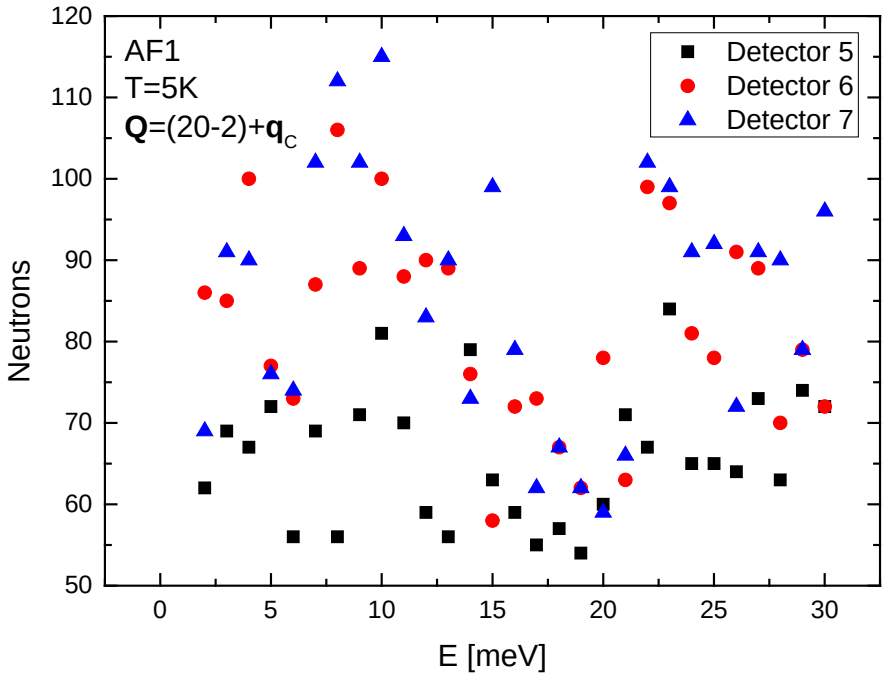

Fig. 79: The same scan as in Fig. 62 but before all corrections and "cosmetics"

In Fig. 79 the uncorrected raw data for the constant q scan seen in Fig. 62 is shown. The difference between the two plots is a result of the following data manipulation steps:

- First the background is reduced as discussed in section 5.2
- Then the detector count rates are transferred into SF and NSF count rates, as shown in section 4.3.1 "Analytical calculations for PUMA polarization analysis". A Bose correction of the data is done by dividing the count rate by $e^{h\nu\beta} - 1$
    - Because of the low temperature this has nearly no effect on the data. The correction was done to assure comparability with an older measurement at a higher temperature (this data is shown in Fig. 53 b))
- To somewhat smooth the data the average between two neighboring data points is plotted
- Finally error bars are calculated and added

In the appendix (Fig. 41) is a three step plot for the data correction of this scan with some additional remarks.

8.3 Technical details useful to remember

Information regarding the PSD:

- The PSD tubes require voltage of 1750.0 V
- Corresponding configuration in MESYDAQ computer is 'PSD.mcfg'
- Common Gain 128 and Common Threshold 139
- First Data Bus channel of the central module is FED by the PSD signal.
- In NICOS the voltage ramping can be done using 'hv1' device
- Count command on PSD will be saved as a histogram file in the service folder using the name structure 'puma_0000xxxx'
- In NICOS command line every count command will give img.sum, peak1, peak2, peak3, which are summations over different ranges of interest in channels & tubes, which can be changed by:
    - peak1.roi=(start ch no, start tube no, increment in ch no, increment in tube no)
    - peak2.roi=(start ch no, start tube no, increment in ch no, increment in tube no)
    - peak3.roi=(start ch no, start tube no, increment in ch no, increment in tube no)

Information regarding the MAD single detectors:

- The required voltage is 1550.0 V
- Corresponding configuration in MESYDAQ computer is '##.mcfg'.
- Third Data Bus channel of the central module is FED by the SD signal.
- Common Gain 92 and Common Threshold 15

How the channels are named in in Mesytec and NICOS software. The first two are monitor counts, sum over all detectors and then the corresponding MD channels

Mesytec	NICOS	MD channels
0	1	
1	2	
2	3	1

3	4	2
4	5	3
5	6	4
6	7	5
7	8	6
8	9	7
9	10	8
10	11	9
11	12	10
12	13	11

OPTICAL ALLIGNMENT:

<u>After changing the coupling between sample table and analyzer (ATT change by 90 degree):</u>

Install and set:

Collimators: 20', and 24'

phi.motor.stopdelay=10

Air pressure under the blue box = 4

<u>Alignment of MA using neutrons:</u>

1st step

Remove single analyzer

Make ATH.OFFSET = 0

Make ATH = 0

Make ATT = 90

Make ATX=0; ATY=0

90° = ATT - CAD

Check for the following:

ATT = 90 -> CAD = 0°; ATT = 85° -> CAD = 15°; etc.

Insert the MA while

ATX=+5 mm, ATY=0, ATH=0, ATT=90

CAD has no intrinsic offset.

CAD offset is related to ATT.OFFSET

2nd step

Keep CAD = -27.2º (nominal)

rd6=-14.0º

Such that rd6_cad=-41.2º

Make scan for ra6 around -20.6º [Take care, this axis has huge backlash]

If no intensity found during ra6 scan do the following

3rd step

Move ra6 to -20.6º(nominal) [backlash!!!]

Make as much space around rd6, as possible by moving the other detectors to the sides

Do a broad scan for rd6 around the position rd6=-14º [cad at -27.2º]

Iterate between ra6 scan and rd6 scan to determine the offset properly

ra6.offset=?

rd6.offset=?

After this do a ta6 scan around ta6=5mm to get the max intensity [remember nominally ta6=5 mm is at the center of the goniometer, as ATX=5 mm, because of the MA installation]

Set ta6=5 mm with proper offset

If you wish you can iterate between ta6 and ra6 while rd6 is fixed, later again ta6=5 mm and iterate between ra6 and rd6

This step is important as depending on that all rd# and rg# offsets will be determined.

4th step

Keep ra6 after offset correction at -20.6º, ta6=5 mm

Keep all the detectors 4º apart with rg#=0º[optically]

Move the whole multi detector by CAD to determine calculated position and the real position from neutron intensity and determine the offsets

Put all the offsets found from the neutron alignment of the beam reflected from ra6

5th step

Once all the detectors are aligned, keeping each of the detectors at the reflected beam positions, do the corresponding rg# scans.

When the intensity starts falling down sharply, set that value to 0º for each of the guide.

After all offsets are properly adjusted, all the rg# 0 and rd# are 4º apart from each other do a CAD scan with high statistics.

6th step:

Once all rd#, rg# are aligned, with help of already aligned ra6 reflected beam, align rest of the ra#s

This is done via putting the corresponding analyzer on the beam path via moving PHI

9 Bibliography

References

1. Sobolev O, Park JT. PUMA: Thermal three axes spectrometer. JLSRF. 2015;1:A13. doi:10.17815/jlsrf-1-36.

2. Sobolev O, Hoffmann R, Gibhardt H, Jünke N, Knorr A, Meyer V, Eckold G. The multianalyser system of the three axes neutron spectrometer PUMA: Pilot experiments with the innovative multiplex technique. Nucl. Instrum. Methods Phys. Res. A. 2014;772:63–71. doi:10.1016/j.nima.2014.11.007.

3. Lefmann K, McMorrow DF, Rønnow HM, Nielsen K, Clausen KN, Lake B, Aeppli G. Added fexibility in triple axis spectrometers: the two RITAs at Risø. Physica B. 2000:343–54.

4. Born R, Hohlwein D. Simultaneous energy analysis in a large angular range: A novel neutron spectrometer, its resolution and applications. Z. Physik B - Condensed Matter. 1989:547–55.

5. E. R. Pike, Pierre C. Sabatier, editors. Scattering: Scattering and Inverse Scattering in Pure and Applied Science: Academic Press; 2001.

6. Tasset F. Zero field neutron polarimetry. Physica B. 1989:627–30.

7. Janoschek M, Klimko S, Gähler R, Roessli B, Böni P. Spherical neutron polarimetry with MuPAD. Physica B: Condensed Matter. 2007;397:125–30. doi:10.1016/j.physb.2007.02.074.

8. Hutanu V, Meven M, Sazonov A, Heger G. Development of compact magnetostatic cavities for 3 He spin filter cells. Meas. Sci. Technol. 2008;19:34010. doi:10.1088/0957-0233/19/3/034010.

9. Hutanu V, Meven M, Masalovich S, Heger G, Roth G. 3 He spin filters for spherical neutron polarimetry at the hot neutrons single crystal diffractometer POLI-HEiDi. J. Phys.: Conf. Ser. 2011;294:12012. doi:10.1088/1742-6596/294/1/012012.

10. M. Batz, S. Baeßler, W. Heil, E. W. Otten, D. Rudersdorf, J. Schmiedeskamp, Y. Sobolev, and M. Wolf. 3He Spin Filter for Neutrons. Journal of Research of the National Institute of Standards and Technology;2005:293–8.

11. Masalovich S. Method to measure neutron beam polarization with 2×1 Neutron Spin Filter. Nucl. Instrum. Methods Phys. Res. A. 2007;581:791–8. doi:10.1016/j.nima.2007.08.150.

12. Cooper-Jensen CP, Vorobiev A, Klinkby E, Kapaklis V, Wilkens H, Rats D, et al. "m=1" coatings for neutron guides. J. Phys.: Conf. Ser. 2014;528:12005. doi:10.1088/1742-6596/528/1/012005.

13. Schanzer C, Schneider M, Böni P. Neutron Optics: Towards Applications for Hot Neutrons. J. Phys.: Conf. Ser. 2016;746:12024. doi:10.1088/1742-6596/746/1/012024.

14. J_Penfold_1990_J._Phys.__Condens._Matter_2_001.

15. B. O. LOOPSTRA. NEUTRON POWDER DIFFRACTOMETRY USING A WAVELENGTH OF 2.6 A*. Nuclear Instruments and Methods in Physics Research. 1966:181–7.

16. Schwesig S, Maity A, Sobolev O, Ziegler F, Eckold G. Novel type of neutron polarization analysis using the multianalyzer-equipment of the three-axes spectrometer PUMA. Nucl. Instrum. Methods Phys. Res. A. 2018;877:124–30. doi:10.1016/j.nima.2017.09.032.

17. Shirane G, Shapiro SM, Tranquada JM. Neutron Scattering with a Triple-Axis Spectrometer: Basic Techniques. Cambridge: Cambridge University Press; 2002.

18. van Hove L. Correlations in space and time and Born approximation scattering in systems of interacting particles. Phys. Rev. 1954:249–62.

19. Eckold G, Sobolev O. Analytical approach to the 4D-resolution function of three axes neutron spectrometers with focussing monochromators and analysers. Nucl. Instrum. Methods Phys. Res. A. 2014;752:54–64. doi:10.1016/j.nima.2014.03.019.

20. Moon RM, Riste T, Koehler WC. Polarization analysis of thermal-neutron scattering. Phys. Rev. 1969;181:920–31.

21. Shull CG, Strauser WA, Wollan EO. Neutron Diffraction by Paramagnetic and Antiferromagnetic Substances. Phys. Rev. 1951;83:333. doi:10.1103/PhysRev.83.333.

22. Asbrink S, Waskowska A. CuO: X-ray single-crystal structure determination at 196 K and room temperature. J Phys Condens Matter. 1991;3:8173–80.

23. Wang Z, Qureshi N, Yasin S, Mukhin A, Ressouche E, Zherlitsyn S, et al. Magnetoelectric effect and phase transitions in CuO in external magnetic fields. Nat. Commun. 2016;7:10295. doi:10.1038/ncomms10295.

24. Ain M, Menelle A, Wanklyn BM, Bertaut EF. Magnetic structure of CuO by neutron diffraction with polarization analysis. J Phys Condens Matter. 1992;4:5327–38.

25. Jones SPP, Gaw SM, Doig KI, Prabhakaran D, Hétroy Wheeler, E M, Boothroyd AT, Lloyd-Hughes J. High-temperature electromagnons in the magnetically induced multiferroic cupric oxide driven by intersublattice exchange. Nat. Commun. 2014;5:3787. doi:10.1038/ncomms4787.

26. Cao K, Giustino F, Radaelli PG. Theory of Electromagnons in CuO. Phys Rev Lett. 2015;114:197201. doi:10.1103/PhysRevLett.114.197201.

27. Ain M, Reichardt W, Hennion B, Pepy G, Wanklyn BM. Magnetic excitations in CuO. Physica C. 1989;162-164:1279–80.

28. Yang BX, Thurston TR, Tranquada JM, Shirane G. Magnetic neutron scattering study of single-crystal cupric oxide. Phys. Rev. B. 1989;39:4343–9.

29. Jacobsen H, Gaw SM, Princep AJ, Hamilton E, Tóth S, Ewings RA, et al. Spin dynamics and exchange interactions in CuO measured by neutron scattering. Phys. Rev. B. 2018;97:1224. doi:10.1103/PhysRevB.97.144401.

30. Gaw SM. "Cooperative Spin Excitations in Quantum Materials Studied by Neutron Spectroscopy". University of Oxford; 2014.

31. Yamasaki Y, Miyasaka S, Kaneko Y, He J-P, Arima T, Tokura Y. Magnetic Reversal of the Ferroelectric Polarization in a Multiferroic Spinel Oxide. Phys Rev Lett. 2006;96:207204. doi:10.1103/PhysRevLett.96.207204.

32. Pronin AV, Uhlarz M, Beyer R, Fischer T, Wosnitza J, Gorshunov BP, et al. B - T phase diagram of CoCr 2 O 4 in magnetic fields up to 14 T. Phys. Rev. B. 2012;85:867. doi:10.1103/PhysRevB.85.012101.

33. Eckold G, Gibhardt H, Caspary D, Elter P, Elisbihani K. Stroboscopic neutron diffraction from spatially modulated systems. Z. Krist. 2003:144–53.

Danksagung

Natürlich möchte ich mich auch noch bei allen Personen bedanken die mich im Verlauf dieser Arbeit unterstützt haben.
Zu allererst bei Prof. Dr. Eckold für die Möglichkeit diese Arbeit anzufertigen und für die Zeit die er sich genommen hat um mir den Einstieg in ein für mich neues Thema zu erleichtern. Vielen Dank auch für seine Anleitung und Unterstützung während der experimentell zähen Phasen der Promotion.
Prof. Dr. Techert für ihre Bereitschaft die Zweitbetreuung dieser Arbeit zu übernehmen und für ihre konstruktiven Rückmeldungen während der Jahresberichte.
Außerdem möchte ich mich noch bei allen weiteren Mitgliedern des Prüfungsausschusses bedanken.
Weiterhin möchte ich mich bei den ehemaligen und momentanen Mitarbeitern der Abteilung Eckold bedanken, für die zahlreichen interessanten und anregenden Diskussionen, notwendige Ablenkungen und die allgemein sehr angenehme Arbeitsatmosphäre.
Fabian Ziegler für die enge Zusammenarbeit bei zahlreichen Messreisen in Sachen Kupferoxid nach Garchingen. Patrick Kirscht für ständige Hilfsbereitschaft in bei technischen Problemen und die Zusammenarbeit am Wechselfeldmagneten. Dank auch an Norbert Jünke für die technische Hilfe an und um PUMA. Ebenso möchte ich Oleg Sobolev für seine ausdauernde und tatkräftige Hilfe bei der Entwicklung und dem Aufbau der Polarisationsanalyse sowie den folgenden Messreisen zum vollständigen PUMA danken. Furthermore, I would like to thank Avishek Maity for his support during the final polarization analysis measurements of this thesis, as well as for the implementation of lots of very comfortable and features of the analysis setup.
Dank gilt auch dem BMBF für die weitest gehende Finanzierung dieser Arbeit (Förderkennzeichen 05K13MG3)
Auch will ich mich bei meinen Freunden bedanken die mich im Verlauf des Projektes zum richtigen Zeitpunkt abgelenkt, ertragen und motiviert haben. Besonders Christian dafür das er eine frühe Version dieser Arbeit gelesen und kommentiert hat sowie Conny, Hanna, Katy und Marie für gute Gespräche, Mittagspausen, offene Ohren und Antrieb.
Zum Abschluss noch möchte ich mich noch besonders bei meiner Familie bedanken. Bei meinen Eltern die mir das Studium und alles daraus Folgende überhaupt erst ermöglicht haben, ihr Verständnis und die Selbstverständlichkeit ihrer Unterstützung bei meinen Großeltern für ihre Großzügigkeit sowie die herausragende logistische Unterstützung und bei Anngret das sie mich von Zeit zu Zeit an das Leben außerhalb der Uni erinnert hat.
Meinen Geschwistern, Robert und Annedore, für Motivation und das Gegenlesen der Arbeit. Wie üblich liegen alle verbleibenden ungünstigen Formulierungen und Fehler alleine bei mir.